

---

# Ultra High Performance Fibre Reinforced Concrete applied in Railway Bridges

---

PARAMETER STUDY

submitted in partial fulfillment of the  
requirements for the degree of

MASTER OF SCIENCE

in

STRUCTURAL ENGINEERING

by

J.V. de Geus  
born in Dirksland, The Netherlands



Concrete Structures  
Department of Structural Engineering  
Faculty CEG, Delft University of Technology  
Delft, the Netherlands  
[www.tudelft.nl](http://www.tudelft.nl)



Antea Group  
Rivium Westlaan 72  
2909 LD Capelle aan den IJssel  
the Netherlands  
[www.anteagroup.com](http://www.anteagroup.com)

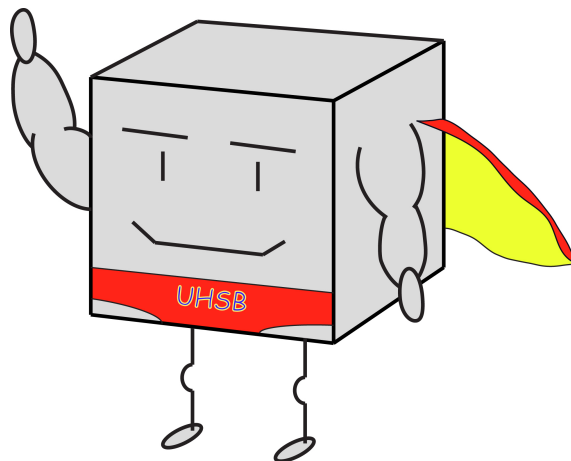


---

# Ultra High Performance Fibre Reinforced Concrete applied in Railway Bridges

---

Author: J.V. de Geus  
Student id: 4034023  
Email: j.v.degeus@student.tudelft.nl  
Date: May 25, 2014



Thesis Committee:

Chair: Prof.Dr.Ir. D.A. Hordijk, Faculty CEG, TU Delft  
University supervisor: Dr.Ir. C. van der Veen, Faculty CEG, TU Delft  
Company supervisor: Ing. M. Rovers, Antea Group  
Committee Member: Ir. R. Abspoel, Faculty CEG, TU Delft



---

## Preface

The report before you is my graduation work in order of fulfillment of the degree of master of science in structural engineering at Delft University of Technology. At the university people like to say that they are working on the boundaries between the known and unknown. Performing this research has let me experience what this boundary looks like and with finishing this research I hope to have relocated it.

First of all I would like to thank Antea Group for providing me with the opportunity and facilities to perform this research and its flexibility to let the research develop in a direction which suited both mine and the companies interest. Especially I would like to thank Martijn Roverts, who was not only the instigator of this research, but with who I have also spent countless hours in deliberation and who was able to make me see numerous subjects from a different angle.

Further I would like to thank my graduation committee Professor Hordijk, Cor van der Veen and Roland Abspoel. By asking the right questions they have challenged me and urged me to get to the bottom of the various subjects I have been working on. Working with them has made my graduation research better.

Like every graduate student I would not have been able to finish my research without the help from my friends. With this preface I thank them all for the tremendous support they have given me.

Last, but most important, I thank my parents. They have encouraged and made it possible for me to study and have always supported me in the direction I chose to go.

J.V. de Geus  
Delft, the Netherlands  
May 25, 2014



---

# Abstract

This research goes together with the literature study. This literature study sets the context for the main body of the research, the parameter study. Together they form the research on how the application of Ultra High Performance Fibre Reinforced Concrete (UHPFRC) influences the design of concrete railway bridges.

The literature study starts out by defining the properties of UHPFRC. The very specific mixture of UHPFRC causes not only a high strength and durability, but also leads to the requirement of different design verifications to be applied.

The literature study continues by investigating the important design aspects in conventional concrete railway bridges and UHPFRC structures. For conventional concrete railway bridges this is based on available design calculations. For UHPFRC structures the available literature leads to a more general approach. In this section of the research the term 'normativeness' is introduced as a measure for the importance of a certain design aspect. At the base of this lies the basic thought that the height of the unity check tells us something about how important this aspect is in the design. This approach leads to the conclusion that stresses and fatigue are the most important design aspects in concrete railway bridges. This is confirmed later on in the parameter study.

Whereas the literature study keeps a general character with regard to the material properties, the parameter study makes a clear choice for the regarded structure type and applied concrete mixture. The parameter study starts by setting the boundary conditions to the structure. The shape of the through bridge is defined and the material properties of the concrete mixture Ductal® CS1000 by Lafarge Group are presented.

As a regular design calculation the report continues to define the applied loadings, the prestressing and the verifications. Again the general character of the literature study on the design verifications is here omitted and the specific applied design calculations and verifications for UHPFRC are stated.

The main part of the parameter study has been performed with use of linear-elastic calculations. The material properties of UHPFRC suggest that the material is suitable for non-linear calculations. This is investigated with use of a non-linear beam model. The approach of these calculations and the corresponding verifications are defined in this report.

The parameter study for both the linear-elastic and the non-linear calculations have been performed by programming a Matlab model. The model uses an approach in which the cross section starts out too small and iteratively grows until all verifications are satisfied. This leads to a cross section which is more or less optimized as at least one unity check in a structure approaches one. A description of the Matlab model is present in the report.

The results are presented in three different sections. First, comparing UHPFRC with conventional concrete. Second, the verification on stresses in the serviceability limit state has shown to be of most influence on the design. Because the limitations do no right to the material properties of

UHPFRC, these limitations have been omitted. The results show how the stress limitations influence the design. Finally, the results of the non-linear calculations are presented and interpreted.

UHPFRC is a promising material with many favorable properties which can be applied in larger infrastructural works to reduce the cross sectional area. It must be noted however, that even though the cross sectional area can be reduced, the application of UHPFRC in through bridges does not lead to an extraordinary slenderness. It can be stated that even though its good performance UHPFRC is not a material which can easily be applied in order to prevent design challenges from occurring.

At this point in time UHPFRC is a viable option in the material choice when designing infrastructural works. It is however recommended that the choice for UHPFRC is done with regard of the consequences for the design calculations and that it is not just replacing the conventional concrete, but only applied at the points where the material properties can fully be used.

---

# Contents

<b>Preface</b>	<b>iii</b>
<b>Abstract</b>	<b>v</b>
<b>Contents</b>	<b>vii</b>
<b>1 Scope</b>	<b>1</b>
<b>2 Geometry</b>	<b>3</b>
2.1 Clearance cross section . . . . .	3
2.2 Inspection paths . . . . .	4
2.3 Track composition . . . . .	4
2.4 Cross section . . . . .	4
2.5 Cover . . . . .	4
2.6 Span . . . . .	5
2.7 Sign conventions . . . . .	5
<b>3 Materials</b>	<b>7</b>
3.1 Concrete mixture . . . . .	7
3.2 Prestressing steel . . . . .	8
3.3 Reinforcement steel . . . . .	8
<b>4 Loads</b>	<b>11</b>
4.1 Static load . . . . .	11
4.2 Life load . . . . .	11
4.3 Excluded loads . . . . .	15
4.4 Load combination . . . . .	15
<b>5 Prestressing</b>	<b>17</b>
5.1 Tendon profile . . . . .	17
5.2 Friction losses . . . . .	18
5.3 Initial prestressing force . . . . .	19
5.4 Time dependent losses . . . . .	20
5.5 Cable configuration . . . . .	21

<b>6</b>	<b>Verifications</b>	<b>23</b>
6.1	Ultimate limit state . . . . .	23
6.2	Serviceability limit state . . . . .	26
<b>7</b>	<b>Non-linear calculation</b>	<b>29</b>
7.1	Moment redistribution . . . . .	29
7.2	Moment-curvature relation . . . . .	31
7.3	Rotation capacity . . . . .	31
<b>8</b>	<b>Description of MatLab model</b>	<b>35</b>
8.1	Model scheme . . . . .	35
8.2	Length . . . . .	35
8.3	Initial conditions . . . . .	35
8.4	Loads . . . . .	39
8.5	Prestressing . . . . .	41
8.6	Verifications . . . . .	45
8.7	Unity checks . . . . .	48
8.8	Optimization . . . . .	49
8.9	Limitations . . . . .	52
<b>9</b>	<b>Results</b>	<b>55</b>
9.1	UHPFRC - Conventional concrete . . . . .	55
9.2	OVS stress demands . . . . .	68
9.3	Non-linear results . . . . .	76
<b>10</b>	<b>Conclusions</b>	<b>83</b>
10.1	Applying UHPFRC . . . . .	83
10.2	Reducing the stress limitations . . . . .	84
10.3	Non-linear calculations . . . . .	85
10.4	General conclusion . . . . .	85
<b>11</b>	<b>Recommendations</b>	<b>87</b>
	<b>References</b>	<b>89</b>
<b>A</b>	<b>Productsheet Ductal CS1000</b>	<b>93</b>
<b>B</b>	<b>Derrivation of uneven settlement</b>	<b>97</b>
B.1	Double span . . . . .	97
B.2	Three spans . . . . .	98
<b>C</b>	<b>Derivation of temperature load effect</b>	<b>101</b>
<b>D</b>	<b>Tendon profile</b>	<b>103</b>
D.1	Single span . . . . .	103
D.2	Three spans . . . . .	104

## CONTENTS

---

<b>E</b>	<b>Manual Calculation - One span</b>	<b>107</b>
E.1	Geometry . . . . .	107
E.2	Loads . . . . .	108
E.3	Load combinations . . . . .	110
E.4	Prestressing . . . . .	111
E.5	Verifications - main structure . . . . .	114
E.6	Verifications - floor . . . . .	121
E.7	Verification . . . . .	126
<b>F</b>	<b>Manual Calculation - Two span</b>	<b>129</b>
F.1	Geometry . . . . .	129
F.2	Loads - field . . . . .	130
F.3	Loads - support . . . . .	134
F.4	Load Combinations - Field . . . . .	136
F.5	Load Combinations - Support . . . . .	137
F.6	Prestressing . . . . .	139
F.7	Verifications . . . . .	143
F.8	Floor . . . . .	151
F.9	Verification . . . . .	152
<b>G</b>	<b>Verification non-linear beam model</b>	<b>155</b>



# Chapter 1

---

## Scope

Although there is a high level of interest in UHPFRC from the development and research field, the demand of UHPFRC is almost totally restricted to study projects. A round trough the Dutch concrete manufactures learns that due to this naught request of UHPFRC only a few concrete manufacturers have experimentally tried to make an UHPFRC mixture. Combined with the absence of a legislative bases this leads to the question of the chicken and the egg, or in this case supply and demand, which came first?

Due to this absence of a legislative basis and a lack of availability of mixtures with clear material properties UHPFRC is not yet being considered as an applicable option by engineers when they start a design project. The goal of this research is to provide more insight, in an early stage of design, in the normative design issues which may arise and the coarse dimensions when designing in UHPFRC. This should make the material more accessible and stimulate the use of it. This gives rise to the research question:

“How do the material specific properties of Ultra High Performance Fibre Reinforced Concrete influence the design of infrastructural structures compared to structures in conventional concrete?”

This question has already qualitatively been regarded in the literature study. This was based on study projects available in the literature. To provide more insight in the design of UHPFRC structures and give a more elaborate and quantitative answer a parameter study will be performed. The first step in this is to make an inventory of the calculation methods and design verifications applicable for UHPFRC. The parameter study will be performed for single track trough bridges with a varying span length. The cross-section of the bridge will be determined in order to be in compliance with the Eurocode and OVS requirements. Although the literature study includes girder bridges and plate bridges in the research as well, they are excluded here. The development of a UHPFRC prefabricated girder is subject to specific production knowledge which is better known at prefab producers. Plate bridges usually give rise to less design challenges than trough bridges and are therefore also disregarded in the parameter study. Double track trough bridges are excluded since the effect of the side walls is almost nothing at midspan of the floor in cross direction and the floor depth approaches the size of a solid slab. Single track trough bridges are commonly applied in fly-overs and have shown to be challenging designs.

Due to the nature of the parameter study it will be possible to look further into the governing design aspect for railway bridges; 'stress limits in the serviceability limit state'. On this subject of the OVS demands ('Design Recommendations for Railway Bridges', Dutch: 'Ontwerp Voorschriften Spoorwegen') on railway bridges, the research will investigate whether loosening the strict demands with regard to the allowable stresses will render railway bridges in UHPFRC to be more economical.

This will be done by altering the requirements and investigate the effect on the required cross section dimensions. Thus answering the research question:

“How do the stress limits in the serviceability limit state influence the design when they are altered to better accommodate the material properties of Ultra High Performance Fibre Reinforced Concrete?”

As UHPFRC is a very tough material it is capable of withstanding large rotations. This allows a large redistribution of bending moment. This study will give an onset on the investigation of the possibilities for non-linear designing of UHPFRC structures and answer the following research question:

“Do the material properties of Ultra High Performance Fibre Reinforce Concrete make the material more suitable for non-linear calculations than conventional concrete?”

The parameter study is performed by developing a model which calculates the minimum required cross section for a varying span. This is done by starting with a known too small cross-section which is then increased in size until the requirements are met. The required dimensions and resulting highest unity checks are printed after which the span is increased and the process starts again.

## Chapter 2

---

# Geometry

The geometry of the railway bridges is determined by ProRail rules and are recorded in the OVS. The minimum widths for the cross sections of the bridges are determined according to the OVS00026 (Kremer, 2010) and OVS00056 (Valkenburg, 2012). Points of departure for the geometry of the bridge are: mixed freight and passenger traffic, no horizontal curvature and a train speed of 200 km/h.

### 2.1 Clearance cross section

The clearance cross section is the cross section above and next to the railway track where no fixed or temporary objects may be situated. The OVS increases the clearance cross section with the so called Red Zone. In this zone exceptions may be made for certain objects. The OVS defines four different clearance cross sections. In case of new railway tracks or major modifications of existing tracks the OVS always requires the clearance cross section PVR-GC to be applied. This research makes use of this clearance cross section PVR-GC including the red zone as depicted in figure 2.1.

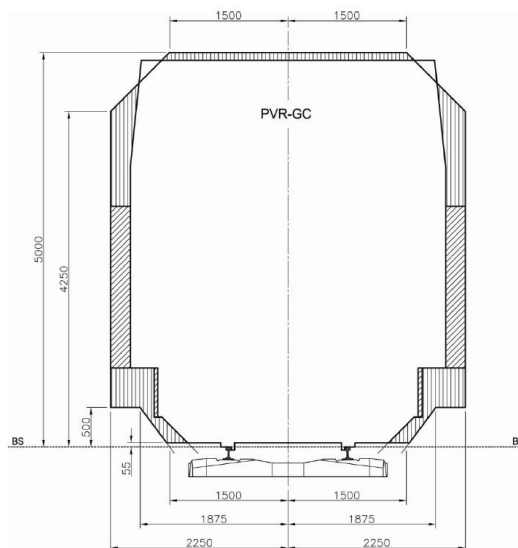


Figure 2.1: Clearance cross section PVR-GC with surrounding red zone. (Kremer, 2010)

For tracks where a train speed of 200 km/h is allowed a further increase is required due to the pressure wave caused by the passing train. This gives that the horizontal distance to the centre of the clearance cross section is required to be 2.75 m.

## 2.2 Inspection paths

Every railway track is required to have at least one inspection path next to the track. This track is to be placed outside of the pressure wave zone. For speeds above 40 km/h the path is required to have a minimum width of 1.00 m which may be reduced to 0.80 m in case of obstacles like signposts. In case of a double track at each side an inspection path is required.

In case of single track trough bridges the inspection path may not be situated more than 840 mm above the rail level. When the walls of the trough become higher these can no longer be used as a path and the bridge has to be widened with a path at rail level. Widening of the bridge however has a big influence on the construction depth of the trough floor. As this depth is the effective construction height with regard to the clearance cross section below the structure it is desirable that the floor depth is as small as possible. To achieve this the floor is not widened, but the escape route from the railway track to the inspection paths is made possible by steps or ladders at the inside of the wall. These provisions may only be applied in coördinance with the contractor and with additional safety provisions like extended warning times.

In case the trough walls are less than 1000 mm wide the inspection paths can be constructed with an exterior steel framework.

## 2.3 Track composition

The composition of the track construction was determined based on OVS00056. As the track is supposed to support mixed traffic and the bridge is supposed to be a new construction the traffic type according to OVS00056 is IV-M. This results in a track composition of ballast and sleepers. The ballast is required to have a thickness of 350 mm below the sleeper. The bottom of the ballast layer is situated 730 mm under the top of the track.

The ballast layer is supposed to be enclosed at a distance of minimum 2000 mm and maximum 2150 mm from the centre of the track.

## 2.4 Cross section

A typical cross section for a single track trough bridge is depicted in figure 2.2.

## 2.5 Cover

The cover to be applied on the reinforcement and prestressing steel is fifty and respectively sixty millimeter according to the demands with regard to durability in the NEN-EN 1992-1-1. This being based on the environmental class XD3 and a construction class 'S5'. The construction class based on S4, plus two for hundred years design life time, minus one for the increased concrete strength.

Due to the excellent durability properties of UHPFRC the cover can be reduced substantially. In the study project 'Modular UHPC bridge' (Tirimanna & Buitelaar, 2012) the suggested cover was ten millimeter according to the involved concrete technologist. As this project was a pedestrian bridge the cover applied cover in this study on railway bridges is increased to twenty millimeter on the outermost reinforcement bar and thirty millimeter on the prestressing ducts. This is also in compliance with the applied cover in the thesis of (Kenter, 2010) where a metro structure in UHPC was designed with a cover of twenty millimeter.

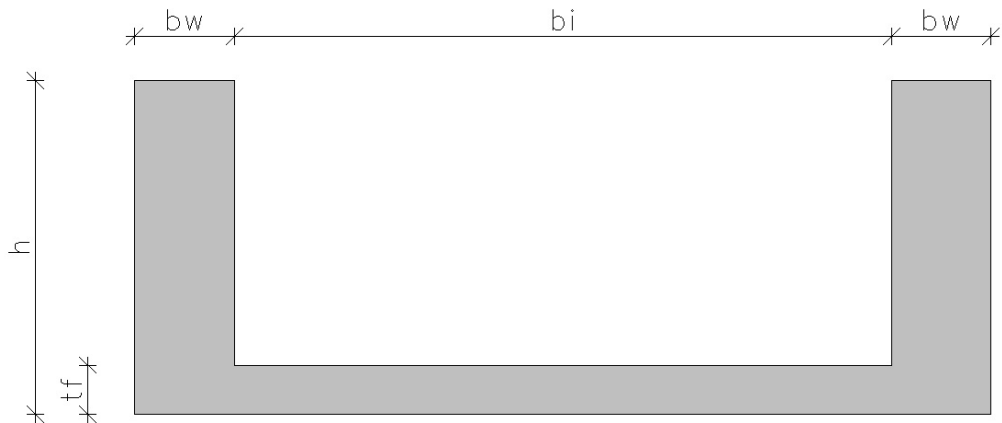


Figure 2.2: Typical cross section for UHPFRC trough bridge.

## 2.6 Span

The span of the bridges is the main variable in the model. It will incrementally go up from ten to forty meters. Also the number of spans will vary. Both statically determined bridges containing a single span and statically undetermined bridges of two spans will be investigated on the behavior of the required dimensions.

## 2.7 Sign conventions

Throughout the project the global sign conventions as depicted in figure 2.3 have been used. In which  $x, y, z$  are the global directions and  $u, v, w$  are the global displacements.

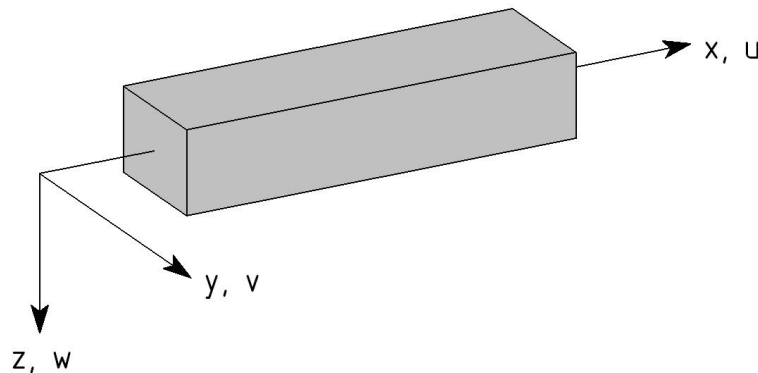


Figure 2.3: Global sign conventions

Figure 2.4 shows the sign conventions which have been used for in- and external forces.

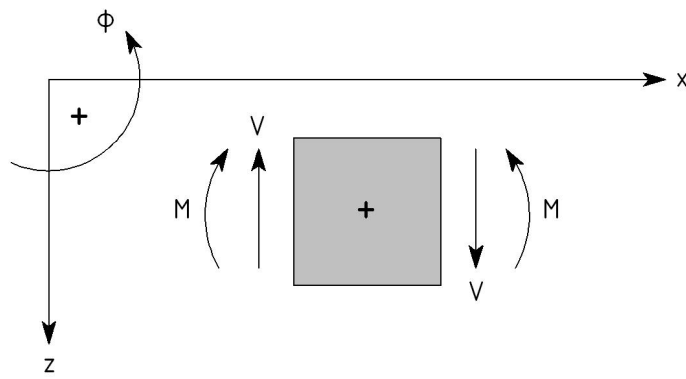


Figure 2.4: Force sign conventions

## Chapter 3

# Materials

### 3.1 Concrete mixture

The general properties of UHPFRC were extensively described in the literature study. As the aim of this research is to make a step from theory to practical application of the material a commercially available mixture was chosen. This leads to practically possible results.

The applied concrete mixture is Ductal® CS1000 by Lafarge Group. Ductal® has been commercially available for a number of years now and its mixtures have already been applied in various structures. The CS1000 mixture is a mixture for structural applications like bridges, marine docks and piles. The characteristics of the mixture which have been used in this research are presented in table 3.1. A product sheet by Ductal® has been added in appendix A.

Property	Symbol	Value	Unit
Density	$\rho$	26	$kN/m^3$
Compression mean	$f_{cm}$	180	$N/mm^2$
Compressing design	$f_{cd}$	160	$N/mm^2$
Tension mean	$f_{ctk;0.05}$	10	$N/mm^2$
Tension design	$f_{ctd}$	8	$N/mm^2$
Young's modulus	$E_{cm}$	55000	$N/mm^2$
Fiber length	$l_f$	14	$mm$
Fiber diameter	$d_f$	0.2	$mm$
Poisson ratio	$\nu$	0.2	–
Shrinkage factor	$\epsilon_{cd}(\infty)$	$10^{-5}$	–
Creep factor	$\phi_{\infty,t_0}$	0.5	–
Coefficient of thermal expansion	$\alpha_T$	12	$\mu m/m/^\circ C$

Table 3.1: Material properties Ductal® CS1000

The supplied material properties are not sufficient to draw a complete stress-strain diagram. With use of the article (Ketel, Willemse, van Rijen, & Koolen, 2011) additional characteristics have been specified. This has as consequence that a conservative approach has been used in order for the material to correspond as much as possible with the Eurocode.

Property	Symbol	Value	Unit	
Compressive yield strain	$\epsilon_{c3}$	$= 2.3 \cdot 10^{-3}$	[-]	
Ultimate concrete strain	$\epsilon_{cu3}$	$= 2.6 \cdot 10^{-3}$	[-]	
Youns' modulus	$E_{cd}$	$= f_{cd}/\epsilon_{c3}$	$N/mm^2$	
Tension yield strain	$\epsilon_{ct}$	$= f_{ctd}/E_{cd}$	$= 0.115 \cdot 10^{-3}$	[-]
Maximum strain at $f_{ctd}$	$\epsilon_{ctd} = \epsilon_{ct0.3}$	$= \frac{0.3}{l_c} + \epsilon_{ct}$	[-]	
Ultimate tensile strain	$\epsilon_{ctu}$	$= \frac{l_f}{4 \cdot l_c}$	[-]	
Fibre length	$l_f$	$= 14$	mm	
Specimen length	$l_c$	$= \frac{2}{3} \cdot h$	mm	

Table 3.2: Material properties Ductal® CS1000 (continued).

### 3.2 Prestressing steel

The prestressing system exists of a number of cables build up by strands of  $140 \text{ mm}^2$ . The applied prestressing steel is FeP1860. It has the following properties.

Property	Symbol	Value	Unit
Characteristic strength	$f_{pk}$	1860	$N/mm^2$
Ultimate design strength	$f_{pu}$	1690	$N/mm^2$
Characteristic yield strength	$f_{p0.1k}$	1674	$N/mm^2$
Design yield strength	$f_{pd}$	1521	$N/mm^2$
Young's modulus	$E_p$	195000	$N/mm^2$
Density	$\rho$	78.5	$kN/m^3$
Yield strain	$\epsilon_{sy}$	7.6	$^\circ/\infty$
Ultimate strain	$\epsilon_{su}$	35.0	$^\circ/\infty$

Table 3.3: Material properties FeP1860

### 3.3 Reinforcement steel

The applied reinforcement steel is B500B with the following properties.

Property	Symbol	Value	Unit
Characteristic yield strength	$f_{yk}$	500	$N/mm^2$
Design yield strength	$f_{yd}$	435	$N/mm^2$
Young's modulus	$E_p$	200000	$N/mm^2$
Density	$\rho$	78.5	$kN/m^3$
Yield strain	$\epsilon_{sy}$	2.2	$^\circ/\infty$
Ultimate strain	$\epsilon_{su}$	32.5	$^\circ/\infty$

Table 3.4: Material properties B500B

The amount of applied reinforcement is constant for all spans and models. This allows to easily compare the aspects which are for this study of the most interest; the concrete dimensions and

the governing design aspects. By keeping the reinforcement constant the concrete dimensions and therefore the various capacities become a function of the material properties of UHPFRC.

Keeping the applied reinforcement constant does have its drawbacks. As a wide range of spans is evaluated with the same reinforcement it is obvious that the reinforcement is not always turned to full account. Or at the other side of the spectrum, the applied reinforcement is insufficient. Both situations will be present in the results. In the first case this will result in low unity checks for verifications where the reinforcement plays a role (moment capacity, shear capacity). In the second case the model will increase the capacity by enlarging the cross section. Here very large, and perhaps unrealistic, results may be found.

Direction	location	$\varnothing$ [mm]	Spacing [mm]
Longitudinal	floor top	16	150
Longitudinal	floor bottom	16	150
Longitudinal	top wall	20	100
Cross Floor	bottom	25	125
Cross Floor	top	25	125
Vertical	walls	20	100

Table 3.5: Applied reinforcement steel.

The applied reinforcement steel has been based on practical considerations. The minimum reinforcement applied in civil concrete structures is usually about  $\varnothing 16 - 150$ . This is applied at the positions where no large amount of required reinforcement is expected. In the top of the wall increased amount of reinforcement is applied as this influences the moment capacity of the trough above the mid support. As the walls are expected to become quite thin the reinforcement bars are placed with a spacing of 100 mm.

In the conventional concrete structures for cracked cross sections the reinforcement has to be able to withstand the entire shear force. The applied shear reinforcement has therefore determined by the occurring shear force in the conventional concrete structures.

Due to the method of schematizing the floor the bending moments are the same in positive and negative direction. The reinforcement in the floor is therefore equal in the top and bottom side. Section 9.1.3 will go into further detail on this topic.

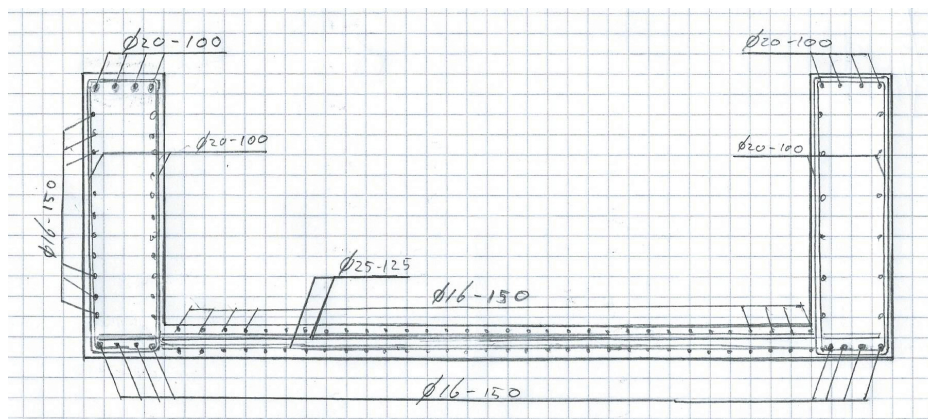


Figure 3.1: Typical reinforcement.



## Chapter 4

---

# Loads

In this chapter all loads acting on the bridges are stated according to the Eurocode and OVS.

### 4.1 Static load

#### 4.1.1 Self weight concrete

Due to the high packing density the self weight of UHPFRC is considerably higher than for conventional concrete. Ductal® CS1000 has a self weight  $26 \text{ kN/m}^3$ , but in general the self weight of UHPFRC can easily reach up to  $29 \text{ kN/m}^3$ .

Conventional reinforced concrete	$\gamma_c = 25 \text{ kN/m}^3$
Ultra High Performance Fibre Reinforced Concrete	$\gamma_c = 26 \text{ kN/m}^3$

#### 4.1.2 Track composition

The self weight of the track structure is given as an average value including the ballast, the sleepers, the railway beams and the influence of possible lifting during maintenance. The depth of the track composition is required to be calculated from the top of the deck to 150 mm below the top of the track.

$$\text{Track structure } \gamma_t = 22 \text{ kN/m}^3$$

### 4.2 Life load

#### 4.2.1 Load model 71

The load model 71 (LM71) indicates the effect of the vertical loading due to regular railway traffic. Its characteristic values are indicated in figure 4.1. The spread load  $q_{vk}$  has no limitation in length. According to the national annex to the Eurocode these values have to be multiplied by a factor  $\alpha = 1.21$  to obtain the classified vertical loading. In case of calculating the deflection with relation to passenger comfort this factor  $\alpha = 1.0$ .

#### 4.2.2 Load model SW/0 and SW/2

Load model SW/0 and SW/2 indicate the vertical loading due to respectively normal railway traffic on continuous girders and heavy railway traffic. The model and characteristic values are given in figure 4.2 and table 4.1. The characteristic values have to be multiplied with the factor  $\alpha = 1.21$  to obtain the classified vertical loading.

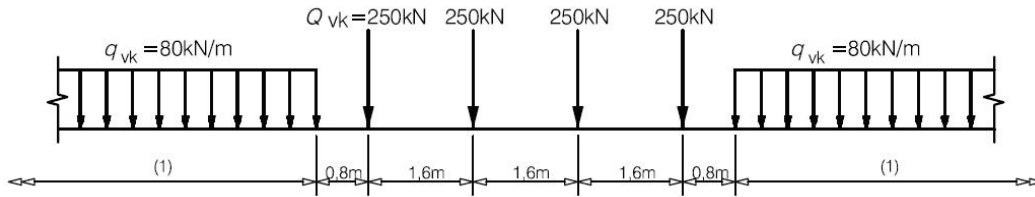


Figure 4.1: Load model 71 - characteristic values

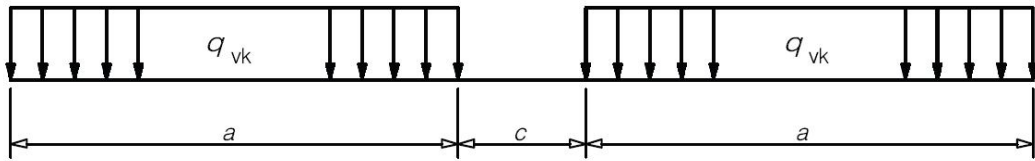


Figure 4.2: Load model SW/0 and SW/2

Load model	$q_{vk}$ [kN/m]	$a$ [m]	$c$ [m]
SW/0	133	15.0	5.3
SW/2	150	25.0	7.0

Table 4.1: Characteristic values load model SW/0 and SW/2

**4.2.3 Pathways**

Non-public inspection paths are supposed to be loaded by a spread load with a characteristic value of:

$$\text{Pathways } q_{fk} = 5 \text{ kN/m}^2$$

**4.2.4 Dynamic loading**

The dynamic effects have been taken into account by multiplying the static results with the dynamic factor  $\Phi$ . This dynamic factor only has to be applied to the load models 71, SW/0 and SW/2. The dynamic factor is taken for a standard maintained railway track.

$$\begin{aligned} \text{Standard maintenance } \phi_3 &= \frac{2.16}{\sqrt{L_\Phi} - 0.2} + 0.73 \\ \text{with: } & 1.00 \leq \Phi_3 \leq 2.00 \end{aligned} \tag{4.1}$$

In this equation  $L_\Phi$  is the determining length. For the main span direction this length is identified as:

$$\begin{aligned} \text{Simply supported} & \quad \text{Main span length} \\ \text{Continuous over 2 spans} & \quad L_\Phi = 1.2 \cdot \frac{1}{2}(L_1 + L_2) \end{aligned} \tag{4.2}$$

### 4.2.5 Fatigue loading

The fatigue loading to be considered is the composition of heavy traffic with axle-loads of 250 kN. This composition exists of the four load models: five, six, eleven and twelve (appendix D NEN-EN1991-2). The dynamic load factor for fatigue calculations is given to be:

$$\phi_{fat} = 1 + \frac{1}{2}(\phi' + \frac{1}{2}\phi'') \quad (4.3)$$

with:

$$\phi' = \frac{K}{1 - K + K^4} \quad (4.4)$$

in which:

$$K = \frac{v}{160} \quad L_{\Phi} \leq 20 \text{ m}$$

$$K = \frac{v}{47.16L^{0.408}} \quad L_{\Phi} > 20 \text{ m}$$

and

$$\phi'' = 0.56e^{-\frac{L_{\Phi}^2}{100}} \quad (4.5)$$

in which:

$$L_{\Phi} \quad \text{determined length [m]}$$

$$v \quad \text{maximum allowed speed [m/s]}$$

### 4.2.6 Thermal loading

Thermal loading of the structure causes imposed deformations. The loading consists of a constant and a linear component. The temperature changes of concrete bridges are defined in the Eurocode.

The linear component of the temperature load has been defined by NEN-EN 1991-1-5 for concrete bridge decks. The applied loads are depicted in figure 4.3.

The coefficient of thermal expansion for UHPFRC has been determined to be  $\alpha_T = 15 \cdot 10^{-6}$  (Graybeal, 2006). Specifically for Ductal® the coefficient of thermal expansion is  $\alpha_T = 12 \cdot 10^{-6}$ .

Due to the application of a ballast bed on the trough floor the cross-section will not experience an evenly spread temperature change across the cross section. As the trough walls will experience an imposed deformation due to the temperature gradient, the stiffness of the trough floor will prohibit the walls from totally deforming. There will be a certain measure of interaction between the stiffness of the floor, the deformation of the walls and the resulting internal forces. This effect was not possible to take into account in the used numerical model for the parameter study. The thermal load effects have been taken into account as an imposed deformation on a one dimensional model.

#### Single span

In the statically determined single span structure no resistance to the imposed deformation is present. Therefore no internal forces due to thermal loading will occur.

#### Double span

As the static system of the double span bridge contains one support which is fixed in horizontal direction no resulting forces due to expansion or contraction will occur. The linear temperature gradient however introduces a constant curvature over the length of the structure. A bending moment will develop in the cross section above the mid support. As the temperature gradient is bi-linear it is split in two cases of which the results are calculated and consequently added. The magnitude of the moments can be found by:

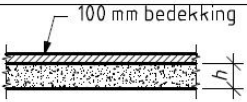
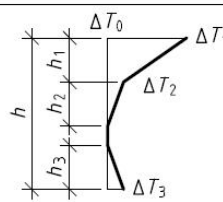
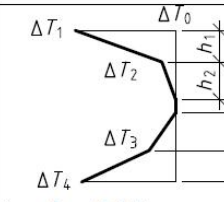
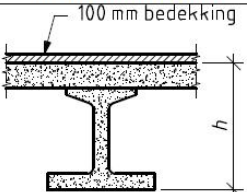
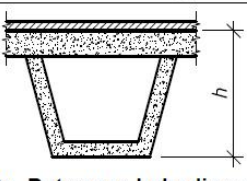
Constructietype	Temperatuurverschil ( $\Delta T$ )																																																										
	(a) Opwarming		(b) Afkoeling																																																								
 <p>100 mm bedekking</p> <p><b>3a. Betonnen plaat</b></p>																																																											
 <p>100 mm bedekking</p> <p><b>3b. Betonnen liggers</b></p>	<p><math>h_1 = 0,3 h</math> maar <math>\leq 0,15</math> m</p> <p><math>h_2 = 0,3 h</math> maar <math>\geq 0,10</math> m en <math>\leq 0,25</math> m</p> <p><math>h_3 = 0,3 h</math> maar <math>h_3 \leq h - h_1 - h_2</math> en <math>h_3 \leq (0,10 \text{ m} + \text{slijtlaagdikte [m]})</math></p>		<p><math>h_1 = h_4 = 0,20 h</math> maar <math>\leq 0,25</math> m</p> <p><math>h_2 = h_3 = 0,25 h</math> maar <math>\leq 0,20</math> m</p>																																																								
 <p><b>3c. Betonnen kokerligger</b></p>	<table border="1"> <thead> <tr> <th><math>h</math> m</th> <th><math>\Delta T_1</math> °C</th> <th><math>\Delta T_2</math> °C</th> <th><math>\Delta T_3</math> °C</th> </tr> </thead> <tbody> <tr> <td><math>\leq 0,2</math></td> <td>-</td> <td>-</td> <td>-</td> </tr> <tr> <td>0,4</td> <td>10</td> <td>7</td> <td>0</td> </tr> <tr> <td>0,6</td> <td>10</td> <td>5</td> <td>0</td> </tr> <tr> <td><math>\geq 0,8</math></td> <td>10</td> <td>4,5</td> <td>0</td> </tr> </tbody> </table>	$h$ m	$\Delta T_1$ °C	$\Delta T_2$ °C	$\Delta T_3$ °C	$\leq 0,2$	-	-	-	0,4	10	7	0	0,6	10	5	0	$\geq 0,8$	10	4,5	0	<table border="1"> <thead> <tr> <th><math>h</math> m</th> <th><math>\Delta T_1</math> °C</th> <th><math>\Delta T_2</math> °C</th> <th><math>\Delta T_3</math> °C</th> <th><math>\Delta T_4</math> °C</th> </tr> </thead> <tbody> <tr> <td><math>\leq 0,2</math></td> <td>-</td> <td>-</td> <td>-</td> <td>-</td> </tr> <tr> <td>0,4</td> <td>-5</td> <td>-3</td> <td>0</td> <td>0</td> </tr> <tr> <td>0,6</td> <td>-5</td> <td>-3</td> <td>0</td> <td>0</td> </tr> <tr> <td>0,8</td> <td>-5</td> <td>-2,5</td> <td>0</td> <td>0</td> </tr> <tr> <td>1,0</td> <td>-5</td> <td>-1,5</td> <td>0</td> <td>0</td> </tr> <tr> <td><math>\geq 1,5</math></td> <td>-5</td> <td>-0,5</td> <td>0</td> <td>0</td> </tr> </tbody> </table>			$h$ m	$\Delta T_1$ °C	$\Delta T_2$ °C	$\Delta T_3$ °C	$\Delta T_4$ °C	$\leq 0,2$	-	-	-	-	0,4	-5	-3	0	0	0,6	-5	-3	0	0	0,8	-5	-2,5	0	0	1,0	-5	-1,5	0	0	$\geq 1,5$	-5	-0,5	0	0
$h$ m	$\Delta T_1$ °C	$\Delta T_2$ °C	$\Delta T_3$ °C																																																								
$\leq 0,2$	-	-	-																																																								
0,4	10	7	0																																																								
0,6	10	5	0																																																								
$\geq 0,8$	10	4,5	0																																																								
$h$ m	$\Delta T_1$ °C	$\Delta T_2$ °C	$\Delta T_3$ °C	$\Delta T_4$ °C																																																							
$\leq 0,2$	-	-	-	-																																																							
0,4	-5	-3	0	0																																																							
0,6	-5	-3	0	0																																																							
0,8	-5	-2,5	0	0																																																							
1,0	-5	-1,5	0	0																																																							
$\geq 1,5$	-5	-0,5	0	0																																																							

Figure 4.3: Temperature difference for concrete decks (Eurocode, 2011b)

$$\phi = \left| \frac{M_{\Delta T_i} \cdot L}{3 \cdot EI} \right| = \frac{\kappa \cdot L}{2} \quad (4.6)$$

$$M_{\Delta T_i} = \frac{3}{2} \kappa \cdot EI \quad (4.7)$$

In which:

$$\kappa = \alpha_T \cdot \Delta T_i \cdot \frac{1}{h_i} \quad (4.8)$$

#### 4.2.7 Uneven settlement

Imposed deformation due to uneven settlement introduces forces due to the stiffness of the structure. The Eurocode requires a settlement of  $\delta = 10 \text{ mm}$  of each support with regard to the adjacent supports. In trough bridges, which generally have a large stiffness, this requirement may lead to such high forces in the structure that they become dominant or the structure even becomes impossible to build.

The value  $\delta = 10 \text{ mm}$  prescribed in the Eurocode is a conservative value. By performing additional soil investigation a better prediction of the settlement behavior can be given. With this knowledge measures can be taken to reduce the settlement. A better knowledge of the behavior of the structure in combination with monitoring of the structure can justify the application of a reduced settlement. This method is not uncommon in practice and therefore under these remarks the applied settlement in this research is reduced to  $\delta = 5 \text{ mm}$ .

The introduced load effects have been derived in appendix B.2.2.

### 4.3 Excluded loads

The following loads have been excluded from the model.

- Centrifugal forces. The model only treats bridges without horizontal curvature. Therefore no centrifugal forces will occur.
- Nosing force. The sideways forces are of minimal effect on the construction depth of the bridge.
- Traction and braking. Although traction and braking introduce rather large forces on the structure, their effect on the geometry of the cross section is very limited.
- Construction loads. The load combinations during construction are considered to have marginal influence on the design of the structure.
- Wind loads. The sideways forces are of minimal effect on the construction depth of the bridge.

### 4.4 Load combination

The applied loads on the structure result in a set of load combinations. The load combinations have been put together according to NEN-EN 1990-1-1.

#### 4.4.1 Ultimate limit state

The calculations on behalf of the strength of the structure are performed in the ultimate limit state (ULS). The design values of the loads in this case are given in table A2.4(B) of the NEN-EN 1990-1-1.

Tabel A2.4(B) — Rekenwaarden voor de belastingen (STR/GEO) (groep B)

Blijvende en tijdelijke ontwerpsituaties	Blijvende belastingen		Voorspanning	Dominante veranderlijke belasting (*)	Tegelijkertijd optredende Veranderlijk belastingen (*)		Blijvende en tijdelijke ontwerpsituaties	Blijvende belastingen		Voorspanning	Dominante veranderlijke belasting (*)	Tegelijkertijd optredende Veranderlijk belastingen (*)	
	Ongunstig	Gunstig			Belangrijkste (indien aanwezig)	Andere		Ongunstig	Gunstig			Belangrijkste (indien aanwezig)	Andere
(Vgl. 6.10)	$\gamma_{G,sup} G_{k,sup}$	$\gamma_{G,inf} G_{k,inf}$	$\gamma_F P$	$\gamma_{Q,1} Q_{k,1}$		$\gamma_{Q,1} \psi_0 Q_{k,1}$	(Vgl. 6.10a)	$\gamma_{G,sup} G_{k,sup}$	$\gamma_{G,inf} G_{k,inf}$	$\gamma_F P$		$\gamma_{Q,1} \psi_{0,1} Q_{k,1}$	$\gamma_{Q,1} \psi_{0,2} Q_{k,2}$
							(Vgl. 6.10b)	$\gamma_{G,sup} G_{k,sup}$	$\gamma_{G,inf} G_{k,inf}$	$\gamma_F P$	$\gamma_{Q,1} Q_{k,1}$		$\gamma_{Q,1} \psi_{0,2} Q_{k,2}$

(\*) Veranderlijke belastingen zijn die, die zijn beschouwd in de tabellen A2.1 tot en met A2.3.

OPMERKING 1 De keuze tussen 6.10, of 6.10a en 6.10b kan zijn aangegeven in de nationale bijlage. In de gevallen 6.10a en 6.10b kan de nationale bijlage bovendien 6.10a zo wijzigen dat hij alleen nog maar blijvende belastingen omvat.

OPMERKING 2 De  $\gamma$ - en  $\psi$ -waarden kunnen in de nationale bijlage zijn voorgeschreven. De volgende waarden voor  $\gamma$  en  $\psi$  zijn aanbevolen wanneer de vergelijkingen 6.10, of 6.10a en 6.10b zijn gebruikt:

$\gamma_{G,sup} = 1,35^{1)}$   
 $\gamma_{G,inf} = 1,00$   
 $\gamma_Q = 1,35$  wanneer Q ongunstige belastingen voorstelt ten gevolge van weg- of voetgangersverkeer (0 wanneer ze gunstig zijn)  
 $\gamma_Q = 1,45$  wanneer Q ongunstige belastingen voorstelt ten gevolge van spoorwegverkeer, door de belastinggroepen 11 tot en met 31 (uitgezonderd 16, 17, 26<sup>3)</sup> en 27<sup>3)</sup>), belastingmodellen LM71, SW/0 en HSLM en werkelijke treinen, wanneer ze als afzonderlijke hoofdverkeersbelastingen zijn beschouwd (0 wanneer ze gunstig zijn)  
 $\gamma_Q = 1,20$  wanneer Q ongunstige belastingen voorstelt ten gevolge van spoorwegverkeer, door de belastinggroepen 16 en 17 en SW/2 (0 wanneer ze gunstig zijn)  
 $\gamma_Q = 1,50$  voor andere verkeersbelastingen en andere veranderlijke belastingen<sup>2)</sup>  
 $\psi = 0,85$  (zodat  $\psi_{0,sup} = 0,85 \times 1,35 = 1,15$ )  
 $\gamma_{Gset} = 1,20$  in het geval van een lineair elastische berekening, en 1,35 in het geval van een niet-lineaire berekening, voor ontwerpsituaties waar belastingen ten gevolge van ongelijke zettingen ongunstige effecten kunnen hebben. Voor ontwerpsituaties waar belastingen ten gevolge van ongelijke zettingen gunstige effecten kunnen hebben, moeten deze belastingen niet in rekening zijn gebracht.

Zie eveneens EN 1991 tot en met EN 1999 voor  $\gamma$ -waarden te gebruiken bij opgelegde vervormingen.

$\gamma_F$  = aanbevolen waarden die zijn vastgelegd in de ter zake doende Eurocode voor ontwerp en berekening.

1) Deze waarde geldt voor: eigen gewicht van de constructieve en niet constructieve elementen, ballast, grond, grondwater en vrij water, wegneembare belastingen enz.  
 2) Deze waarde geldt voor: veranderlijke horizontale gronddruk door grond, grondwater, vrij water en ballast, gronddruk door bovenbelasting door verkeer, aerodynamische belastingen door verkeer, wind- en thermische belastingen enz.  
 3) Voor spoorverkeersbelastingen door de belastinggroepen 26 en 27 mag  $\gamma_Q = 1,20$  zijn toegepast op afzonderlijke componenten van verkeersbelastingen als die te maken hebben met SW/2 en mag  $\gamma_Q = 1,45$  zijn toegepast op afzonderlijke componenten van verkeersbelastingen die te maken hebben met de belastingmodellen LM71, SW/0 en HSLM enz.

Zie vervolg

Tabel A2.4(B) (einde)

Blijvende en tijdelijke ontwerp-situaties	Blijvende belastingen		Voor-spanning	Dominante veranderlijke belasting (*)	Tegelijkertijd optredende Veranderlijk belastingen (*)		Blijvende en tijdelijke ontwerp-situaties	Blijvende belastingen		Voor-spanning	Dominante veranderlijke belasting (*)	Tegelijkertijd optredende Veranderlijk belastingen (*)	
	Ongunstig	Gunstig			Belangrijkste (indien aanwezig)	Andere		Ongunstig	Gunstig			Belangrijkste (indien aanwezig)	Andere
(Vgl. 6.10)	$\gamma_{0,sup} G_{k,sup}$	$\gamma_{0,inf} G_{k,inf}$	$\gamma_P$	$\gamma_{0,1} Q_{k,1}$		$\gamma_{0,1} Q_{k,1}$	(Vgl. 6.10a)	$\gamma_{0,sup} G_{k,sup}$	$\gamma_{0,inf} G_{k,inf}$	$\gamma_P$		$\gamma_{0,1} Q_{k,1}$	$\gamma_{0,1} Q_{k,1}$
							(Vgl. 6.10b)	$\psi \gamma_{0,sup} G_{k,sup}$	$\gamma_{0,inf} G_{k,inf}$	$\gamma_P$	$\gamma_{0,1} Q_{k,1}$		$\gamma_{0,1} Q_{k,1}$

OPMERKING 3 De karakteristieke waarden van alle blijvende belastingen afkomstig van één bron zijn vermenigvuldigd met  $\gamma_{0,sup}$  indien het totale resulterende belastingeffect ongunstig is en met  $\gamma_{0,inf}$  indien het totale resulterende belastingeffect gunstig is. Bijvoorbeeld mogen alle belastingen afkomstig van het eigen gewicht van de constructie zijn beschouwd als afkomstig van één bron; dit geldt ook indien verschillende materialen zijn gebruikt. Zie evenwel A2.3.1(2).

OPMERKING 4 Voor bepaalde toetsingen mogen de waarden voor  $\gamma_0$  en  $\gamma_Q$  zijn onderverdeeld in  $\gamma_0$  en  $\gamma_Q$  en de factor  $\gamma_{0,sup}$  die rekening houdt met de onzekerheden van het model. In de meeste normaal voorkomende gevallen mag een waarde voor  $\gamma_{0,sup}$  in het bereik 1,0 – 1,15 zijn gebruikt; deze mag in de nationale bijlage zijn gewijzigd.

OPMERKING 5 Waar belastingen afkomstig van water niet zijn afgedekt door EN 1997 (bijv. waterstroming), mogen de te gebruiken belastingcombinaties zijn aangegeven per afzonderlijk project.

Figure 4.4: Design values ultimate limit state

### 4.4.2 Serviceability limit state

The serviceability limit state (SLS) knows three combinations; the characteristic, frequent and quasi-permanent. They are stated below. The values for  $\Psi$  are given in table A2.3 of the NEN-EN 1990-1-1. This table distinguishes between load combinations built up of individual load components or load groups. The groups consist mostly consist of a vertical traffic load in combination with horizontal loads. As stated the horizontal loads have been excluded in this research, leaving only the vertical components in the load groups. Load model SW2 gets a different  $\Psi$ -factor when applied as individual load or within a group. As in practice the loads are most likely to be applied as a group the  $\Psi$ -factor for load model SW2 is taken as  $\Psi_1 = 0.8$ .

$$\text{Characteristic combination } \sum_{j \geq 1} = G_{k,j} \text{ “+” } P \text{ “+” } Q_{k,1} \text{ “+” } \sum_{i > 1} \Psi_{0,i} Q_{k,i} \quad (4.9)$$

$$\text{Frequent combination } \sum_{j \geq 1} = G_{k,j} \text{ “+” } P \text{ “+” } \Psi_{1,1} Q_{k,1} \text{ “+” } \sum_{i > 1} \Psi_{2,i} Q_{k,i} \quad (4.10)$$

$$\text{Quasi-permanent combination } \sum_{j \geq 1} = G_{k,j} \text{ “+” } P \text{ “+” } \sum_{i \geq 1} \Psi_{2,i} Q_{k,i} \quad (4.11)$$

In which  $G$  is the permanent loading,  $P$  the prestressing loading and  $Q$  the variable loading.

### 4.4.3 Fatigue

For the verifications on fatigue loading a separate load combination is prescribed.

$$\sum_{j \geq 1} = \left( G_{k,j} \text{ “+” } P \text{ “+” } \Psi_{1,1} Q_{k,1} \text{ “+” } \sum_{i > 1} \Psi_{2,i} Q_{k,i} \right) \text{ “+” } Q_{fat} \quad (4.12)$$

## Chapter 5

# Prestressing

### 5.1 Tendon profile

The placement of the cables follows a parabolic layout. This allows the geometry of the cables to be described by a function. The starting point is that the cables are applied as close as possible to the outermost fibre in order to increase the effectiveness of the prestressing.

#### 5.1.1 Single span

In single span structures the tendon profile follows the parabola as indicated in figure 5.1. The parabola is defined as:

$$g(x) = \frac{4(z_b - f)}{L^2} \cdot x^2 \quad (5.1)$$

The derivation of the tendon profile can be found in appendix D.

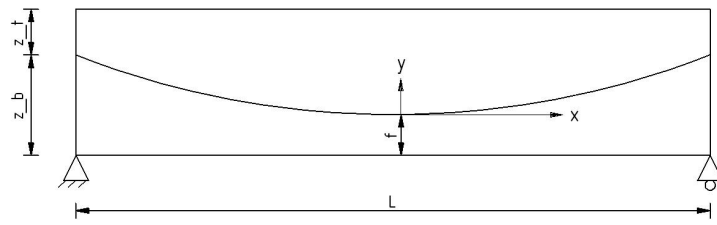


Figure 5.1: Tendon profile single span structure

#### 5.1.2 Two spans

The tendon profile for two spans can be derived from the tendon profile of three spans. The tendon profile is symmetrical about the mid support. The spans can be regarded as the end spans in the structure with three spans. Therefore the same parabolic functions apply. The functions of the parabolas have been derived in appendix D and are:

$$h(x) = \frac{1}{2 \cdot R} (x - x_2)^2 + y_2 \quad (5.2)$$

$$g(x) = \frac{1}{2R + \frac{x_2^2}{y_2}} \cdot x^2 \tag{5.3}$$

In which  $R$  is the radius of the tendon profile above the support and  $x_1$  is given as:

$$x_1 = 2 \cdot \frac{y_2}{x_2} \cdot R + x_2 \tag{5.4}$$

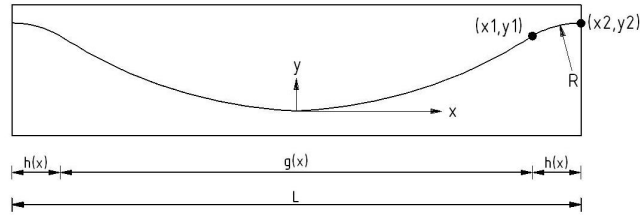


Figure 5.2: Tendon profile in midspan

The tendon profile in the end spans are not symmetrical. Therefore the global position of the origin of the coordinate system is unknown. This can be solved by treating the distance  $x_2$  as unknown and solving it through the boundary and matching conditions. This results in:

$$h(x) = \frac{1}{2 \cdot R} (x - x_2)^2 + y_2 \tag{5.5}$$

$$g(x) = \frac{1}{2R + \frac{x_2^2}{y_2}} \cdot x^2 \tag{5.6}$$

with:

$$x_2 = \frac{L \pm \sqrt{\frac{y_3}{y_2} \cdot (L^2 - 2R \cdot y_3) + 2R \cdot y_3}}{1 - \frac{y_3}{y_2}} \tag{5.7}$$

## 5.2 Friction losses

Due to friction between the prestressing steel and the duct, the prestressing force will vary over the length of the cable. This effect is influenced by the rotation of the cable, the friction coefficient

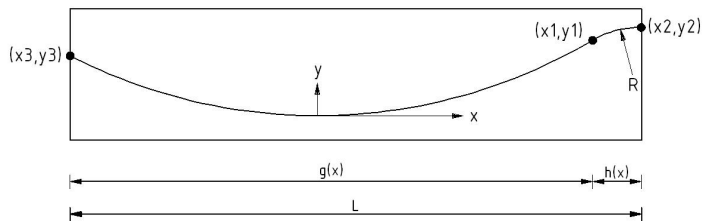


Figure 5.3: Tendon profile in endspan

and the so called wobble-effect. The prestressing force after friction losses can be expressed as a function of the length.

$$P(x) = P_0 \cdot e^{-\mu(\Delta\theta+k \cdot x)} \quad (5.8)$$

In which:

$\mu$	friction coefficient	
$\Delta\theta$	total sum of absolute angular rotation	
$k$	wobble-effect	(5.9)
$x$	x-coordinate of the considered cross section	

The friction coefficient is dependent on the chosen prestressing system and is generally between  $\mu = 0.15 - 0.25$  for systems with strands. The applied prestressing system here requires a friction coefficient of  $\mu = 0.17$ . The wobble-effect for regularly applied prestressing systems is  $k = 0 - 0.01 \text{ rad/m}$ . The applied wobble-effect is  $k = 0.008 \text{ rad/m}$ .

Besides the friction losses over the length of the cable, the wedge settlement introduces losses as well. This effect takes place over a certain length which depends on the slope of the friction losses and the actual settlement of the cable. The wedge-set length can be calculated by:

$$l_{set} = \frac{w_{set} \cdot E_p}{\frac{\Delta\sigma_p}{\Delta x}} \quad (5.10)$$

in which:

$w_{set}$	retraction of the prestressing cable in the anchor	
$E_p$	young's modulus of the prestressing steel	(5.11)
$\frac{\Delta\sigma_p}{\Delta x}$	slope of the friction loss diagram	

The size of the wedge settlement is dependent on the anchor system and is usually between  $w_{set} = 5 - 15 \text{ mm}$ . The applied wedge set in this project was  $w_{set} = 10 \text{ mm}$ .

### 5.3 Initial prestressing force

Requirements on the maximum allowed tensile stresses in the outermost fibres dictate the boundary conditions for the minimum required and maximum allowed prestressing force. Starting point for this method is that at prestressing ( $t = 0$ ) only the self-weight of the structure is present and at  $t = \infty$  time dependent losses have occurred and the system is fully loaded. The boundary conditions can be derived by the sets of equations for the different static systems presented in equations 5.12 through 5.17.

The maximum allowable tensile stresses in the concrete are given in the OVS00030-6 (Kremer, 2012) (see also the literature study on this topic). Table 5.1 shows the allowable tensile stresses. The demands make a distinction between the cases whether the considered outer fibre is located near the prestressing cable or not.

One span

$t = 0$

$$\sigma_{top} = -\frac{P_0}{A_c} + \frac{M(P)}{W_t} - \frac{M(G)}{W_t} \quad (5.12)$$

$t = \infty$

$$\sigma_{bottom} = -\frac{P_\infty}{A_c} - \frac{M(P)}{W_b} + \frac{M(G+Q)}{W_b} \quad (5.13)$$

Two spans

$t = 0$

$$\sigma_{top} = -\frac{P_0}{A_c} + \frac{M(P)}{W_t} - \frac{M(G)}{W_t} \quad (5.14)$$

Load combination	Location	maximum tensile stress [N/mm <sup>2</sup> ]
Quasi-permanent	Everywhere	0
Frequent	No prestressing	0.5 * $f_{ctk:0.05}$ or $\sigma_c < 1.5$
Frequent	Prestressing	0
Characteristic	No prestressing	0.75 * $f_{ctk:0.05}$ or $\sigma_c < 2.25$
Characteristic	Prestressing	0.5 * $f_{ctk:0.05}$ or $\sigma_c < 1.5$
Construction phase	Everywhere	$\sigma_c < f_{ctmt}$ or $\sigma_c < 3.0$

Table 5.1: Maximum allowable tensile stresses according to OVS00030-6

$$\sigma_{bottom} = -\frac{P_0}{A_c} + \frac{M(P)}{W_b} - \frac{M(G)}{W_b} \quad (5.15)$$

$t = \infty$

$$\sigma_{top} = -\frac{P_\infty}{A_c} - \frac{M(P)}{W_t} + \frac{M(G+Q)}{W_t} \quad (5.16)$$

$$\sigma_{bottom} = -\frac{P_\infty}{A_c} - \frac{M(P)}{W_b} + \frac{M(G+Q)}{W_b} \quad (5.17)$$

## 5.4 Time dependent losses

### 5.4.1 Creep

The influence of creep has been taken into account according to paragraph 3.1.4 in the NEN-EN 1992-1-1. The creep strain was calculated for the moment in time at  $t = \infty$  with equation 5.18.

$$\varepsilon_{cc}(\infty, t_0) = \phi(\infty, t_0) \cdot \left( \frac{\sigma_c}{E_c} \right) \quad (5.18)$$

In which:

$\varepsilon_{cc}(\infty, t_0)$	creep strain at $t = \infty$
$\phi(\infty, t_0)$	creep coefficient of the mixture
$\sigma_c$	constant concrete compressive stress applied at $t = 0$
$E_c$	Tangent modulus $1.05 \cdot E_{cm}$

The creep coefficient is dependent on the concrete mixture. The applied creep coefficient is  $\phi(\infty, t_0) = 0.5$ .

### 5.4.2 Shrinkage

The shrinkage is the combined strain due to drying shrinkage and autogenous shrinkage. The autogenous shrinkage can be calculated trough:

$$\varepsilon_{ca} = 2.5(f_{ck} - 10) \cdot 10^{-6} \quad (5.19)$$

The drying shrinkage of the ductal CS1000 mixture is given to be less than  $\varepsilon_{cd} < 10^{-5}$ . This upper limit is taken into account as strain due to drying shrinkage.

### 5.4.3 Relaxation

As the prestressing system is no different in this structure compared to structures in conventional concrete, the general rules for relaxation as described in the NEN-EN 1992-1-1. The applied equation for the relaxation in the prestressing steel is:

$$\frac{\Delta\sigma_{pr}}{\sigma_{pi}} = 0.66 \cdot \rho_{1000} \cdot e^{9.1\mu} \left( \frac{t}{1000} \right)^{0.75(1-\mu)} \cdot 10^{-5} \quad (5.20)$$

In which:

$\Delta\sigma_{pr}$	absolute value of relaxation losses
$\sigma_{pi}$	maximum stresses in the prestressing steel after immediate friction losses
$\rho_{1000}$	relaxation loss in % after 1000 hours at an average temperature of 20°C
$\mu$	$= \sigma_{pi} / f_{pk}$
$t$	time after prestressing in hours

The design lifetime of the structure of 100 years implies a time of  $t = 876000$  hours. The value of  $\rho_{1000}$  can be taken as 2.5% for strands.

## 5.5 Cable configuration

There is a high degree of interaction between the dimensions of the cross-section, the prestressing force, the amount, the type and the position of the cables. This makes that the cable configuration has got an almost unlimited number of possibilities. In order to make all bridges comparable and reduce the number of possible cable configurations some boundary conditions were created.

1. All cables are positioned in the webs of the trough.
2. All cables have a vertical curvature.
3. All cables are positioned in the webs in pairs of two.
4. A maximum of eight or twelve cables per web for the single and double span structure respectively.

The choice for the size of the cables has been done by creating an iterative process in the model where each time either the number of strands in the cable or the height of the trough is increased. At each iteration the self weight and the boundary conditions for the prestressing are recalculated. This process continues until the required height with regard to the anchor plates has been met and  $P_{min} < P_{max}$ .



## Chapter 6

---

# Verifications

### 6.1 Ultimate limit state

#### 6.1.1 Effective width

The effective width over which the stresses can uniformly be distributed, influences the cross-section which contributes to the load distribution. The effective width of the floor has been calculated according to paragraph 5.3.2.1 of the NEN-EN 1992-1-1. Applied for this situation of the trough bridge this becomes:

$$b_{eff} = b_{eff,1} + b_w \leq b \quad (6.1)$$

In which:

$$b_{eff,1} = 0.2 \cdot \frac{1}{2} b_i + 0.1 \cdot l_0 \leq 0.2 \cdot l_0$$
$$b_{eff,1} \leq b_i$$

and

$$l_0 = 1.00 \cdot L \quad \text{for field single span structure}$$
$$l_0 = 0.85 \cdot L \quad \text{for field double span structure}$$
$$l_0 = 0.15 \cdot 2 \cdot L \quad \text{for support double span structure}$$

#### 6.1.2 Bending moment capacity

As the effective width can be smaller than half of the actual cross-section the applied bending moment is divided over the two effective areas. The unity check for the bending moment capacity is:

$$\frac{M_{E,d}}{M_{R,d}} \leq 1.0 \quad (6.2)$$

$$M_{E,d} \quad \text{effective bending moment}$$
$$M_{R,d} \quad \text{bending moment resistance}$$

Due to the high compressive strength of the concrete it may occur that horizontal equilibrium can be reached with a very small compressive height. This will result in a strain in the reinforcement steel which is well beyond the ultimate steel strain. This is an additional verification which applies for UHPFRC and should be performed just as the verification of the maximum compressive zone height.

### 6.1.3 Shear capacity

The verifications on shear capacity in the ultimate limit state contain two facets. First the flexural shear and second the compression strut. As UHPFRC allows slender and thin constructions the latter is possibly more pronounced in UHPFRC structures than in structures of conventional concrete. To gain insight in the influence of both aspects two separate unity checks were performed.

$$\text{unity check} = \frac{V_{Ed}}{V_{Rd}} \quad (6.3)$$

$$\text{unity check} = \frac{V_{Ed}}{V_{Rd,max}} \quad (6.4)$$

$V_{E,d}$	effective shear force
$V_{R,d}$	shear resistance
$V_{Rd,max}$	compressive strut capacity

### 6.1.4 Lateral torsional buckling

In conventional concrete structures very thin, slender beams, loaded under bending are rarely applied. Therefore lateral torsional stability is hardly ever verified. In UHPFRC it is possible to design very thin beams under bending. This also occurs in the design of the trough bridges in this research and therefore a verification on lateral torsional buckling has been included.

For lateral torsional buckling on concrete beams in structures no absolute verification exists. The approach of the Eurocode shows this by only stating that lateral torsional buckling should be verified in slender beams. However, no quantitative method is described. It does state that no second order effect has to be taken into account in case certain conditions with regard to the slenderness are met.

Two different approaches were investigated on their suitability of application for structural elements. First the method applied for lifting concrete prefabricated beams (de Jong & Schaafsma, 1997) and secondly the method described in the dissertation 'New vision on flexural-torsional buckling, stability and strength of structural members' (Raven, 2006).

The reasoning of the first method is that the lateral torsional buckling moment is an upper limit at which lateral torsional buckling certainly will occur. However, just like with the Euler buckling load for normal loaded elements, this upper limit will never be achieved due to imperfections in the structural element. To calculate this upper limit the method makes use of an effective width of the floor which is included in the torsional stiffness. This does increase the lateral torsional moment capacity, but the influence of the ratio between the floor- and wall thickness is not taken into account. After a second order displacement has been calculated this displacement is transposed to a horizontal bending moment. Lateral torsional buckling is assumed to occur when this bending moment is larger than the horizontal bending moment capacity.

In the dissertation (Raven, 2006) an analysis of stability due to second order effects was developed. This method was compared to the results of verifications in the NEN 6760, NEN 6770 and NEN 6720, the design codes for respectively timber, steel and concrete structures. Although these design codes have very different approaches for the verification of stability, it was found that the, in the dissertation developed method, gives results almost equal to the design codes and is applicable for concrete structural elements. Therefore this approach has been chosen to evaluate lateral torsional buckling and is described below. The dissertation shows that the approach is applicable for statically determined and undetermined beams.

Note that, although the dissertation shows the possible application of the method on concrete elements, this method may not yet be regarded as the absolute value of lateral torsional buckling for concrete. Further research is required on this specific topic. In this research the verification on

lateral torsional buckling has to be regarded as an indication of the sensitivity of the structure to this type of instability.

The general verification for lateral torsional buckling is:

$$\frac{N_{Ed}}{N_{Rd}} + \frac{\overline{M}_{y,Ed}}{M_{y,Rd}} + \frac{\overline{M}_{z,Ed}}{M_{z,Rd}} \leq 1 \quad (6.5)$$

$N_{E,d}$	effective normal force
$N_{R,d}$	normal force resistance
$M_{y,Ed}$	effective bending moment about y axis
$M_{y,Rd}$	bending moment resistance in y axis
$M_{z,Ed}$	effective bending moment about z axis
$M_{z,Rd}$	bending moment resistance in z axis

In this the overlined bending moments stand for the bending moment including the second order effect. As in this research horizontal forces are neglected  $\overline{M}_{z,Ed}$  only consists of the second order bending moment of the size :

$$\overline{M}_{z,Ed} = \overline{M}_{z2} = -EI_z \cdot \overline{v}_2'' \quad (6.6)$$

This second order moment can be found by:

$$M_{z2} = \frac{F_E}{k_1} \frac{\overline{v}_0}{n_z^* - 1} \quad (6.7)$$

In which:

$F_E$	Euler buckling load
$\overline{v}_0$	initial displacement
$n_z^*$	second order factor

The initial displacement is taken as  $\overline{v}_0 = L/300$ . This value is stated in the NEN 1992-1-1 as the horizontal deflection due to geometrical imperfection.

The second order factor for a beam with a lateral support (in this case the trough floor) in the tension zone can be found with equation E.104.

$$\frac{1}{n_z^*} = \frac{k_1 M_{y1} + F_c \frac{h}{2}}{GI_t \frac{2}{h} + F_E \frac{h}{2}} \quad (6.8)$$

In which:

$M_{y1}$	maximum bending moment
$F_c$	normal load
$k_1$	factor depending on construction type and loading
$GI_t$	effective torsional stiffness

Loading	$k_1$
constant moment	1.0
constant distributed load	0.88
concentrated load at midspan	0.73

Table 6.1: Values for factor  $k_1$ .

### 6.1.5 Fatigue loading

The verification of the structure subject to fatigue loading is done according to the first method described in the literature study and the loads described in section 4.2.5.

## 6.2 Serviceability limit state

### 6.2.1 Deflection

The occurring deflection has been calculated as a result of the curvature due to the loading. Solving the differential equation with the corresponding boundary conditions gives the deflection of the structure.

$$-EI \cdot \frac{d^2w}{dx^2} = M \quad (6.9)$$

The statical vertical deflection in the serviceability limit state is limited to  $w_{max} = L/800$ . The deflection is also limited by a vertical acceleration of the train with relation to passenger comfort. The NEN-EN 1990 gives maximum vertical deflections to limit the vertical acceleration. For a comfort level 'Very good' a vertical acceleration of  $b_v = 1.0 \text{ m/s}^2$  is considered. The limiting vertical deflection which corresponds with this is depended on the length of the span and the velocity of the train. This relation is depicted in figure 6.1.

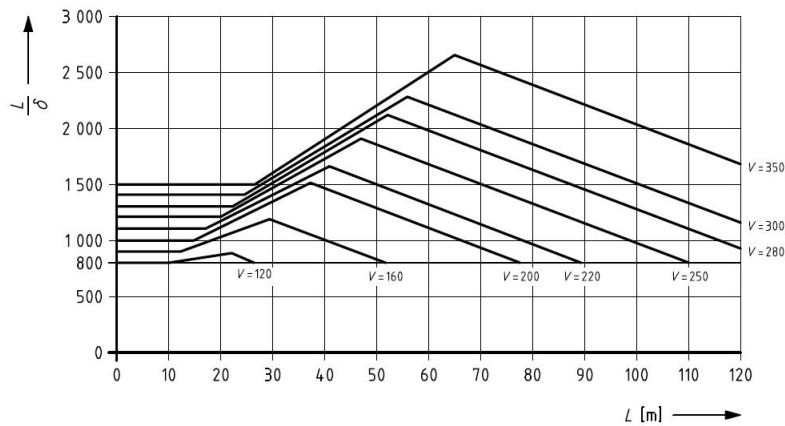


Figure 6.1: Relation between deflection  $\delta$ , span  $L$  and velocity  $V$ . (Eurocode, 2011a)

### 6.2.2 Stresses

The OVS demands with regard to the allowable tensile stresses in the structure are verified by making use of the cross section analysis. The stresses have been calculated according to equation 6.10 and 6.11.

$t = 0$

$$\sigma_{top} = -\frac{P_0}{A_c} + \frac{M_p}{W_t} - \frac{M(G)}{W_t} \quad (6.10)$$

$t = \infty$

$$\sigma_{bottom} = -\frac{P_\infty}{A_c} - \frac{M_p}{W_b} + \frac{M(G+Q)}{W_b} \quad (6.11)$$

### 6.2.3 Crack width

The current state of technology doesn't grant a quantitative method for determining the crack width in UHPFRC. The application of the crack width calculation for conventional concrete would give very unjust results due to the fine distribution of the fibers. Therefore the crack width calculation has been left out of the model. This will have no large implications for the results. After all in the longitudinal direction the requirements with regard to the stresses in the SLS prevent cracking from happening.

In the cross direction however this requirement is not present. To not ignore the influence of the crack width demands on the cross section, the applied yield stress of the reinforcement in the floor is reduced in the calculation of the moment capacity. The applied yield stress is  $f_{yd}^* = 300 \text{ N/mm}^2$ . This causes the application of a thicker floor with a larger section modulus to reduce the maximum stresses and thus the crack formation.



## Chapter 7

---

# Non-linear calculation

The bending moments cause (micro-)cracks to occur. These cracks will lead to a reduced stiffness in the cross section, as given by the relation in the moment-curvature diagram (section 7.2). Due to the capacity of UHPFRC to withstand large strains in comparison with conventional concrete, it is able to allow large rotations and is therefore well able to redistribute bending moments along the structure.

### 7.1 Moment redistribution

The concrete structure is most fully used when both above the mid support and in the field the moment capacity is approached. Before the moment capacities are reached the effective moment causes the concrete to crack and to approach a plastic hinge. When a plastic hinge occurs, this cross section will not be able to withstand a larger bending moment, but the curvature will increase, causing the bending moment to increase at other cross sections. While increasing the load this will continue to happen until the first plastic cross section fails, or the failure mechanism has been formed with plastic hinges. The resulting bending moment distribution will have a smaller absolute maximum bending moment, which is favorable for the dimensions of the cross section.

Due to the non-linear moment-curvature relation, in a statically determined structure of one simply supported span some reduction of the stiffness will occur before the plastic moment will be reached. This causes that only very limited redistribution of bending moments can take place since as the plastic moment has been reached a plastic hinge will be formed and the failure mechanism occurs. The failure mechanism for a simply supported, statically undetermined structure of two spans requires the development of two plastic hinges. The absolute maximum bending moment will occur above the support. At increasing of the load the first plastic hinge will occur here. Increasing the load further will cause a plastic moment to occur in the field. Since the load redistribution in the single span structure is very limited only the statically undetermined structure will be evaluated with a non-linear calculation.

Figure 7.1 shows the approach of the calculation of the redistributed bending moment. First, the moment distribution with the linear elastic approach is calculated. With use of the moment curvature diagram for the cross section the curvature can be determined at the cross sections of the discretized structure. The curvature distribution can be integrated twice with the trapezium method to find the corresponding deflection line. The boundary conditions which should be applied are that the deflection at each support should be zero. For the end supports this can be enforced, but at the midsupport the deflection may be unequal to zero due to an unrealistic curvature distribution. In this case the boundary conditions aren't met and the support bending moment is lowered with

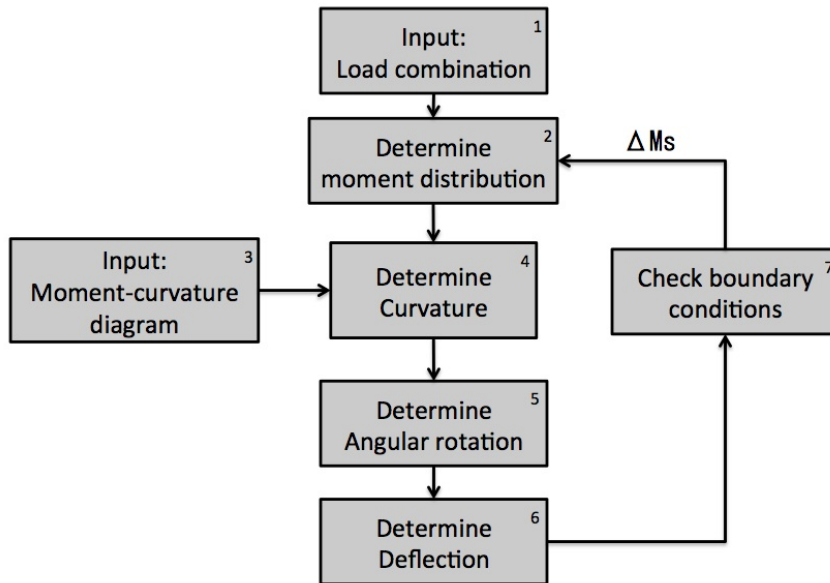


Figure 7.1: Process chart for non-linear moment redistribution. (Dilsiz, 2013)

stepsize  $\Delta M_s$  and the redistributed bending moment is calculated. This process will continue until the boundary conditions are met.

In step five and six from figure 7.1 the curvature line is integrated twice with the trapezium method. This numerical integration calculates the area beneath the curve, but the integration constants are unknown. These integration constants can be found by applying boundary conditions. For the integration of the curvature to the angular rotation it holds that at the points where the derivative of the curvature is zero, the angular rotation is also zero. The applied boundary condition for the integration from angular rotation to deflection is that the deflection at the end support is required to be zero.

The process of finding the redistributed bending moment requires a bending moment distribution known over the full length of the two spans. However, in the linear elastic calculations, due to symmetry, only one span has been modeled. In order to proceed with the calculation of the redistributed bending moment an assumption for the bending moment distribution over the second span is required. This can be done as the evaluated bending moment lines in the ultimate limit state define the moment envelop. This moment envelop will cause the largest curvature and therefore the largest reduction in stiffness. As it is not possible to say that either one span will be loaded to the maximum before the other is, it may be assumed that the maximum reduced stiffness is present in the second span. This can be modeled by mirroring the moment envelop about the midsupport. The assumption that the lowest stiffness is present in the second span is a safe assumption as it allows less redistribution of bending moment. Implicitly this approach models a loading history where the second span has been fully loaded before the evaluated span is.

The calculation of the redistributed bending moment is done according to figure 7.2. For each moment distribution in which the support moment is larger than the field moment, the maximum amount of moment distribution is the difference between the maximum field moment and the moment capacity in that cross section (distance  $a$ ). Redistribution of the bending moment will not influence the distance  $b$ . Therefore the redistributed bending moment can be calculated as the dis-

tance between line A and B, which is at each point the same as the distance between C and D.

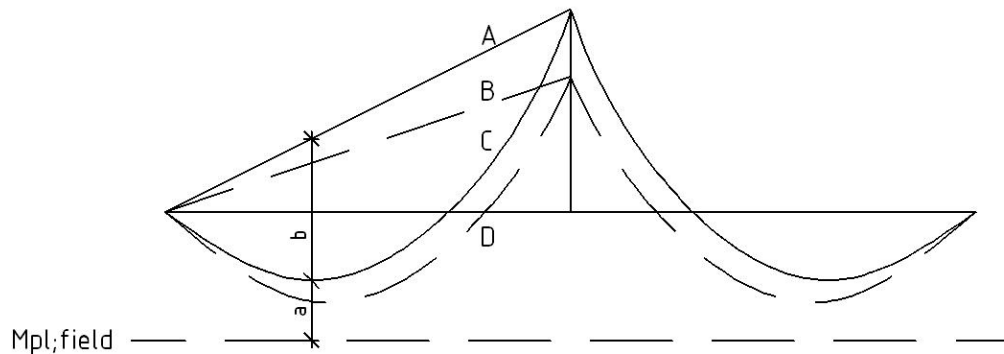


Figure 7.2: Redistribution of the bending moment.

## 7.2 Moment-curvature relation

The moment curvature relation, which is input for the non linear calculation of the moment distribution, has been determined with use of the multiple layer model. This model, which previously has been used in multiple studies, discretizes the cross section in a number of small layers and calculates the strain distribution in the cross section due to the applied curvature. The applied multiple layer model is a variation based on the model used by (Dilsiz, 2013). The model has been altered to be applicable for pretensioned concrete cross sections with a varying width over the height. The resulting diagram therefore is a moment - normal force - curvature diagram.

The input for the multiple-layer-model are the geometry, the normal force, the constitutive relations of the different materials and the curvature. For each curvature the corresponding strain- and stress-distribution can be found. From this the resulting bending moment which corresponds with the applied curvature can be calculated. Calculating the bending moments for a range of curvatures for a cross section gives the MNC-diagram for that specific cross section. Due to the curved tendon profile the MNC-diagram is different for each cross section. Figure 7.3 gives the flow chart of the multiple layer model.

In order to find the required moment capacity after moment redistribution, the linear-elastic moment distributions which cause the maximum support- and field-moment are important. With these two moment distributions all other moment distributions are accommodated for. The linear-elastic moment distributions which provide the maxima are known from the linear elastic model.

## 7.3 Rotation capacity

At the sections in the bridge where the stiffness is reduced an increased rotation will occur. The Eurocode describes a method in which the maximum allowed rotation is split between the tough reinforced concrete and the more brittle prestressed concrete (figure 7.4). Although the UHPFRC trough bridge is prestressed, the material is very tough. Especially this aspect makes that UHPFRC is very suitable for moment redistribution. As to not be detrimental to the material properties due to the applied rules it was chosen not to apply the Eurocode verification here.

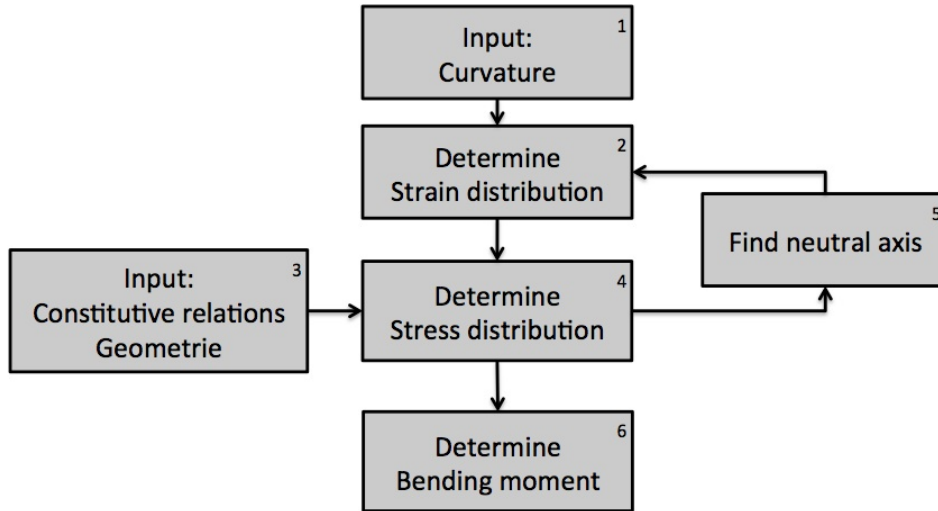


Figure 7.3: Process chart multiple layer model. (Dilsiz, 2013)

The CUR 108 publication allows the rotation capacity to be calculated based on the actual occurring strain. Assuming a constant curvature over the length  $d$  or  $2 \cdot d$  (depending on the considered cross section) the ultimate rotation capacity can be calculated. As the actual occurring strain is dependent on the material properties this method will allow the large deformation capacity of UHPFRC to be used. Important to note is that this method has not experimentally been verified for UHPFRC. It is however a plausible approach for how the material may behave.

As the rotation is largest under the load combinations in the ultimate limit state only these situations have to be verified. The maximum allowed rotation is given by function 7.1 for cross sections in the field and by equation 7.2 for the cross section above the midsupport.

$$\Phi_u = \frac{\epsilon_{cu3}}{x_u} \cdot 2d \quad (7.1)$$

$$\Phi_u = \frac{\epsilon_{cu3}}{x_u} \cdot d \quad (7.2)$$

In which:

- $\Phi_u$  maximum allowed rotation
- $\epsilon_{cu3}$  ultimate compressive strain
- $x_u$  ultimate height of the compressive zone
- $d$  effective cross sectional height

The actual occurring rotation in the evaluated cross section is calculated in the redistribution of the bending moment and is therefore already known. The verification can be defined as  $\Phi_{Ed} \leq \Phi_{ud}$ .

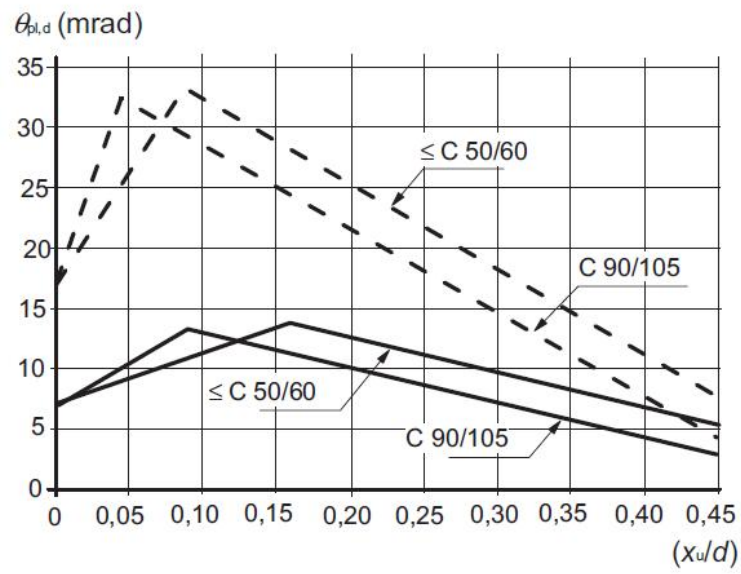


Figure 7.4: Maximum allowed rotation according to NEN-EN 1992-1-1.



## Chapter 8

---

# Description of MatLab model

### 8.1 Model scheme

The parameter study has been performed in a model in the computer program Matlab. This was done on account of the program which allows all intermediate calculated data to be extracted and the function of the program to make relative easy changes to the boundary conditions and compare the results.

The basic idea behind the model is that a too small cross section will be subject to the design verifications. As this cross section will not be able to satisfy the verifications the cross section will be enlarged until all verifications are satisfied. The result of the model is an optimized cross section. For the non-linear calculations the model uses a different approach. It loads the linear-elastic results and then, after redistribution of the bending moment, reduces the height until one of the verifications is no longer satisfied. The output is the last evaluated geometry in which all verifications are satisfied.

Figure 8.1 shows the process chart of the Matlab model for both the single and double span linear elastic calculation. The applied theory has been described in the previous chapters.

The Matlab model has been verified by performing manual calculations for both the single and double span structure. A longer span length of 40 m for the single span structure was chosen to show the structural safety of a longer span, while a span length of 20 meter for the double span structure was chosen to verify the prestressing profile with smaller radii. In these manual calculations the geometry which results from the Matlab model is verified. In stead of manually designing a geometry. The manual calculations are presented in appendix E and F. The results of the manual calculations have been compared with the Matlab results and are presented in tables E.5 and F.9.

### 8.2 Length

The model analyzes trough bridges for various lengths. These lengths are defined by a minimum and maximum length and a step size of one meter. For each length the model starts over at the beginning of the design process. No calculated values of previous lengths are taken to the next. Table 8.1 shows the evaluated lengths for the different models.

### 8.3 Initial conditions

At the start of the design process the initial conditions are defined. These are the properties which remain constant, like the applied reinforcement (table 3.3), the material properties (Chapter 3) and the initial cross section dimensions.



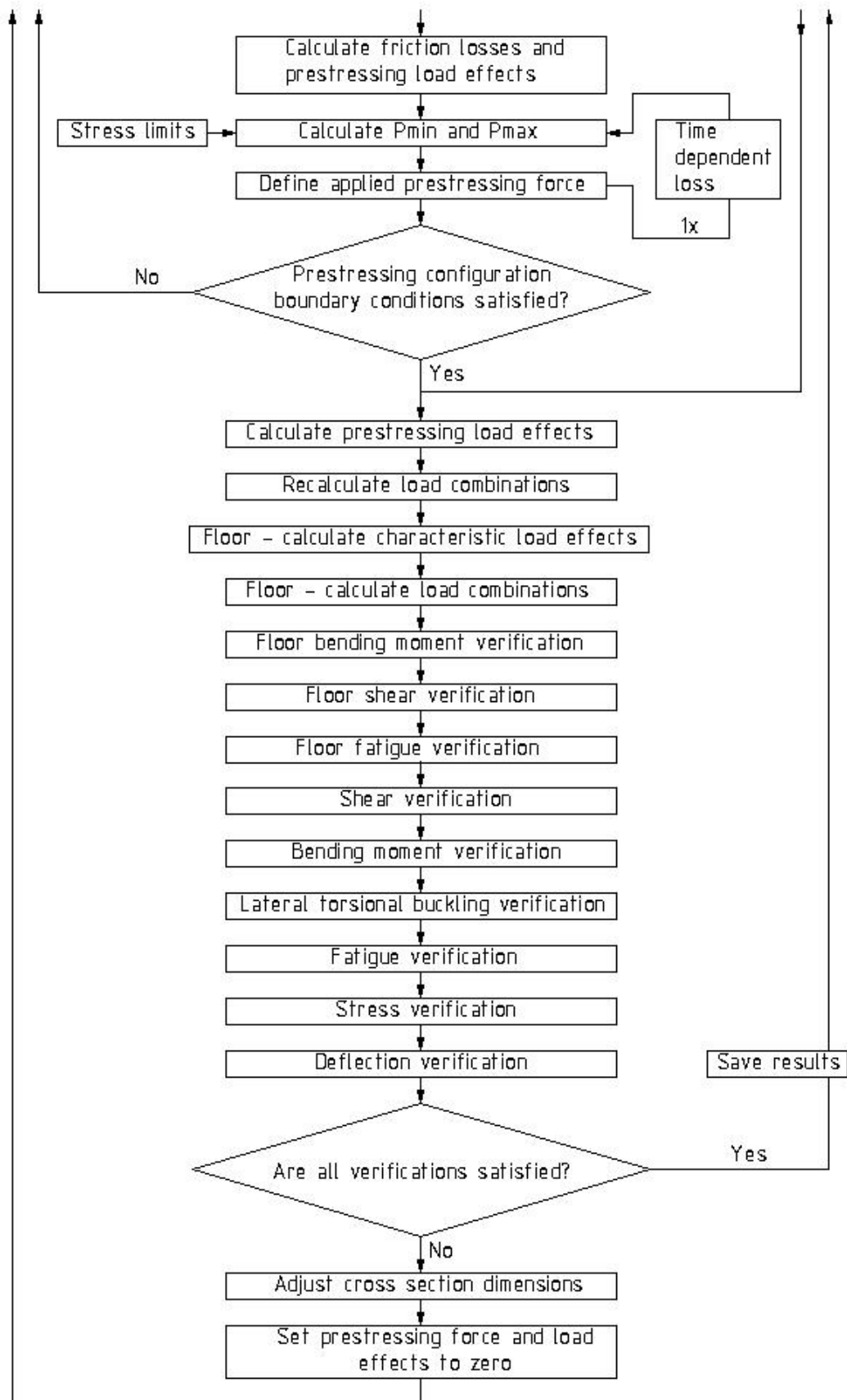


Figure 8.1: Flow chart linear-elastic model.

Model	Lengths	Remark
1 span - UHPFRC	10 - 50 m	
1 span - C35/45	10 - 40 m	Larger spans lead to unrealistic results.
2 spans - UHPFRC	20 - 50 m	Minimum span length of 20 m required to accommodate prestressing curvature.
2 spans - C35/45	20 - 28 m	For longer spans the shear force verification can not be satisfied.

Table 8.1: Evaluated lengths for different models.

The cross section dimensions are at this point defined to be too small to be realistic values. After satisfying all design verifications the model will present a resulting cross section which is optimized in terms of cross sectional area. The initial cross section dimensions are given below.

Dimension	Symbol	Size
wall height - single span	$h$	400 mm
wall height - double span	$h$	1200 mm
wall thickness	$b_w$	200 mm
floor thickness - UHPFRC	$t_b$	300 mm
floor thickness - C35/45	$t_b$	680 mm
internal width	$b_i$	4000 mm
outer width	$b_d$	4400 mm

Table 8.2: Initial cross sectional dimensions.

In the single span structure an initial wall height of 400 mm is applied. In the double span structure this is 1200 mm. This was done to speed up the calculations of the double span structure. Each iteration takes a lot more time for the double span model than for the single span model. The calculation time is reduced by reducing the required number of iterations. In the single span model this goes that fast that the influence on the calculation time can be neglected.

The applied initial floor thicknesses are the same as the results. The required thickness of floor has first iteratively been determined and subsequently been applied as initial dimension. The reason for this is that the model shows instability with regard to the varying floor thickness. As the length of the static model of the floor is defined as the centre to centre distance of the walls, the span length of the floor increases as the wall become wider. This may cause that the verifications for a given floor thickness may no longer be met when the wall thickness is increased. Although the model has been programmed to increase the floor thickness until the floor verifications are satisfied, this may lead to unrealistic results when a too small initial floor thickness is applied. This has been prevented by applying a verified floor thickness as initial dimension. The applied initial floor thickness is not unrealistic as the manual calculation in appendix E shows.

A constant amount of applied reinforcement has been used since the emphasis of the research is on how the concrete cross section changes over varying length. The constant reinforcement allows to make this comparison.

## 8.4 Loads

### 8.4.1 Static loading

The model makes use of superposition of the load effects. By applying the displacement method for each load case, the moment- and shear force distribution line can be defined in an analytical expression. Due to symmetry this expression is evaluated for 'n' points over half the length of the beam. Later on in the design process this allows to find the corresponding bending moment distribution with the maximum shear force.

### 8.4.2 Mobile load model

The Matlab model is required to calculate the maximum loading for each static system of varying length. Due to the load models LM71 and SW/0 and SW/2 consisting of point loads, distributed loads and block loads, the position of the load can not be expressed as a constant times the length of the structure. Especially in the case of the SW load models, in combination with statically undetermined systems, a large spread in the position of the load in order to obtain the maximum internal forces can be seen for a varying length of the system. This spread would introduce an error in the results which has been considered too large to permit, as this could lead to unrealistic results in the research.

A solution to this was found in moving the load model over the length of the structure with steps of one meter. Each position will give it's own moment and shear distribution. From these, the model will continue with the governing load distributions.

The internal bending moments are determined by use of the displacement method. As a load configuration is placed upon the structure it divides the structure in certain intervals. These intervals are connected by boundary- and matching conditions. This leads to a set of equations and unknowns which can be solved. This was done analytically in the computer program Maple. These equations were then imported into the Matlab model. The model determines in which interval the considered cross section is placed and then calculates the internal bending moments. Figure 8.2 shows a schematic overview of the possible positions of a SW load on a two span structure, with its corresponding intervals.

At this point the moment line in the structure is known. The shear force is the derivative of the bending moment. To find the shear force line the bending moment line has been approached with a fourth degree polynomial. This allows Matlab to find the analytical derivative. This equation is now evaluated for 'n' points. The result is the shear force line.

Load models SW/0 and SW/2 consist of two spread loads of a fixed length and distance of each other. These loads have to be applied also in the case they work favorable. The load model LM71 consists of four point loads with a fixed configuration and two spread loads of undefined length. These spread loads have been applied only at the areas where they work unfavorable. These areas have been determined by making use of influence lines. This causes that there are different load positions for the maximum shear force and the maximum field moment.

The results for each static system, of each length, can be plotted as the envelop of the internal characteristic forces.

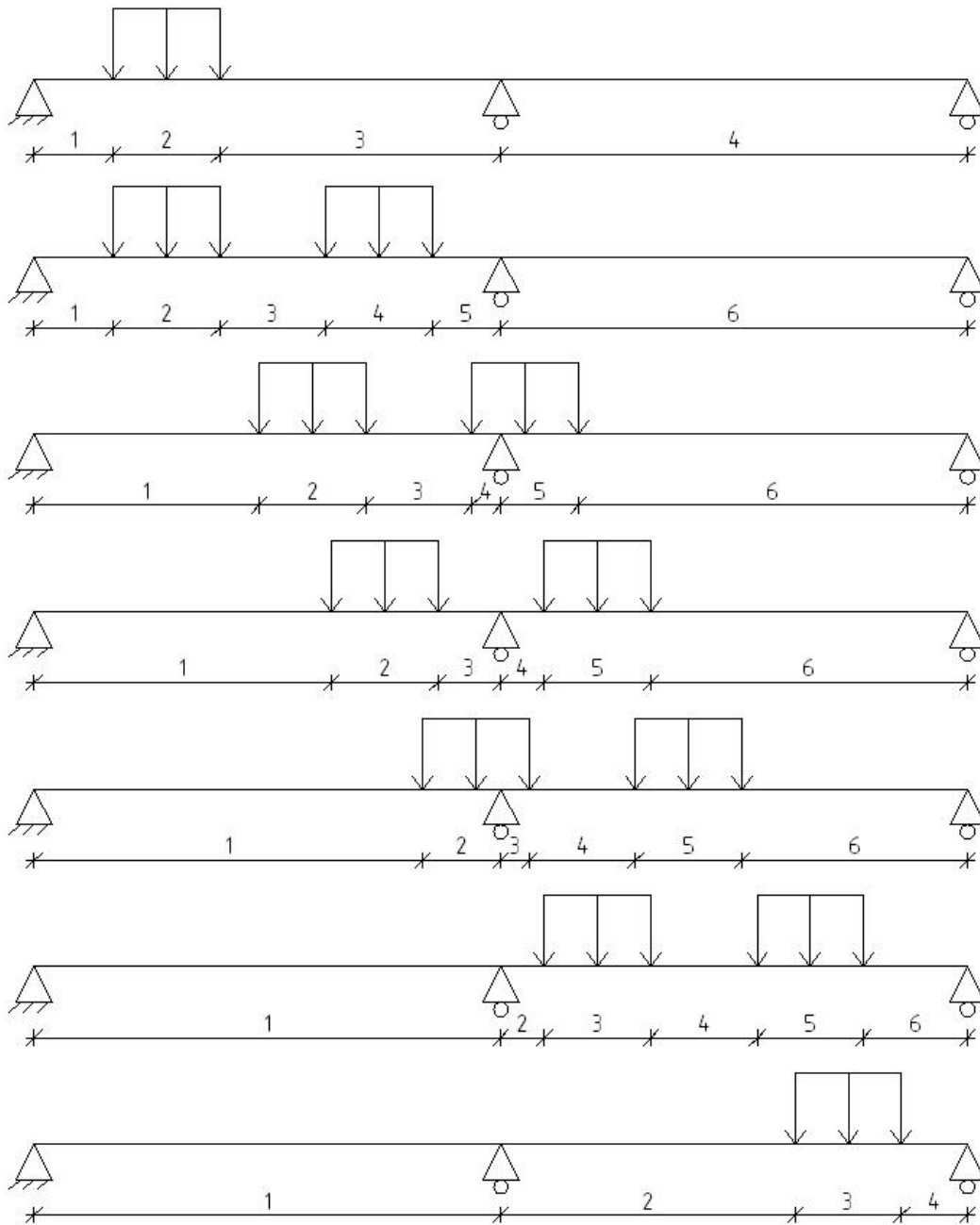


Figure 8.2: Schematic overview of possible load locations of SW load model on double span structure with corresponding mathematical intervals.

### 8.4.3 Load combinations

Section 4.4 shows how the load combinations are defined. In the model the factor  $\Psi$  and  $\gamma$  are defined in matrices. These matrices have a number of rows which correspond with the number of load cases and a number of columns which correspond with the number of load combinations. Also the characteristic load effects have been combined in a matrix. The number of rows of this matrix corresponds with the number of load cases and the number of rows are the 'n' evaluated points over half of the length of the structure.

The definitions of the load cases in the various limit states can be generalized to:

$$E_d = \gamma \cdot \Psi \cdot G_k + \gamma \cdot \Psi \cdot P + \gamma \cdot \Psi \cdot Q_k \quad (8.1)$$

In the model with the matrices this equation becomes:

$$E_d = (\Psi \circ \gamma)' \cdot E_k \quad (8.2)$$

In which:

$\Psi$	$[a \times b]$
$\gamma$	$[a \times b]$
$E_k$	$[a \times n]$
$E_b$	$[b \times n]$
$a$	number of load cases
$b$	number of load combinations
$n$	number of evaluated cross sections
$\circ$	pointwise multiplication

The generalization of equation 8.1 can be used under certain conditions. In load combinations where no factor  $\Psi$  is present the factor  $\Psi = 1.0$ . For load cases which are not present in a load combination the factor  $\Psi = 0$ . The result of equation 8.2 is a matrix  $E_d$  with  $b$  rows and  $n$  columns. Each row stands for the design load effects of a certain load combination.

At this point the prestressing force is still an unknown. However, the load effects have been taken into account in the matrix  $E_k$  with a constant value of  $E_{p,k} = 0$  [-]. This has been done to make the load combination function applicable at all points during the design process. Later on the input in  $E_k$  for the prestressing load effects is redefined.

## 8.5 Prestressing

### 8.5.1 Strands

An assumption was made for the size of the applied prestressing cables. Based on this assumption a minimum required wall thickness can be calculated. This wall thickness is a function of the duct size, as the wall at least needs to be wide enough to fit two ducts with intermediate spacing next to each other.

### 8.5.2 Friction losses

The idealized tendon profile through the center of gravity of the prestressing cables is described by one parabola  $g(x)$  in the statically determined structure and by three parabolas in the structure with two spans. The angular rotation is defined by their derivatives. The parabolas are defined by their boundary conditions: the eccentricity of the tendon profile at the origin and at the ends. As the cable configuration changes, so does the eccentricity. The recalculation of these eccentricities

make it possible to redefine the parabola and therefore calculate the friction losses for the new cable configuration.

The friction loss is calculated by:

$$P(x) = P_0 \cdot e^{-\mu \cdot (\Delta\theta + k \cdot x)} \quad (8.3)$$

This function is evaluated at the points where the derivative changes sign and at the interface between the parabolas. This gives the prestressing force after frictions losses without wedge settlement.

The wedge settlement can be calculated by:

$$l_{set} = \frac{w_{set} \cdot E_p}{\frac{\Delta\sigma_p}{\Delta x}} \quad (8.4)$$

In this the expression  $\Delta\sigma_p/\Delta x$  is the slope of the expression 8.3. Before wedge settlement losses the prestressing at the edge  $x = 0$  is  $P(x)/P_0 = 1.0$ . After wedge settlement losses this is  $P(x)/P_0 = 1 - 2 \cdot l_{set} \cdot \Delta\sigma_p/\Delta x$ . A linear function for  $P(x)/P_0$  after wedge settlement is defined by  $P(x)/P_0 = 1 - 2 \cdot l_{set} \cdot \Delta\sigma_p/\Delta x + x \cdot \Delta\sigma_p/\Delta x$ . This function intersects  $P(x)/P_0$  before settlement at  $x = l_{set}$ .

The two functions for  $P(x)/P_0$  before and after wedge settlement are evaluated at  $2 \cdot n + 1$  points over the length of the structure for the one side tensioned single span structure and at  $n$  points for the statically undetermined structure which is symmetrically tensioned at both sides. This makes from the functions  $P(x)/P_0$  two vectors of the size  $[1 \times n]$ . The actual prestressing force  $P(x)/P_0$  after wedge settlement is now defined by a vector of the size  $[1 \times n]$  in which the value for each entry is the smallest of two initial vectors. The mean prestressing force can now be calculated from this vector.

### 8.5.3 Maximum and minimum prestressing force

The OVS sets certain boundary conditions to the maximum allowed tension stress in the concrete. These boundary conditions have been described in a data set and are dependent on the load combination and the position of the evaluated fibre with respect to the position of the prestressing cable. All boundary conditions have been evaluated by a cross-section analysis. In this evaluation the boundary condition is being extracted from the data set by predefining the location of the fibre and the load condition.

<i>Load combination</i>	<i>Near cable</i>	<i>Away from cable</i>
<i>Construction</i>	$\sigma_c \leq f_{ctm} \leq 3$	$\sigma_c \leq f_{ctm} \leq 3$
<i>Frequent</i>	0	$0.5 \cdot f_{ctk} \leq 1.5$
<i>Characteristic</i>	$0.5 \cdot f_{ctk} \leq 1.5$	$0.75 \cdot f_{ctk} \leq 2.25$
<i>Quasi – permanent</i>	0	0

The boundary conditions have all been evaluated and all lead to a certain maximum allowed or minimum required prestressing force. Depending on the location of the evaluated cross section the minimum and maximum prestressing force are found at the top or bottom. The boundary conditions for the prestressing force are defined by the largest minimum and smallest maximum prestressing forces.

Due to the equations which calculate the required prestressing force to obtain a certain tensile stress it may occur that the required prestressing force is negative. This means that without prestressing force the stress will be a lower tensile stress or even a compressive stress. When this occurs the model takes for the prestressing force  $P = 0 \text{ kN}$ .

The prestressing forces at  $t = \infty$  are transposed to the initial prestressing forces at  $t = 0$  by making use of the time dependent losses. At first these are estimated to be 15%.

The chosen initial prestressing force  $P_0$  is the smallest required force. This minimizes the required amount of prestressing which should have a positive effect on the costs of the structure.

#### 8.5.4 Applied prestressing force

The initial prestressing force  $P_0$  is before friction losses and wedge settlement. The mean prestressing force after wedge settlement was calculated as a percentage of the initial force. The mean prestressing force  $P_{m,0}$  at  $t = 0$ , and the mean prestressing force  $P_{m,\infty}$  at  $t = \infty$  are calculated.

From the initial prestressing force and the maximum allowed steel stress the required area of prestressing steel is calculated. The size of the prestressing strands remains constant and the number of strands per cable are known so the cable area can be used to calculate the required amount of cables. The amount of cables is defined such that it is always a number which can symmetrically be divided over the two trough walls and such that always an even number of cables is placed in each wall. This allows the cables to always be placed in pairs next to each other.

As the applied prestressing is known the actual initial stress can be calculated.

#### 8.5.5 Time dependent losses

With the calculated applied prestressing force the actual time dependent losses can be calculated. This has been done relatively easy by evaluating the theoretic equations. As from the prestressing boundary conditions it may occur that no prestressing is required, the prestressing area may be found to be zero. The equations for relaxation and creep losses require a division by the prestressing area. This is not possible when the value for  $A_p$  is zero. When the prestressing area is zero the relaxation and creep losses are also set to be zero. In practice this mean that no creep and relaxation will occur when no prestressing is present.

#### 8.5.6 Cable configuration

There are numerous ways to apply the prestressing cables. The positions, amount of strands and amount of cables are the main variables in this. To reduce the number of possibilities certain boundary conditions have been applied. At the head of the structure the tendon profile is situated as much as possible towards the neutral axis of the cross section, this is for both this statically determined and undetermined structure. In the statically undetermined structure the tendon profile above the mid support is situated as high as possible. The model does take into account the required area for the anchor plates to be placed.

Step	Description
1.	Define cable size.
2.	Alter cross section dimensions.
3.	Recalculate cross sectional properties.
4.	Recalculate load combinations.
5.	Recalculate friction losses.
6.	Recalculate minimum and maximum prestressing force.
7.	Recalculate actual time dependent losses.
8.	Recalculate applied prestressing force.
9.	Verify boundary conditions.
10.	Accept or alter cable configuration.

Table 8.3: Iterative steps in defining the cable configuration.

The model finds its cable configuration on an iterative manner. The steps it goes through are described in table 8.3. At the basis of the choice for a cable configuration there is a data set with

possible cable compositions in terms of number of strands per cable, the outer diameter of the duct and the size of the anchor plates.

$$\begin{array}{c}
 \text{index} \\
 1 \\
 2 \\
 3 \\
 4 \\
 5 \\
 6
 \end{array}
 \begin{array}{c}
 n_{strands} \\
 \varnothing_{duct} \\
 w_{anchor} \\
 h_{anchor}
 \end{array}
 \begin{array}{c}
 \\
 \\
 \\
 \\
 \\
 \\
 \end{array}
 \end{array}
 \quad (8.5)$$

The number of cables and strands have already been calculated (section 8.5.1 and 8.5.4). For this the same data set has been used. The model starts at index 1. The thickness of the wall is dependent on the diameter of the prestressing ducts. Therefore the wall thickness  $b_w$  is recalculated. Since the geometry has now been altered the section properties and the load effects of the self weight are recalculated.

As the sectional properties and the load are altered this may have influenced the boundary conditions for the prestressing force. Therefore the model again goes through the calculations of the load combinations, friction losses, maximum and minimum prestressing force and the applied prestressing force (step 3 to 8 in table 8.3). Now the number of cables are known, the actual eccentricity, and thus the actual prestressing profile, of the prestressing cable can be taken into account.

Now certain conditions have to be met for the model to accept the cable configuration (step 9). First, with respect to the height. These conditions are that the height of the wall has to be equal to, or greater than the minimum required height. This required height is calculated as a function of the number and size of the anchor plates which need to be placed at the edge of the structure. Secondly the model checks if the center of gravity of the cables at the lowest and highest points is situated with an eccentricity at the desired side of the neutral axis of the cross section. Finally the model checks if the number of cables is equal to or lower than the maximum allowed cables.

When all these conditions are met, the model continues to the next step (section 8.5.8). Depending on which condition isn't met the model takes a different action (step 10). In case the number of cables is greater than the maximum, but the index is below six, the index is raised with one. This increases the number of strands per cable and therefore the required prestressing area can be achieved with less cables. As the duct diameter and the anchor plates increase so does the geometry. Step three through ten from table 8.3 are gone through again.

When the number of cables and the index are respectively greater than and equal to their maximum, this indicates that the required prestressing force is too large for the largest allowed prestressing area. In this case the model will increase the height of the structure. This results in larger section moduli and therefore in a lower required prestressing force. Then the model goes again through step three to ten.

When the eccentricity of the prestressing cables is at the wrong side of the neutral line of the cross section the height of the structure is increased. As the area of the floor remains the same and more mass is placed upward the neutral line will be located higher.

This process of iteration keeps running until all boundary conditions are satisfied.

### 8.5.7 Anchor heads

The data set 8.5 gives information on the size of the anchor head for each cable. These anchor heads need to be placed at the end of the structure and should fit within the cross section and have sufficient intermediate spacing. As the anchor heads are much larger than the duct diameter, the wall will have to be thicker due to the anchor heads. In order to save material the wall thickness will therefore

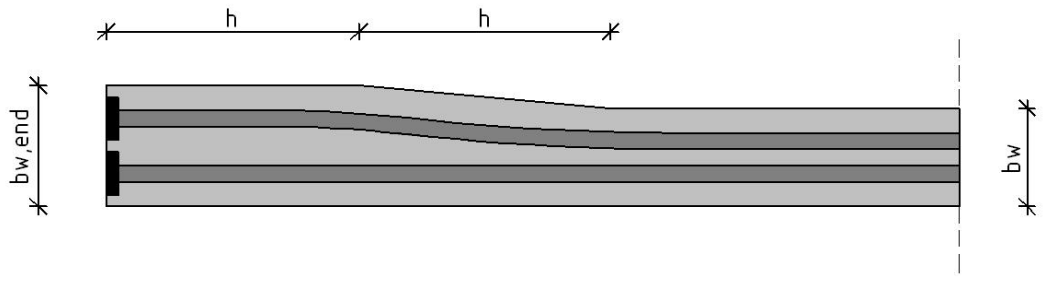


Figure 8.3: Principle detail of widening of the wall to accommodate the anchor plates.

be reduced after a length equal to two times the height to the minimum required thickness due to the ducts. The increased thickness is applied to the outside of the cross section as to not to come in conflict with the clearance cross section. Figure 8.3 gives the principle. The forces due to the horizontal curvature have not been detailed.

### 8.5.8 Prestressing load effects

As the final cable configuration and the actual prestressing force have been determined, the load effects of the prestressing force can be calculated. The load effects due to prestressing have analytically been determined in Maple and consequently been transposed to Matlab. The load effects of the prestressing force are already an entry in  $E_k$  in equation 8.2. Up to this point their value was zero however. The entry of the prestressing load effects is now defined. By applying equation 8.2 the load effects of the prestressing force are combined with the external loadings.

## 8.6 Verifications

### 8.6.1 Shear capacity

In de mobile load model the largest occurring shear force due to a mobile load is found. The position of the mobile load to obtain this maximum shear force is saved as a value  $xV$ . Evaluating equation 8.2 for the shear forces gives a matrix  $V_{d,lc}$  with in each row the shear line for the corresponding load combination evaluated at 'n' points over half of the length. From matrix  $V_{d,lc}$  the maximum shear force line can be found. Its row in the matrix is the load combination where it results from. From the load combination it can be traced back which mobile load (LM71, SW0 or SW2) has been taken into account. Since the location of the load  $xV$  was saved and the load model is known the bending moment distribution for the load model at this position can be calculated. As this is a characteristic load it is further evaluated into the corresponding load combination to obtain the design value.

Due to the known bending moment line each point on the beam can be evaluated whether it's cracked or not. This results in a shear resistance vector  $V_{Rd} [1 \times n]$  with at each entry the corresponding cracked or uncracked shear resistance. We can now perform the unity check for shear resistance at each point of the structure. This is done by point wise dividing  $V_d$  over  $V_{Rd}$ .

$$\frac{V_d}{V_{Rd}} = \frac{[V_1 \quad V_2 \quad \dots \quad V_n]}{[R_1 \quad R_2 \quad \dots \quad R_n]} = [uc_1 \quad uc_2 \quad \dots \quad uc_n] \quad (8.6)$$

The largest occurring unity check, independent of its position, is taken as the unity check for the flexural shear force.

Besides the flexural shear resistance also the resistance of the compression strut has been verified. Both verifications have been placed in separate unity checks so that they later on can be distinguished.

### 8.6.2 Bending moment capacity

The calculation of the bending moment capacity is based on the multiple-layer-model as this allows to easily take the varying width into account. First the horizontal equilibrium is solved under the assumptions that the compressive strain in the outer compressed fibre reaches the ultimate compressive strain  $\epsilon_{cu3}$ . The length of the compression zone  $x_c$  is increased until the horizontal forces in each layer provide horizontal equilibrium.

At this point the height of the concrete compressive zone has been calculated. This makes it possible to check whether the steel stress remains below the ultimate steel strain  $\epsilon_{su}$ . When this is the case the model will proceed to verify the maximum compression zone height. If the steel strain is larger than the ultimate steel strain this means that the assumption of the reached ultimate compressive strain was wrong. Now the model assumes the strain diagram to pass through the ultimate steel strain. A new horizontal equilibrium will be formulated and solved.

When the horizontal equilibrium and the steel strain are satisfied the model will continue to check the height of the compressive zone with the maximum allowed height. In case this condition is not met it will proceed to calculate a fictive prestressing area and then use this to again solve the horizontal equilibrium as described above.

The largest bending moment can be found in the matrix  $M_{d,lc}$ . Only the load combinations belonging to the ultimate limit state are evaluated for this. The maximum bending moment is divided by two as the trough walls are evaluated as separate beams. Now the unity check can be performed.

### 8.6.3 Lateral torsional buckling

The resistance against lateral torsional instability can simply be evaluated by solving the theoretic equations. The maximum bending moment can be found in matrix  $M_{d,lc}$ .

### 8.6.4 Fatigue

The load combinations for fatigue are taken from the matrix  $M_{d,lc}$ . At the evaluated 'n' points the minimum bending moments are subtracted from the maximum bending moments. The maximum load difference at one point can be taken from this result. The point at which this maximum load difference occurs is determined as well. With this information the minimum and maximum stress at this location can be calculated. The fatigue verification has subsequently been performed according to method I given in the Modelcode 2010.

In case the maximum tensile stress causes the concrete to crack the model goes on to testing the reinforcement- and prestressing steel on fatigue. The largest unity check of both will be placed in the fatigue unity check for that side of the construction.

### 8.6.5 Floor

The loads acting on the floor have been determined on the way described in section 8.4.3. New matrices with the characteristic loads and load effects have been created for the floor. The static model of the floor has been depicted in figure 8.4.

The verifications in the floor have been carried out in the same way as described above with the difference that for most variables, alternative variables for the floor have been created. This makes

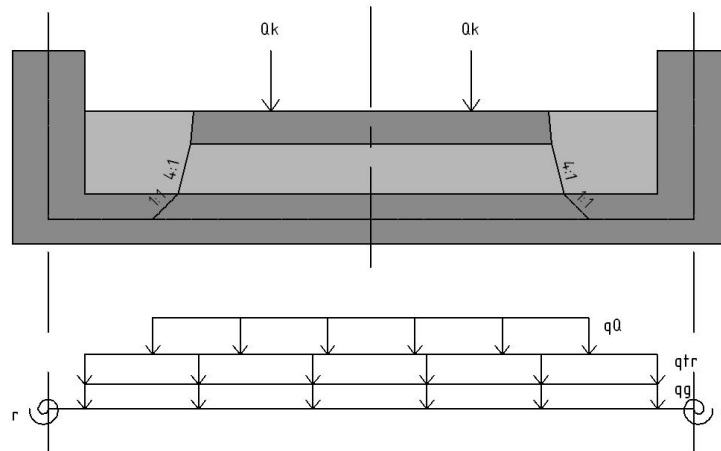


Figure 8.4: Load distribution and static model of the floor in cross direction.

that the data of the main span direction won't get overwritten by values resulting from the floor calculations.

### 8.6.6 Deflection

From the matrix  $M_{d,lc}$  the load combination with the largest bending moment has been determined. The bending moment line has been approached with a polynomial as a function of the symbolic value  $x$  which is the position over the length of the structure. Double integration of this polynomial with the application of the corresponding boundary conditions of the structure gives a function for the deflection. Evaluating this function over 'n' points over the length of the beam gives the deflection line.

The maximum allowable deflection with respect to the vertical acceleration is defined by the graph in figure 6.1. This multi-linear graph can be defined by two  $1 \times 4$  vectors. One sets the values on the vertical axis and the other on the horizontal axis. A linear interpolation function of Matlab gives the resulting value on the vertical axis, with the required value on the horizontal axis as input.

### 8.6.7 Stresses

The demands with regard to the maximum allowable tensile stresses from the OVS have been verified. This was done by performing cross section analysis for the discretized cross sections at the top and bottom side of the structure. The calculated stresses at the outermost fibres were compared to the boundary conditions. This boundary condition is dependent on the load combination and the position of the fibre in relation to the prestressing steel. Figure 8.5 shows a typical graph in which the actual occurring stresses due to the load combinations and the maximum allowable tensile stress are depicted. The area over which the maximum allowable tensile stress decreases is the area where the fibres are situated at the side of the prestressing cable. The figure gives the stresses on one span for the UHPFRC double span structure with span lengths of twenty meters.

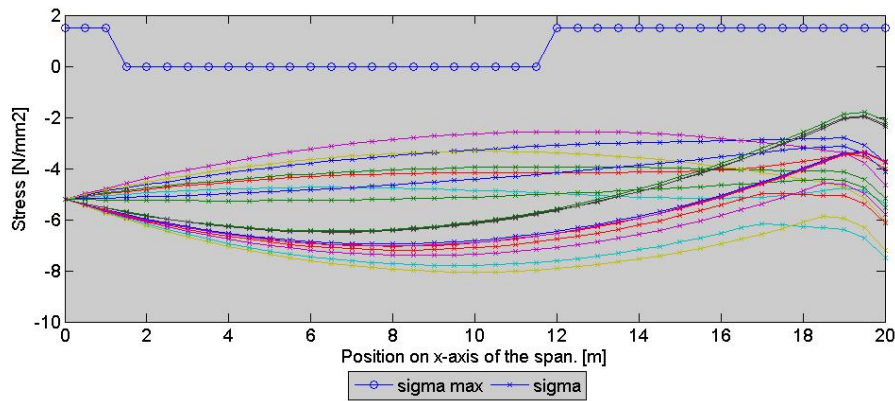


Figure 8.5: Stresses in frequent load combination for one span in the UHPFRC double span structure at the bottom side.

### 8.7 Unity checks

All the unity checks from the performed verifications are put together in a vector. From this the maximum unity check is taken. All unity checks are indexed. This index shows which design aspect gives the highest unity check. With this knowledge the geometry of the cross section will be altered. In such a way that it has the most favorable effect on this design aspect. Table 8.4 shows how the various verifications influence the cross section geometry.

Verification	Increased dimension
Bending moment	Height and width
Shear	Height and width
Fatigue	Height
Deflection	Height
Stresses	Height and width
Lateral torsional buckling	Height and width
Floor - bending moment	Floor
Floor - shear	Floor
Floor - fatigue	Floor

Table 8.4: Influence of the verifications on the cross section.

Now the geometry is altered the entire design process will be started again from the point of calculating the prestressing. Of course after its new section properties and self weight have been determined. This will again lead to a new vector of unity checks. This process will repeat until the largest unity check is below 1.0. All the unity check vectors are documented in a matrix. This matrix gives information on how the unity check develops.

Once all the verifications are satisfied the model will save certain data in memory matrices for future evaluation. Then it will continue to increase the length with the increment and start the entire process over for this new length.

## 8.8 Optimization

As stated before the model starts each length with a too small cross section and continuous to enlarge this until all verifications have been verified. This in contrary to a design method where the cross sectional dimensions are estimated and subsequently the verifications are gone over to see if they are verified. From this perspective it may thus be said that the cross sectional area is optimized.

The cross section is enlarged in such a way as is the most effective for the highest unity check in that iteration. In the cross section three dimensions are variable; the wall height, the wall width and the floor thickness. Table 8.4 shows how the various verifications influence the cross section geometry. Table 8.5 shows the step size of the various dimensions. The step sizes are chosen based on practical considerations. First, a too small step size would considerably increase the calculation speed of the Matlab models. Second, the step size of 50 mm is a practical size in the execution of concrete structures. In the floor this step size of 50 mm would be about 10% of the total floor depth of conventional concrete. Therefore the step size has been reduced to 20 mm to better suite the smaller dimensions of the floor.

Dimension	Step size
Wall height	50 mm
Wall width	50 mm
Floor depth	20 mm

Table 8.5: Step size for cross sectional dimensions.

To show how the step sizes and the model work a short forward reference is made to the results. Figure 8.6 shows the unity checks on deflection for the double span UHPFRC structures of various length. The span lengths of 37 to 40 meters show a unity check which alters between 0.6 and 0.25. To show how this is possible the span lengths of 39 and 40 meters are step by step described.

As the maximum allowable deflection is based on the span length this is constant throughout the iterations. The difference in the unity check must therefore be given in the effective deflection. Of influence on this are the loading and the stiffness of the structure. The stiffness is determined by the moment of inertia as the young's modulus remains constant.

Table 8.6 shows how the cross sectional dimension of both structures are influenced by the iterations. The model requires for both structures six iterations to satisfy all verifications. The first aspect of interest in this table is the fact that the floor and the wall width are the same for both spans

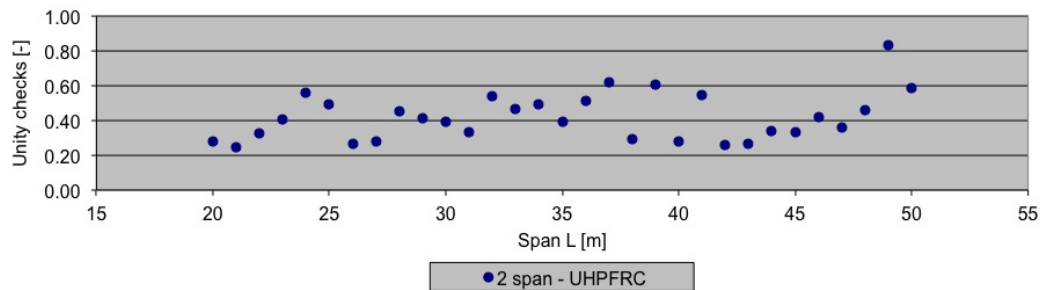


Figure 8.6: Verifications on deflection against span for UHPFRC double span structure.

L=39 m	Start	Iteration: 1	2	3	4	5	6
Wall height	1200	2470	2530	2590	2650	2710	2770
Wall width	200	504	554	604	654	704	754
Floor depth	300	300	300	300	300	300	300
Outer width	4400	5008	5108	5208	5308	5408	5508
L=40 m	Start	Iteration: 1	2	3	4	5	6
Wall height	1200	2460	2520	2580	2640	2700	3160
Wall width	200	504	554	604	654	704	754
Floor depth	300	300	300	300	300	300	300
Outer width	4400	5008	5108	5208	5308	5408	5508

Table 8.6: Cross sectional dimensions on each iteration for double span structure with span length 39 and 40 meters.

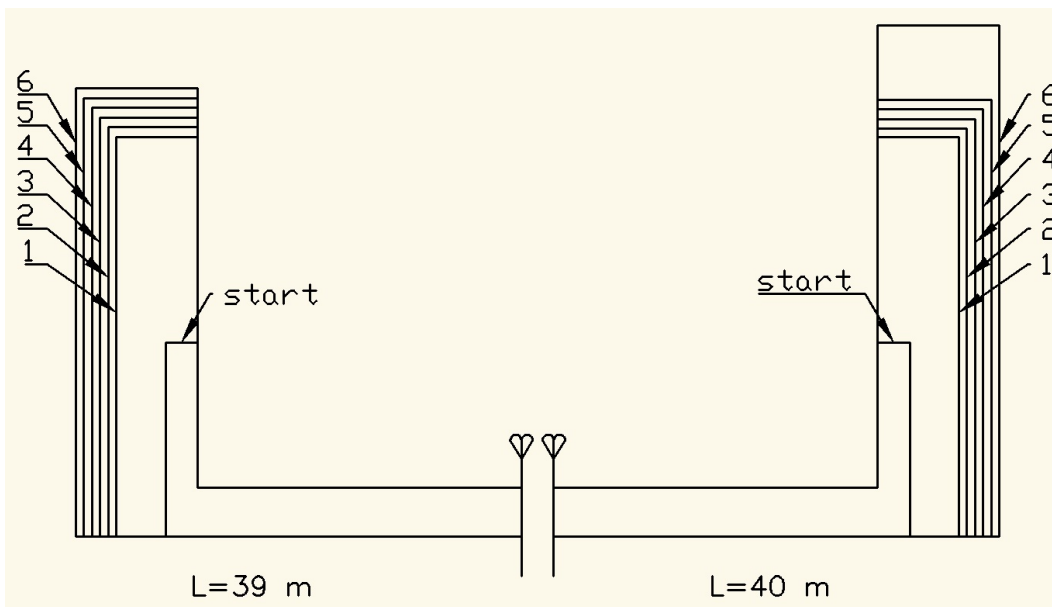


Figure 8.7: Development of the cross sectional area throughout the iterations for L=39 and L=40.

on each iteration. As this is the only aspect influencing the moment of inertia of the structure it is now interesting to see how the height of the structure is determined.

As can be noted in table 8.6 the step size for the height of the wall is not 50 mm, but 60 mm. This indicates that after each iteration, where the height was increased with 50 mm because of an unsatisfied verification, somewhere else in the model the wall height is increased another time with 10 mm. This happens in block B in the model flow chart (figure 8.1). There are only a limited amount of possible cable configurations between number of cables and strands. When the combination with the largest prestressing steel area is applied and the boundary conditions are not yet met, the height of the structure is increased. As this was already increased by 50 mm the applied step size here is kept to be 10 mm to prevent too large steps between the iterations from occurring. This step size of 10 mm in this part of the model is also the reason why the difference between the initial cross

L=39 m	Iteration: 1	2	3	4	5	6
u.c. fatigue field bottom	0.30	0.28	0.27	0.25	0.24	0.23
u.c. fatigue field top	0.75	0.69	0.65	0.61	0.57	0.54
u.c. fatigue support bottom	0.64	0.61	0.58	0.55	0.53	0.51
u.c. fatigue support top	0.20	0.14	0.13	0.12	0.11	0.11
u.c. lateral torsional buckling	0.53	0.49	0.48	0.46	0.45	0.45
u.c. moment field	0.34	0.32	0.32	0.32	0.32	0.33
u.c. moment support	0.17	0.17	0.17	0.17	0.17	0.17
u.c. shear compressive strut	0.28	0.26	0.24	0.22	0.20	0.19
u.c. shear	0.32	0.30	0.28	0.27	0.25	0.24
u.c. characteristic bottom	-7.13	-6.79	-6.46	-6.15	-5.86	-5.59
u.c. characteristic top	3.56	2.74	2.05	1.53	1.13	0.82
u.c. frequent bottom	-7.53	-7.05	-6.59	-6.16	-5.77	-5.40
u.c. frequent top	0.35	0.09	-0.15	-0.29	-0.36	-0.39
u.c. quasi-perm. Bottom	-7.93	-7.70	-7.45	-7.22	-7.02	-6.83
u.c. quasi-perm. Top	-8.14	-8.07	-7.95	-7.82	-7.66	-7.50
u.c. deflection	0.99	0.88	0.80	0.72	0.66	0.60
		Floor				
u.c. fatigue field bottom	0.04	0.04	0.04	0.04	0.04	0.05
u.c. fatigue field top	0.26	0.27	0.27	0.28	0.28	0.29
u.c. fatigue support bottom	0.25	0.25	0.26	0.26	0.26	0.27
u.c. fatigue support top	0.04	0.04	0.04	0.04	0.04	0.04
u.c. moment field	0.87	0.89	0.90	0.92	0.94	0.95
u.c. moment support	0.83	0.84	0.85	0.86	0.88	0.89
u.c. shear	0.07	0.07	0.07	0.07	0.07	0.07
u.c. compressive strut	0.11	0.11	0.11	0.11	0.11	0.11

Table 8.7: Unity checks on each iteration for double span structure with span length 39 meters.

section dimensions and those after the first iteration are not a multiplication of 50 mm. On the first iteration the model will have to go through this loop a number of times until the boundary conditions are satisfied.

For the span length of 40 meters the wall height between the fifth and sixth iteration is not 60 mm but 460 mm. This means that within one iteration the model goes through the cable configuration loop  $(460 - 50)/10 = 41$  times. This results in a high moment of inertia and resistance to deflection. Further investigation on this phenomenon shows that the model goes on to redefine the prestressing configuration even though the boundary conditions are satisfied. This is due to a starting condition in block A which causes that on each iteration the model will pass through this section. In this case of the 40 meter span it shows that when this happens non optimized results may occur. This aspect is subject to improvement for better optimization of the results.

The cross section of a structure is most optimized when multiple design verifications approach its limit. Table 8.7 shows the unity checks for each iteration of the double span structure with span length  $L = 39$  m. The table separates the longitudinal and floor unity checks as the floor is almost independently designed.

The table shows that the maximum unity check for the floor is 0.95 on the bending moment verification at the field. This approaches the limit of 1.0 quite close. The floor can therefore be said to be optimized to a certain extent. After all, the floor is still a solid slab, while more material reduction may be achieved when for instance a hollow core is applied. Optimizations like these were

not considered in this research. This is the reason why some of the other verifications remain very low. The fatigue stress at the bottom of the field for example with a unity check of only  $u.c. = 0.05$ . The applied reinforcement was required to satisfy the bending moment verification, but is much more than required to satisfy the fatigue verification.

Although the floor depth remains constant at 300 mm throughout the iterations, the unity checks for the bending moment and fatigue go up, while those for shear remain constant. This is due to the static model of the floor (see figure 8.4) which considers the supports to be located at the center lines of the trough walls. As the trough walls become wider the span length of the floor increases. This influences the occurring bending moments, but not the shear forces as the total vertical load remains the same.

In the longitudinal direction the highest unity check occurs due to the stress verification in the characteristic combination at the top side with a unity check of  $u.c. = 0.82$ . Second to this is the verification on deflection with a unity check of  $u.c. = 0.60$ . This verification was however already satisfied at the first iteration. In fact, all verifications were satisfied at the first iteration except for the characteristic stress verifications. This verification does show a gradual decrease after each iterations, but it does need six iterations which causes the cross section to be less optimized for the other verifications. This shows that the way the model alters the cross section has large influence on the results. Different changes may lead to a better optimized construction.

## 8.9 Limitations

The Matlab model contains a number of limitations which should be taken into account when considering the results. These limitations are caused by two aspects; the modeling of the trough bridge as a two-dimensional structural model and the applied boundary conditions for parametric design.

### 8.9.1 Structural model

The trough bridge has been modeled as a two dimensional structure. The loadings in the longitudinal direction influence the geometry of cross section of the structure, while the loading of the floor influences the dimensions of the floor. As the loading on the floor is the same for each span, the floor dimensions remain the same in each calculation. This causes that for long spans large trough walls are coupled by a relative thin floor. The horizontal stability of such cases has not been evaluated. Although the applied verification for lateral torsional stability does take the connection of the wall to the floor into account, it doesn't take into account its dimensions.

### 8.9.2 Parametric design

The only variable in the model which changes is the input for the length. This means that for each span length the model needs to be able to produce an output which satisfies all the unity checks. Knowing how much time optimizing one individual concrete structure can take, one may imagine the complicated task to program these optimizations in a numerical model. To reduce the complexity of the modeling task and the model itself at certain points boundary conditions have been formulated. A result of this is that the resulting structures are not fully optimized and certain optimization may be found on further detailing one individual trough bridge. A list of applied boundary conditions is given below.

- All applied reinforcement steel is kept constant in all structures (see section 3.3).
- Prestressing cables are applied in multiplications of four.

- The fictitious tendon profile for the two span trough bridges only has limited optimization (see section 8.5.6).
- The UHPFRC single span structure has been evaluated for spans from 10 to 50 meters.
- The UHPFRC double span structure has been evaluated for spans from 20 to 48 meters.
- The conventional single span structure has been evaluated for spans from 10 to 40 meters.
- The conventional double span structure has been evaluated for spans from 20 to 28 meters. This short range was due to the verification with regard to the shear force. As the concrete is cracked the entire shear force will have to be taken by the reinforcement steel. The applied shear reinforcement is insufficient for spans greater than 28 meters.

### 8.9.3 Non-linear model

Since the non-linear model takes the linear-elastic results as starting point, the limitations in the linear-elastic model work through in the non-linear model. Other limitations are:

- In terms of further optimization of the cross sectional area only the height of the walls has been altered.
- Double numerical integration of the curvature distribution to the deflection line introduces a deviation in the results.
- The shear force distribution changes due to the bending moment redistribution. This has not been taken into account and the shear force verification has therefore been performed based on linear-elastic basis.
- The linear-elastic model only evaluated the bending moment over half of the beam. The non-linear model mirrors the bending moment line about the mid-support to approach a bending moment distribution over the entire construction. For the ULS this is a correct solution (chapter 7), but for the SLS this is a quite crude approach.
- The moment-curvature relation for a cross section in UHPFRC contains a downward branch after the ultimate bending moment has been reached. This means that for a certain bending moment, two corresponding curvatures can be found. The applied function in the model is not able to distinguish which curvature should be applied in such case. Therefore the downward branch in the moment-curvature-diagram has been cut off, leaving only consecutive increasing moment-curvature relations. This means that less curvature can be applied in the non-linear model than in reality is the case.



## Chapter 9

---

# Results

### 9.1 UHPFRC - Conventional concrete

#### 9.1.1 Governing design aspects

In the literature study an investigation was performed for conventional concrete bridges to see which design aspects are normative when designing railway bridges. This research was based on design calculations of twelve bridges. From these design calculations the unity checks were collected. Based on these unity checks a statement was given on which design aspects tend to be normative for railway bridges in conventional concrete. The same method is applied here to analyze which design aspects become normative when designing in UHPFRC. They have been compared with the results from the model for a trough bridge in C35/45. Figure 9.1 shows the values of the unity checks resulting from the models with one and two spans performed in UHPFRC and in a conventional concrete C35/45. Negative values have been omitted in this graph for readability of the area between zero and one. In figure 9.2 these values have been normalized. The normalization of the unity checks was done by dividing the unity checks within a project by the highest occurring unity check in that structure. Therefore the value on the vertical axis for figure 9.1 is the unity check and the value on the vertical axis for figure 9.2 is the measure of importance of the design aspect. In which a value of 1.0 stands for the leading unity check in the design of that structure.

$$\text{normalized u.c.} = \frac{\text{considered unity check}}{\text{maximum unity check in structure}} \quad (9.1)$$

The normalization of the unity checks pronounces the forming of clusters of unity checks. Compared to the literature study this effect is much less however. This is caused by the fact that the model brings the unity checks down by altering the structure until the largest unity check is below 1.0. As a result of this the largest unity checks are very close to 1.0 and therefore the normalization causes the the actual unity checks to be divided by a number close to one, which causes that the position of the unity check in the graph hardly changes. This effect shows that the model results are in a way more optimized than the considered projects in the literature study.

Looking at the normalized unity checks there are three aspects which remain fairly the same for UHPFRC and C35/45, the bending moment, fatigue performance and stresses. The design aspects for shear capacity and deflection show substantial differences.

Next to the interpretation of the unity checks the model provides another tool for investigating which design aspects influence the results. As the Matlab model starts with a too small cross section it uses iterations to find a geometry which satisfies all verifications. Each iteration is started by a design aspect for which the unity check was the highest occurring. The information on how many

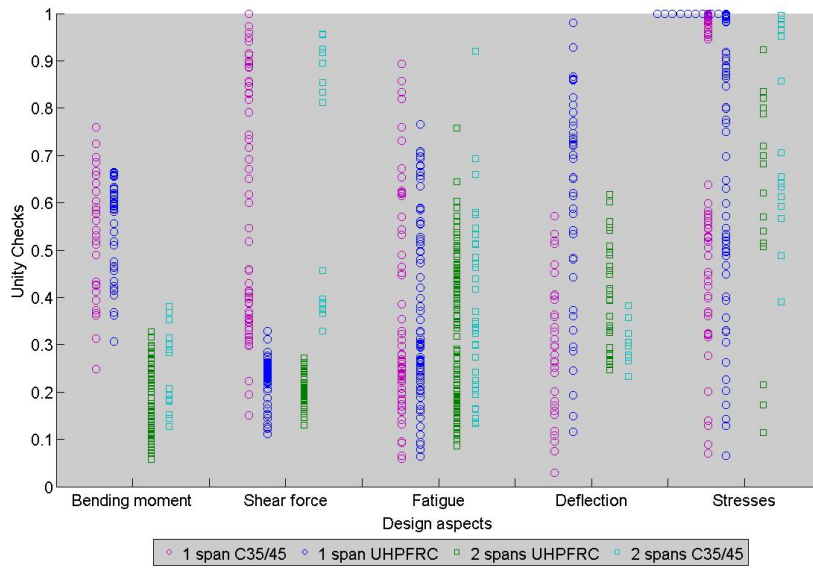


Figure 9.1: Spread of unity checks. Equal values for the same design aspect have been offset horizontally.

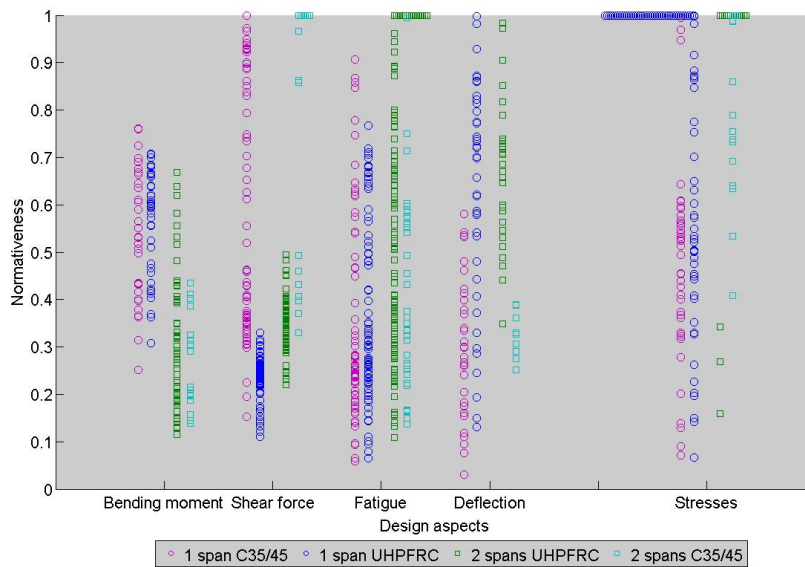


Figure 9.2: Normativeness of design aspect. Equal values for the same design aspect have been offset horizontally.

iterations, and due to which design aspect, can be used to trace back which design aspects were governing in the design.

### Bending moment

Figures 9.3 and 9.4 show that the conventional concrete structures require more iterations and mostly based on bending moment capacity. What happens here is that a certain geometry is found which satisfies the boundary condition  $P_{m0,min} < P_{m0,max}$  so prestressing can be applied. In UHPFRC this geometry also satisfies the other verifications. In conventional concrete the found geometry doesn't satisfy the bending moment verification. Further investigation shows that for the double span structure the bending moment iterations are because the concrete compressive zone height exceeds the maximum. Due to the high compressive strength of UHPFRC this verification doesn't play a role here.

Although the conventional concrete model requires more iterations based on moment capacity, the unity checks show little differences. As was shown in (Ketel et al., 2011) the bending moment capacity for a constant cross section only increases significantly when UHPFRC is applied in combination with the maximum allowable amount of reinforcement.

### Shear force

Compared to UHPFRC the unity checks for conventional concrete on shear are very high. This is due to the shear reinforcement which has been kept constant throughout the different models and has been designed to withstand the occurring shear forces (see section 3.3). The applied shear reinforcement is not sufficient to withstand the largest occurring shear forces. In the double span structure the maximum achievable span is 28 meters. For larger spans the shear verifications can not be satisfied. Therefore the design aspect 'shear force' does not show in figures 9.3 and 9.4. The unity checks for shear force in conventional concrete increase as the span, and the shear force, become larger. They approach one from a span length of 28 meters in both structures.

The normativeness for the shear force shows a characteristic property for conventional concrete where two separate clusters can be identified for both kinds of structures. The verifications considered in the design aspect 'shear force' are both the shear capacity and the capacity of the compressive strut. Figure 9.5 shows for the statically determined structure what causes the formation of the two clusters.

Due to the increased concrete compressive strength of the UHPFRC the capacity of the compressive strut is increased. The unity check for this verification even go as low as 0.20. This is contradictory to the conclusion on shear force in the literature study. In the reference projects was found that the compressive strut was the normative design aspect for the web widths. The reason why this is not the case in these results, is that the reference projects make use of a totally optimized cross section. This model does not. By the applied boundary condition that two prestressing ducts go side by side in the walls, the wall width is determined by this geometrical aspect. This required wall width for the prestressing cables is of such size that the compressive strut gains more than sufficient capacity. Optimizing the wall width could be sought in only a vertical stacking of the cables. This was not applied in this research as it might lead to very high and thin walls which could lead to instability.

The reduced wall width of the UHPFRC structures affects the shear capacity of the wall, but due to the fibers the shear capacity of the material is increased that much that it still leads to larger capacities. Figure 9.5 shows that the unity checks for the shear capacity in UHPFRC are lowered from a range between 0.60 and 0.90 down to about 0.25.

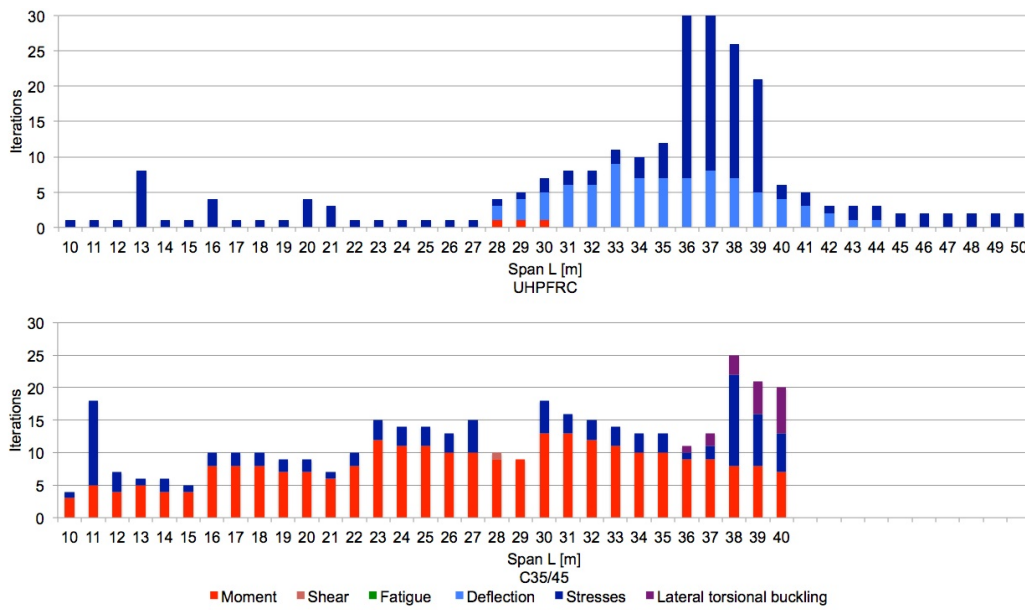


Figure 9.3: Design iterations to span length for single span structure in UHPFRC and C35/45.

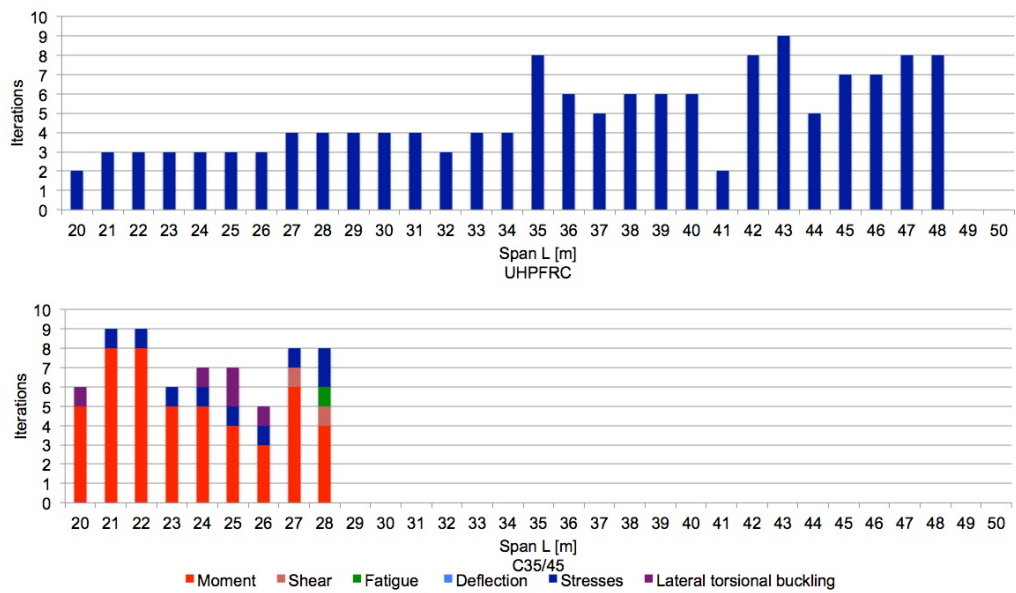


Figure 9.4: Design iterations to span length for double span structure in UHPFRC and C35/45.

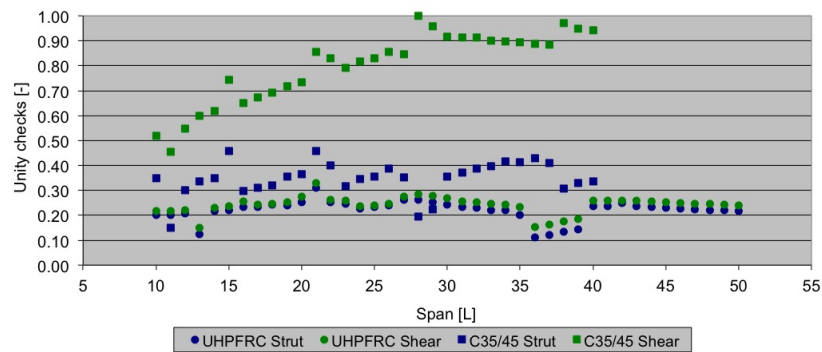


Figure 9.5: Verifications on shear force for statically determined structure in UHPFRC and C35/45.

### Fatigue

For the design aspect 'Fatigue' the unity checks spread a large range, between 0.0 and 0.7. Although this isn't quite approaching the limit, the normalized unity checks for the double span structure show that fatigue is an important design aspect. Certainly much more compared to conventional concrete. In numerous cases fatigue verifications show the highest occurring unity check in the design.

In the design aspect 'fatigue' the verifications for both the top and bottom side of the structure are present and for the statically undetermined structure both the field and mid support cross sections are shown here. In order to gain more insight in which verifications are present in which range, the design aspect 'Fatigue' is split in three cross sections in figure 9.6.

In all structures two clusters of unity checks can be identified. To investigate this aspect the development of the unity checks for the two cross sections in the double span structure have been plotted as a function of the length of the span in figure 9.7. It shows in figure 9.7 that, from a span length of about 33 to 40 meters, the verifications which cause a high unity check start to show a low unity check and vice versa. One explanation could be that the fatigue stress is greater than the concrete fatigue strength and the stress will have to be taken by the reinforcement steel. The Matlab model calculates a unity check for the reinforcement and the concrete fatigue verification. When both are calculated the largest occurring is governing and taken as the unity check on fatigue for that location. As the separate unity checks for the reinforcement and concrete are requested from the calculated data it shows that all unity checks for reinforcement are equal to zero at both the field and the support cross section. This implies that the reinforcement steel is not activated for resisting the fatigue loading and thus that the concrete has sufficient fatigue capacity. This effect can thus not be the case. Evaluation the bending moment lines shows that from a certain span length the direction of the bending moment changes. Consequently, the concrete is no longer verified on compression (with a large capacity), but on tension (with a small capacity). Due to the change in direction the verifications might turn around.

In general for fatigue verifications in the main direction it can be said that they do require attention, but that the high fatigue strength, in both compression and tension, makes that no reinforcement has been applied to accommodate the fatigue capacity.

### Deflection

In the area of the deflection the results show a significant change between the structures in UHPFRC and conventional concrete. For both kinds of structures the unity checks for UHPFRC end up quite

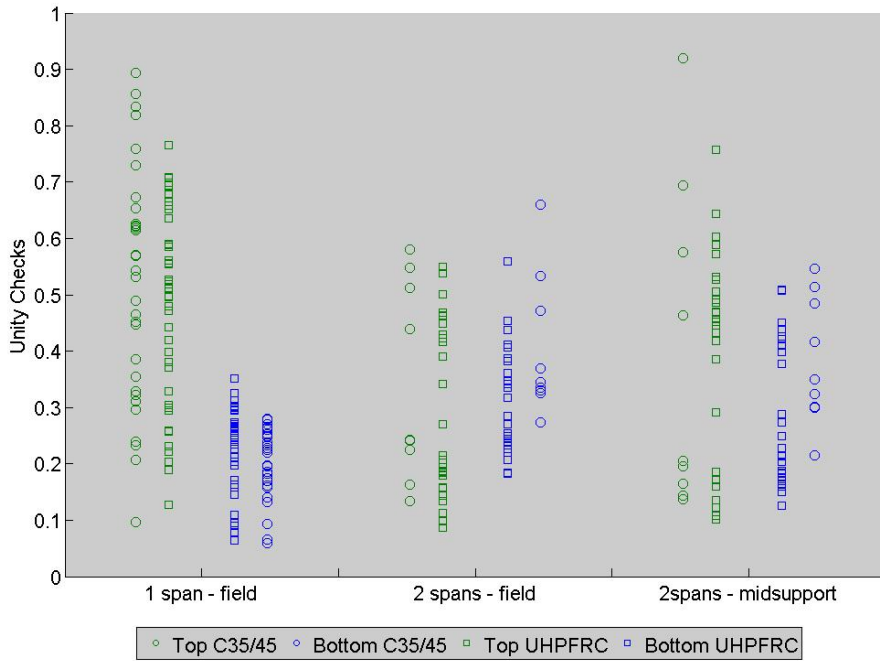


Figure 9.6: Verifications on fatigue for different cross sections.

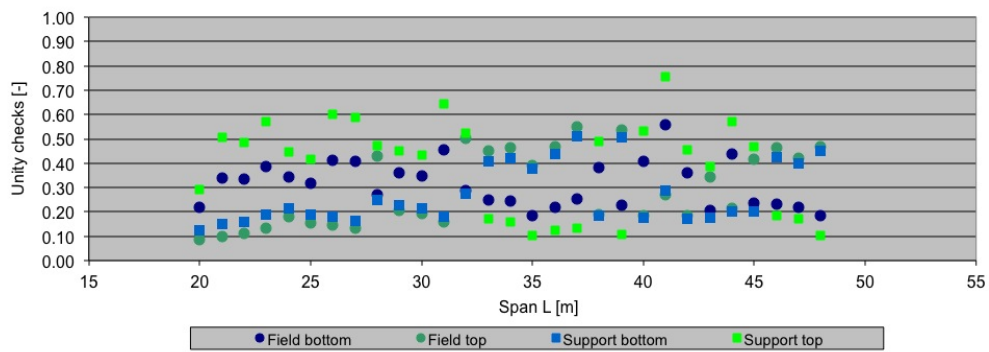


Figure 9.7: Verifications on fatigue against span for double span structure.

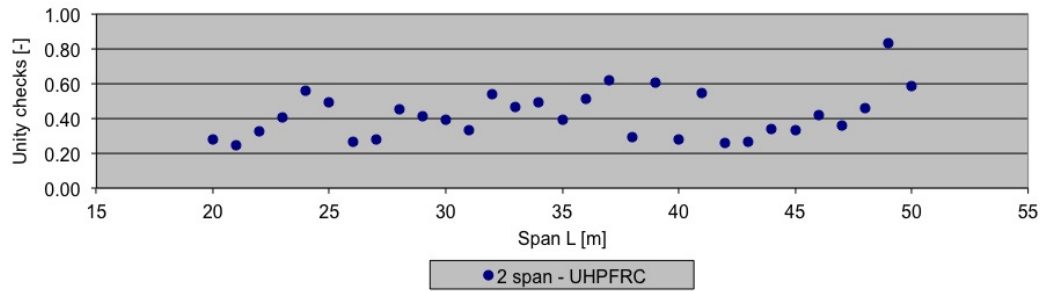


Figure 9.8: Verifications on deflection against span for UHPFRC double span structure.

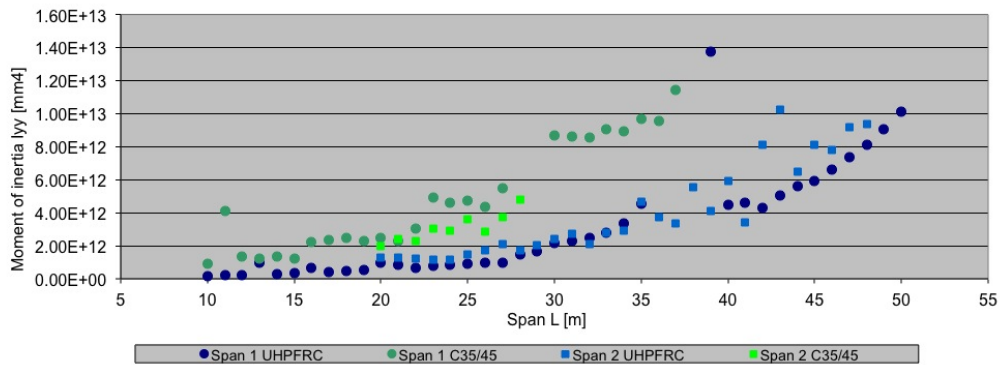


Figure 9.9: Moment of inertia to span length.

a lot higher than for conventional concrete.

The resistance towards deflection is mainly based on the stiffness  $EI$  of the structure. As the modulus of elasticity is kept constant in the model the moment of inertia has the largest influence on the deflection resistance. The moment of inertia (figure 9.9) shows a quadratic development as a function of the span, which corresponds with the linear development of the structure height. The moment of inertia for the double span structures show an average reduction by 50%. For the single span structure this is on average even 75%.

## Stresses

Figure 9.2 shows clearly that the most important aspect of design are the allowable stresses in the serviceability limit state. As well as for conventional concrete as for UHPFRC and as well as in a single or double span structure there are multiple stress verifications that become normative in design. To gain more insight in the different verifications the normalized unity checks for stresses have separately been plotted in figure 9.10. The unity checks below zero (compression stresses) have been cut off for readability. The figure shows that for all kinds of structures the frequent load combination is normative.

The load combinations which becomes normative is dependent on the applied bending moment and the limited tensile stress. Looking at the non-prestressed side of the structure, the difference

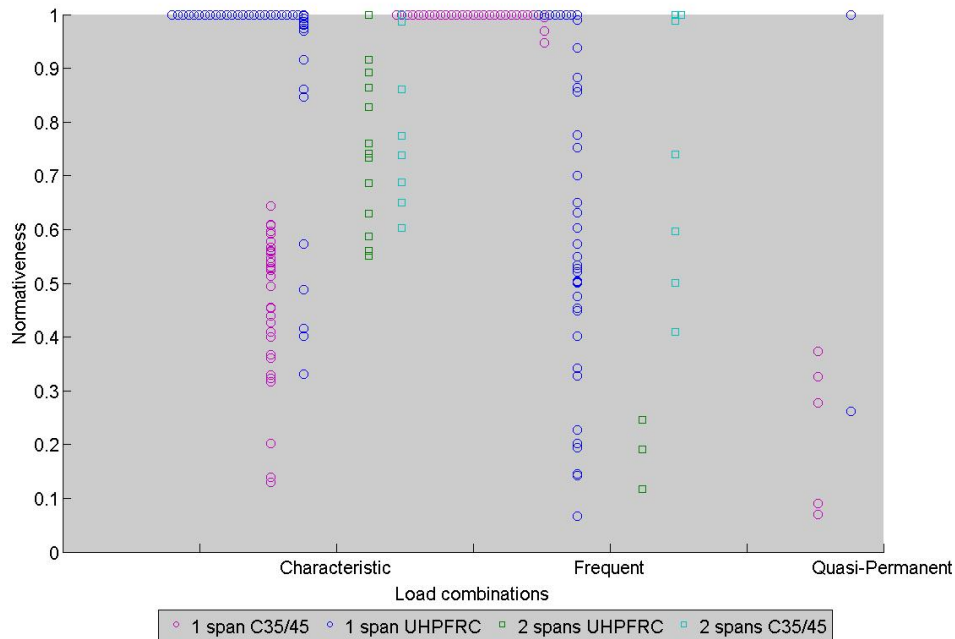


Figure 9.10: Normalized unity checks for stress verifications.

between the characteristic and frequent maximum tensile stress is  $2.25 - 1.50 = 0.75 \text{ N/mm}^2$ . From the characteristic to the frequent load combination this is a decrease of capacity of  $0.75/2.25 = 33\%$ .

This is more than the average decrease in the applied bending moment. In the statically determined structure the decrease in bending moment is on average 28%. Since this is close the capacity decrease there are also situations where the decrease in bending moment is larger than 33%. For these cases the characteristic situation is governing.

The reduction of the bending moment can be explained by table 9.1. This table shows the  $\Psi$ -factor for the load cases which are present in this parameter study. The train loads are the largest loads in this calculation and are therefore taken as the dominant load case. In the characteristic load combination this has no  $\Psi$ -factor and can thus be seen as 1.0. In the frequent combination this is reduced to  $\Psi_1 = 0.8$ . In the characteristic load combination all other variable load cases have to be multiplied with  $\Psi_0$ , in the frequent combination this is  $\Psi_1$ . As the uneven settlement is considered a permanent load case, only the temperature loading and the inspection path load are multiplied with a different  $\Psi$ . The temperature loading is reduced with only 10% for the frequent combination. The inspection path load is not present in the frequent load, but as this load is only  $5 \text{ kN/m}^2$  the overall effect is very small. The differences are larger when the structure is subject to horizontal loads, but these have not been applied in this study (see section 4.3).

As the conventional concrete structures have a larger self weight, the reduced application of the variable loads has less influence on the total load. Percent-wise, the bending moments are thus reduced less in the conventional concrete structures. This explains why the conventional concrete only has normative unity checks in the frequent combination.

The double span structure shows only few unity checks in figure 9.10. Most of the unity checks for the double span structure turn out negative. Meaning that a compressive stress is present where

Load case	Characteristic	Frequent
Self weight	1.0	1.0
Track	1.0	1.0
Train load	1.0	0.8
Settlement	1.0	1.0
Temperature	0.6	0.5
Inspection path	0.8	0.0

Table 9.1:  $\Psi$ -factor for load combinations.

a tensile stress is allowed. Due to the field and support cross sections which have opposing interest in the allowed prestressing force many of the double span structures are fully prestressed.

### Lateral torsional buckling

A design aspect of special interest for UHPFRC structures is lateral torsional buckling. Figure 9.11 shows the resulting unity checks for the verification on lateral torsional buckling. What can be noted in this graph is that in general lateral torsional buckling seems to lead to larger unity checks for the conventional concrete structures than for the UHPFRC structures. This is contrary to the expectations as the walls of the UHPFRC structures have a greater slenderness. To see why conventional concrete structures lead to a higher unity check on lateral torsional buckling the single span structure is further evaluated.

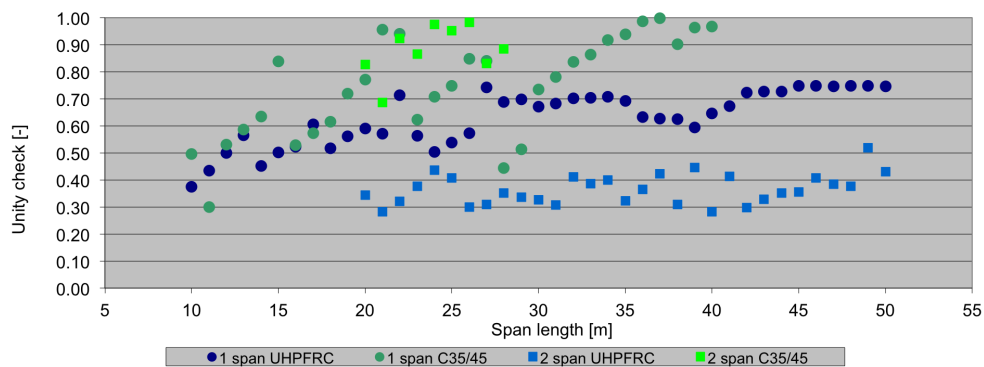


Figure 9.11: Verifications on lateral torsional buckling to span length.

The verification on lateral torsional buckling consists of three different verifications; the normal force, and bending in horizontal and vertical direction (see section 6.1.4 for the background of this verification). The unity check is defined as:

$$\frac{N_{Ed}}{N_{Rd}} + \frac{\overline{M}_{y,Ed}}{M_{y,Rd}} + \frac{\overline{M}_{z,Ed}}{M_{z,Rd}} \leq 1 \quad (9.2)$$

in which:

$N_{E,d}$	effective normal force
$N_{R,d}$	normal force resistance
$M_{y,Ed}$	effective bending moment about y axis
$M_{y,Rd}$	bending moment resistance in y axis
$M_{z,Ed}$	effective bending moment about z axis
$M_{z,Rd}$	bending moment resistance in z axis

Figure 9.12 shows the influence of these three components on the total unity check. Looking at this it makes clear that by far the bending moment in the vertical direction is of most influence and the shape of the graph in figure 9.11 clearly comes back in this. The difference in the vertical bending moment verification however does not explain the difference in the overall lateral torsional buckling verification. Both other aspects, horizontal bending moment and normal force, show a higher unity check for conventional concrete than for UHPFRC.

Many aspects influence the verification on the horizontal bending moment. These are both material property and geometry related. The results show that for the conventional concrete structures the effective bending moment is larger and the moment resistance is smaller than for the UHPFRC structures. These effects have a higher unity check for conventional concrete as result. Of influence on this verification is the Euler buckling load. This is defined as:

$$F_E = \frac{\pi^2 \cdot EI}{L^2} \quad (9.3)$$

For conventional concrete this Euler buckling load will be higher due to the higher stiffness of the structure. This higher Euler buckling load increases the effective horizontal bending moment, since:

$$M_{z2} = \frac{F_E}{k_1} \frac{\bar{v}_0}{n_z^* - 1} \quad (9.4)$$

This shows that although the stiffness of the structure is higher this negatively influence the horizontal bending moment verification of lateral torsional buckling resistance.

The normal force verification is defined as:

$$u.c.tb,N = \frac{\frac{1}{2} P_{m,0}}{b_w \cdot h \cdot f_{cd}} \quad (9.5)$$

As the results (section 9.1.2) show, the prestressing force remains fairly constant for the concrete and UHPFRC structures. The difference in unity check must therefore be caused at the capacity side. Although the wall area of the conventional concrete structures is larger, this is only a factor 1.5 to 3.5. The compressive strength of UHPFRC is however 6.8 times as high. Meaning that although the cross sectional area for UHPFRC is smaller, the normal force resistance is still higher. Leading to a lower unity check on normal force verification.

## 9.1.2 Geometrie

### Height

Figure 9.13 shows for both conventional concrete and UHPFRC how the structure height relates to the length of the span. The literature study shows that for conventional concrete trough bridges the measure for slenderness  $L/h$  is somewhere between 10 and 15. This remains true in the model results for both conventional concrete and UHPFRC.

In general it can be said that for UHPFRC structures the structure height will decrease. The results however show no significant change in the slenderness as this approaches  $L/h = 15$  and can

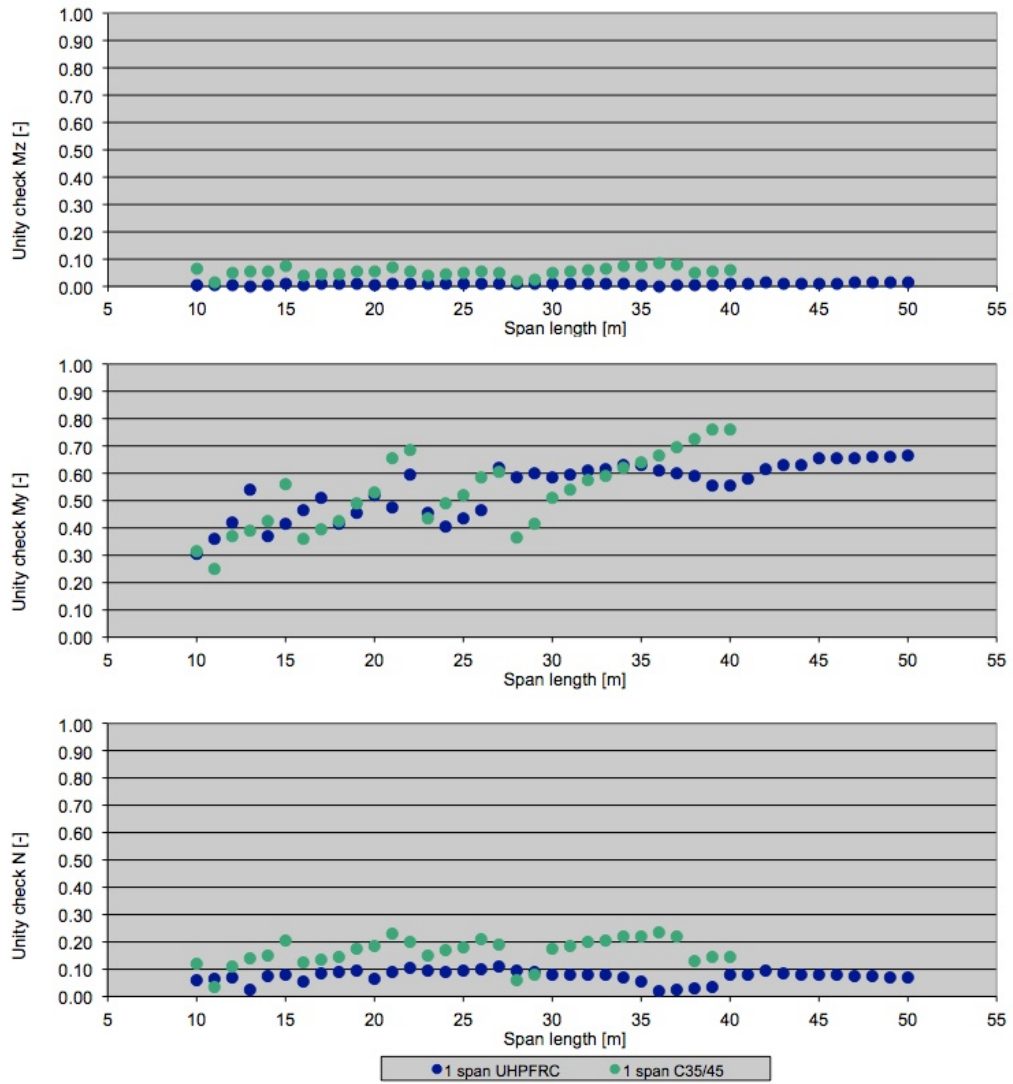


Figure 9.12: The components of lateral torsional buckling verification for the single span structures.

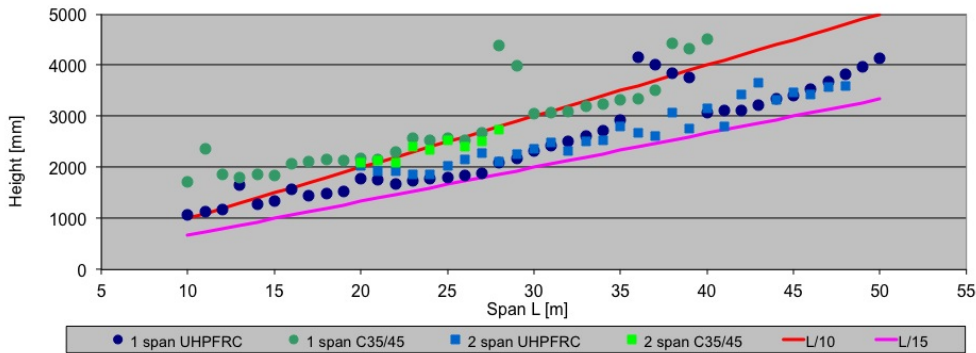


Figure 9.13: Structure height to span length.

also be approached by a well optimized conventional concrete structure. A well optimized trough bridge in UHPFRC may lead to slenderness ratios above fifteen. On average the height reduction of a single span structure is over 600 mm. For the double span structure the height is on average reduced with 300 mm.

**Concrete cross sectional area**

The average reduction in height is of little importance for trough bridges since the construction depth, in relation to the free space below the structure, is determined by the floor thickness. It is however interesting to see how the cross sectional area is influenced by the application of UHPFRC. Due to the higher cost of UHPFRC per cubic meter a decrease of applied concrete can bring the total costs down. Next to the height the wall width is determining for the concrete cross sectional area as the internal width between the walls is constant.

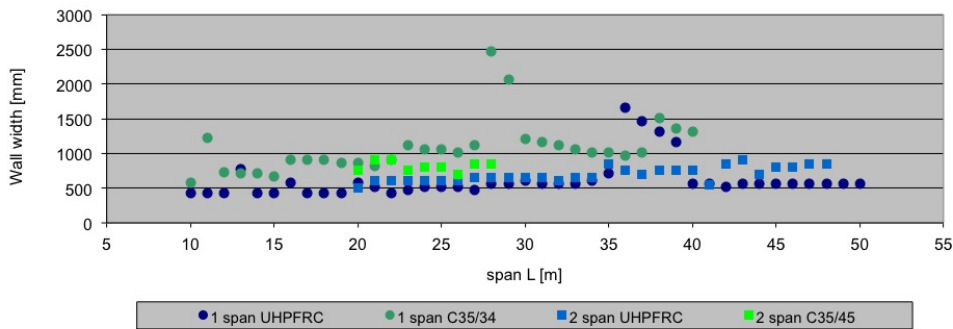


Figure 9.14: Wall width to span length.

The wall width remains fairly constant in the single span UHPFRC structures between 500 and 600 mm. This width is given in by the width required for the combination of the maximum number of cables with the maximum number of strands. The wall width of the C35/45 structure is wider to begin with, but also experiences an increase in size as the span becomes longer. As the maximum

number of cables and strands is the same in C35/45 structures as in UHPFRC, there must be a different aspect which influences the wall width.

The model is based on a too small cross section and increases its size on every iteration until all verifications are satisfied. The dimensions of the cross section are altered based on the verification which gives the highest unity check. The wall width is increased when the verifications of the bending moment capacity, the shear force, the lateral torsional stability and the stresses are not met. The results show that the model requires more iterations for the conventional concrete models than for the UHPFRC structures. Most of these iterations are due to a design aspect which influences the wall width. This is the cause that the wall width in the conventional concrete results are larger than in the UHPFRC structures.

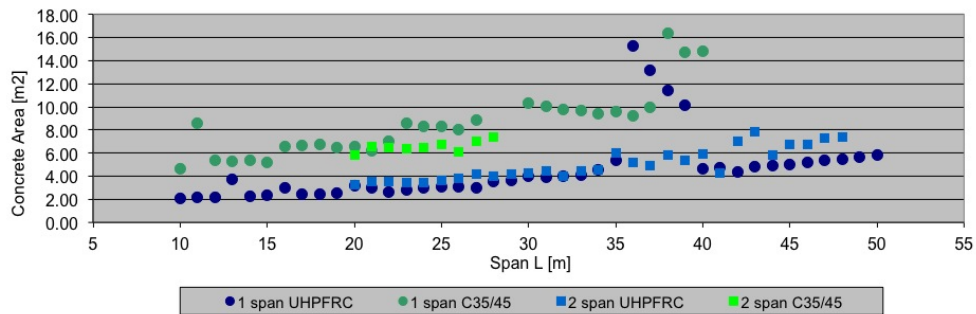


Figure 9.15: Concrete area to span length.

The concrete cross sectional area for UHPFRC trough bridges is substantially smaller compared to conventional concrete. For longer spans the ratio even goes up to a factor two. Although UHPFRC is more dense ( $\gamma_{UHPFRC} = 29 \text{ kN/m}^3$ ) than conventional concrete ( $\gamma_c = 25 \text{ kN/m}^3$ ), this can provide possibilities for precast structures with spans where the ratio between the concrete cross sectional areas is larger than  $29/25 = 1.16$ . This is already the case for spans of 10 meters long and thus it can be said that in this study for all UHPFRC structures the self weight is less than for their conventional concrete counterparts.

### Prestressing

Double span structures in UHPFRC show an application of almost the same amount of prestressing. In the single span structures a decrease in the prestressing force can be noted. This decrease gradually becomes larger as the span length increases. As was mentioned above, the self weight of the UHPFRC is always less than the weight of the conventional concrete structure. This causes that the stresses at the bottom of the cross section, under full loading, become smaller, but that the stresses at the top of the cross section, with only permanent loading, become larger. The Matlab model has been programmed to always apply the minimum amount of prestressing. As in general a lower prestressing force is applied for UHPFRC structures, this suggests that the stress reduction at the bottom fibre has a larger effect than the stress which gives the upper limit.

### 9.1.3 Floor

The literature study has shown that the average floor thickness in conventional railway trough bridges is between 500 mm and 700 mm thick. By making use of ultra high performance fibre reinforced

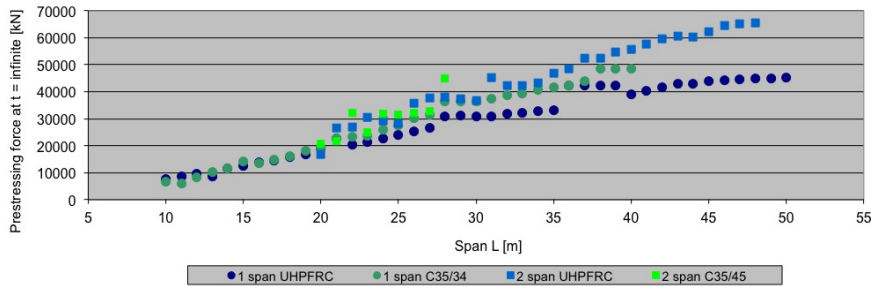


Figure 9.16: Prestressing force to span length.

concrete the expectation is that this thickness can be reduced. This is favorable for the required free height below the structure as the vertical alignment of the rail is often a given demand instead of a design variable.

Two aspects come to light when reducing the floor thickness and applying UHPFRC. One, the steel strain may exceed the ultimate steel strain, and two, the bending moment capacity reduces due to a smaller internal lever arm. To limit the steel strain the thickness of the floor can be reduced such that  $d$  in  $\epsilon_s = \kappa \cdot (d - x)$  becomes smaller. A second measure which can be applied is increasing the amount of reinforcement steel. Due to horizontal equilibrium this will cause a larger concrete compressive force to be activated and therefore an increase of the compressive zone  $x$ . The reduced bending moment capacity due to the smaller internal lever arm can be increased again by increasing the amount of reinforcement since  $M_{ud} = N_s \cdot z$ .

Both aspects suggest an application of a larger amount of reinforcement steel, but have a conflict of interest in the applied thickness of the floor. In this research consensus was found in the application of a UHPFRC floor of 300 mm thick and a reinforcement of  $\varnothing 25 - 125 \text{ mm}$  (1.3% reinforcement percentage). This is a substantial reduction compared to the required thickness of conventional concrete trough floors. A manual verification of this has been performed in appendix E.

The steel fibres add sufficient shear capacity in the trough floor to facilitate the occurring shear forces. The fibre shear capacity is for the floor is 2780 kN, while the concrete shear capacity is only 368 kN. The shear resistance is therefore much more than required ( $V_{Ed, floor} = 302 \text{ kN}$ ) and due to the fibres also guaranteed in cracked cross sections.

The shear compressive strut is not governing here as due to the compressive strength the capacity increases  $172^{\frac{2}{3}}/45^{\frac{2}{3}} = 2.45$  times while the internal lever arm is reduced with a factor  $300/500=0.6$ . Besides that is also the actual shear force reduced due to the lower self weight of the floor.

## 9.2 OVS stress demands

### Allowed tensile stresses

The previous section has shown that the most important design aspect are the stresses in the serviceability limit state. This is likely the effect of the strict demands which the OVS sets to the allowable stresses. As can be seen in table 9.2 the maximum allowed tensile stress is  $3.0 \text{ N/mm}^2$ . This is well below the tensile strength of the UHPFRC which is, in this study,  $f_{ctk} = 10 \text{ N/mm}^2$ . Since this design aspect is leading in the design of the bridge and the material capacity is not fully used it is interesting to see how the design of the structure will behave when the requirements are loosened.

Load combination	Location	maximum tensile stress [ $N/mm^2$ ]
Quasi-permanent	Everywhere	0
Frequent	No prestressing	$0.5 * f_{ctk:0.05}$ or $\sigma_c < 1.5$
Frequent	Prestressing	0
Characteristic	No prestressing	$0.75 * f_{ctk:0.05}$ or $\sigma_c < 2.25$
Characteristic	Prestressing	$0.5 * f_{ctk:0.05}$ or $\sigma_c < 1.5$
Construction phase	Everywhere	$\sigma_c < f_{ctm}$ or $\sigma_c < 3.0$

Table 9.2: Maximum allowable tensile stresses according to OVS00030-6

The OVS sets different limits for the different load combinations in the serviceability limit state. In load combinations with a higher loading, higher stresses are allowed. The background of the requirements with regard to the stresses aren't exactly clear. It is assumed that the reasons are still valid for the application of UHPFRC.

The stress limits are given as a percentage of the concrete tensile strength, in combination with an upper limit. To soften the requirements these upper limits have been omitted. Due to the high tensile strength of UHPFRC this will lead to higher maximum tensile stresses.

For three situations however the maximum tensile stress is not given as a percentage of the strength, but set to  $0 N/mm^2$ . The frequent combination at the side of the prestressing is one of these situations. As section 9.1.1 has shown, the frequent combination is the governing combination in design. Leaving this stress limit at zero will do no right to the material properties and keep the same restriction on the design. The difference in the allowed stress between the characteristic and frequent load combination, at the side of no prestressing, is 25% of the tensile strength. At the prestressing side this is 50%. This is reduced to 25% as well. Which gives a tensile stress limit of 25% of the tensile strength. The stress limit of  $25% \cdot f_{ctk,0.05}$  is also applied in the quasi-permanent combination.

Load combination	Location	maximum tensile stress [ $N/mm^2$ ]
Quasi-permanent	Everywhere	$0.25 * f_{ctk:0.05} = 2.50$
Frequent	No prestressing	$0.5 * f_{ctk:0.05} = 5.00$
Frequent	Prestressing	$0.25 * f_{ctk:0.05} = 2.50$
Characteristic	No prestressing	$0.75 * f_{ctk:0.05} = 7.50$
Characteristic	Prestressing	$0.5 * f_{ctk:0.05} = 5.00$
Construction phase	Everywhere	$\sigma_c < f_{ctm} = 6.20$

Table 9.3: New applied maximum tensile stresses.

### 9.2.1 Governing design aspects

Figure 9.17 shows the resulting unity checks for UHPFRC structures designed according to the OVS-requirements and the self formulated stress requirements. To gain better insight in the governing design aspects the unity checks have again been normalized in figure 9.18.

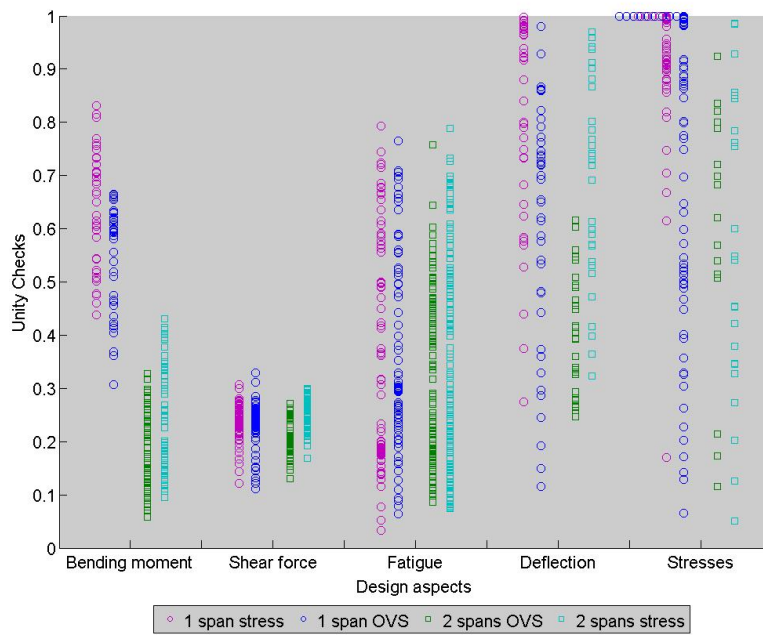


Figure 9.17: Spread of unity checks.

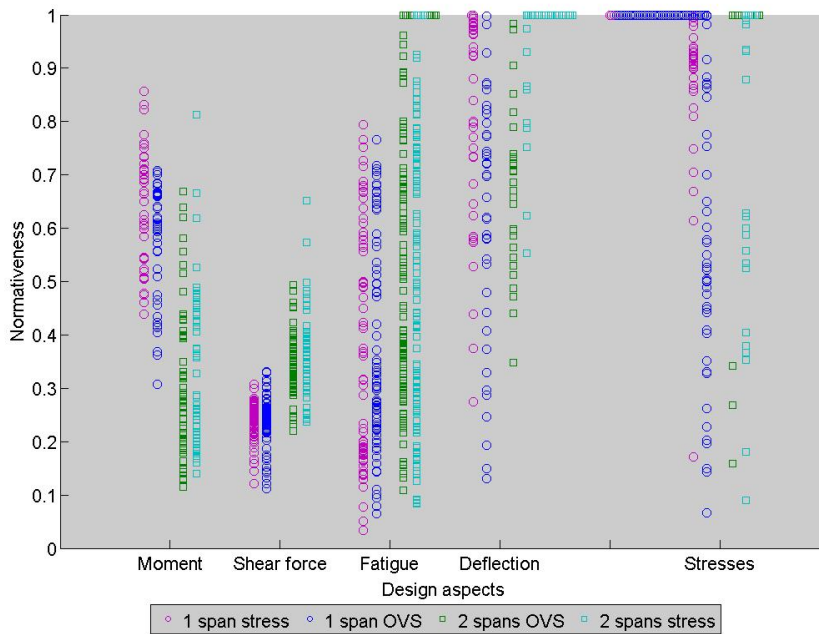


Figure 9.18: Normalized spread of unity checks.

### **Bending moment**

The bending moment design aspect shows the same behavior as the conventional concrete model. Again it is governing in starting the iterations, but the unity checks are by no means normative. Again this is due to the fact that the concrete compressive zone is larger than the allowed compressive zone height. This effect is however less pronounced in UHPFRC where only about three iterations are required and it only occurs for span lengths shorter than 37 meters.

The unity checks are somewhat higher in the stress limit model compared to the OVS-model. The reduced height causes a decrease of the internal lever arm and thus the moment capacity.

### **Shear force**

The shear force shows a slight, but insignificant increase in unity checks. Although the cross section area of a wall may be higher due to an increased wall width (see section 9.2.2), the reduced effective height  $d$  is taken into account for calculating the shear resistance. As the wall height is generally decreased or the same, so is the shear resistance.

### **Fatigue**

On first sight the fatigue results show little change. Also when the results are separated for the three cross sections like in section 9.1.1 the results are very similar. The model results do however show that the fatigue loading, at the top of the mid support cross section, is taken by the reinforcement steel. This happens for the spans of 48 meters and longer.

### **Deflection**

In both the single and double span structure deflection becomes more important as a design aspect. Where in the single span structure deflection was never normative it does now a few times, but also in the range just between 0.9 and 1.0 a lot of normalized unity checks are present. This aspect is even more accentuated by figure 9.19. This shows that although the highest unity check is most often one with regard to the deflection, the geometry is mostly determined by iterations concerning the stress limits. It also shows clearly that the span range for which the deflection becomes normative is larger than when the OVS-limits are applied.

In the double span structure there is a clear shift of the most important aspect for design. Where the OVS limits cause the stresses and fatigue to be the most important design aspect, loosening these requirements will cause the deflection to become more important. Figure 9.20 does not show any iterations based on deflection though. From this it can be concluded that as soon as the stresses are satisfied, the deflection is also satisfied, but only just. From the 31 structures in 26 cases the unity check for deflection was higher than the maximum unity check for the stress verification.

### **Stresses**

The design aspect with regard to the stresses show that the stresses remain the most important design aspect for statically determined structures. For the statically undetermined structure this effect is reduced as the deflection plays a larger role in designing. Figure 9.20 and 9.19 show that the stress verifications are easier satisfied. This is the direct effect of higher stress limits. The verification are actually already satisfied at geometries which are not able to satisfy the verifications on bending moment or deflection.

Separating the unity checks for the various load combinations in figure 9.21 shows that there is a change in which load combination is governing. Where the majority of the governing unity checks were situated in the characteristic load combination for the OVS-limits, loosening these limits

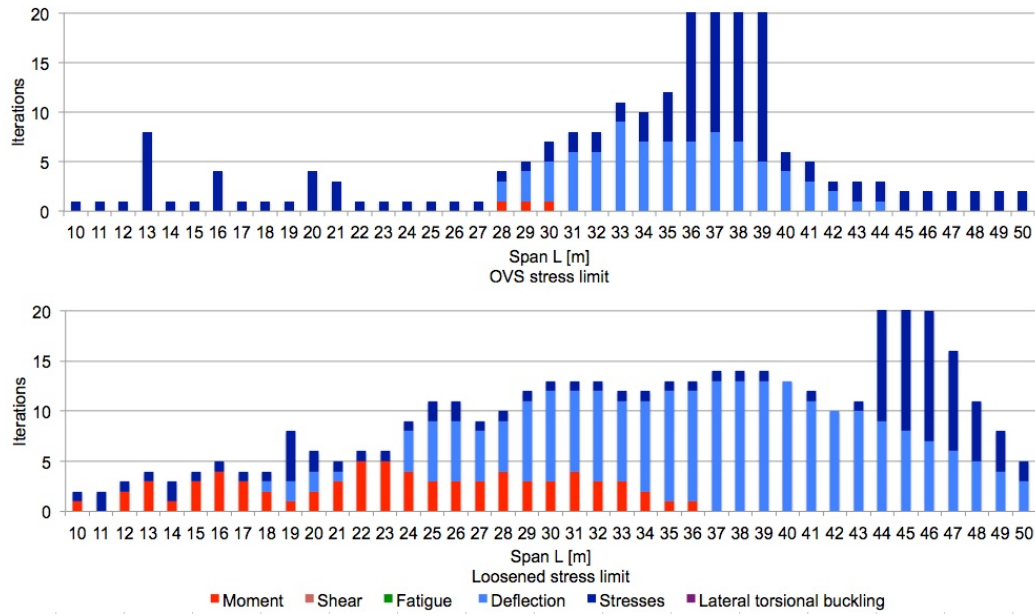


Figure 9.19: Design iterations to span length for single span structure.

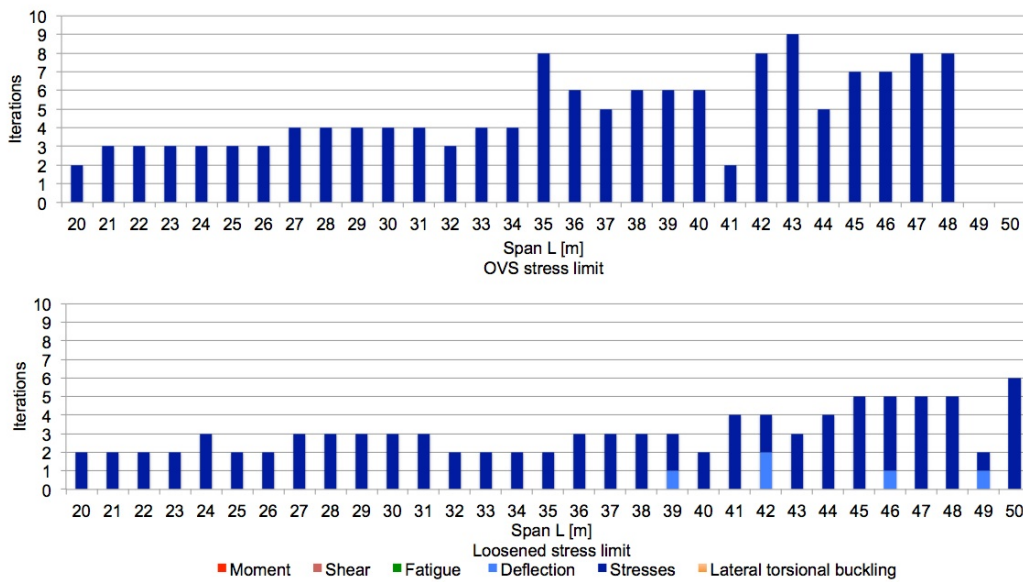


Figure 9.20: Design iterations to span length for double span structure.

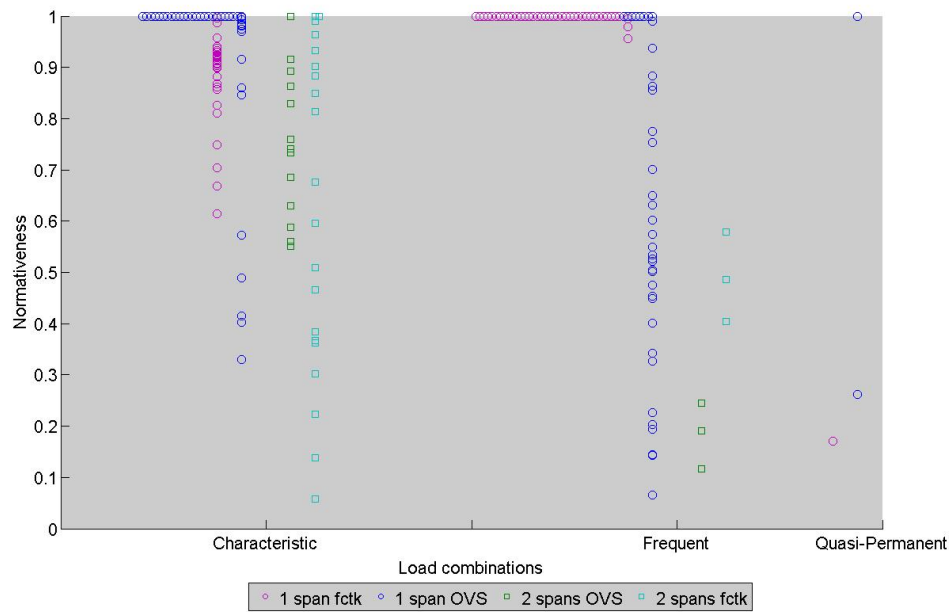


Figure 9.21: Normalized unity checks for stress verifications.

causes that almost all governing unity checks are situated in the frequent load combination. Again this can be explained by the difference in the allowed and occurring stresses in the different load combinations. From the characteristic to the frequent load combination the allowed tensile stress is now reduced with  $2.50/5.00 = 50\%$ . This percent wise even more than for the OVS-limits. The working bending moment is reduced even less with only 23%.

### Lateral torsional buckling

In the previous section on lateral torsional buckling there were two aspects which influenced the unity checks; the cross sectional dimensions and the material properties. Figure 9.22 shows the unity checks on lateral torsional buckling for both the OVS stress limitations and the UHPFRC stress limitations. The material properties remain the same and a reduction in cross sectional area can be achieved with the UHPFRC stress limits. This makes it possible to look at the influence of a smaller cross section on the lateral torsional buckling verification.

Figure 9.22 shows in general an increase of the unity checks for the smaller cross sections (the results of the UHPFRC stress limits). The amount of increase is however very fluctuating and may for some structures even be none existing up to as much as 0.26.

### 9.2.2 Geometrie

The section above shows that reducing the limitations to the stresses in the serviceability limit state makes that the especially the deflection becomes more important. This section will go into the results in terms of geometry of the structure.

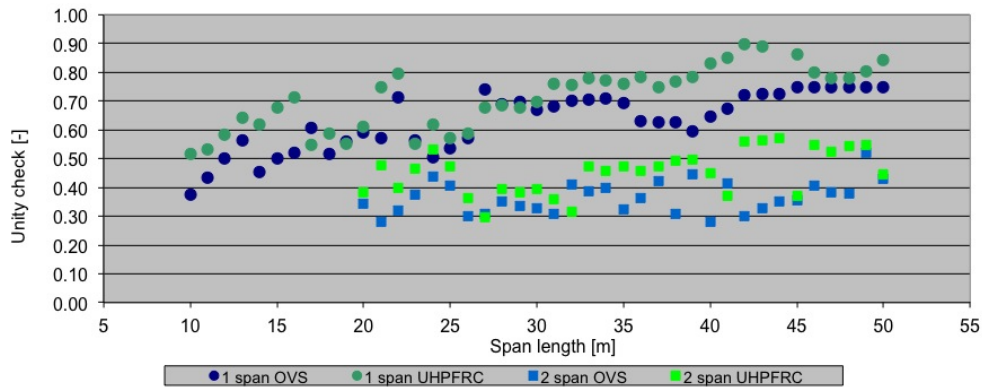


Figure 9.22: Verifications on lateral torsional buckling to span length.

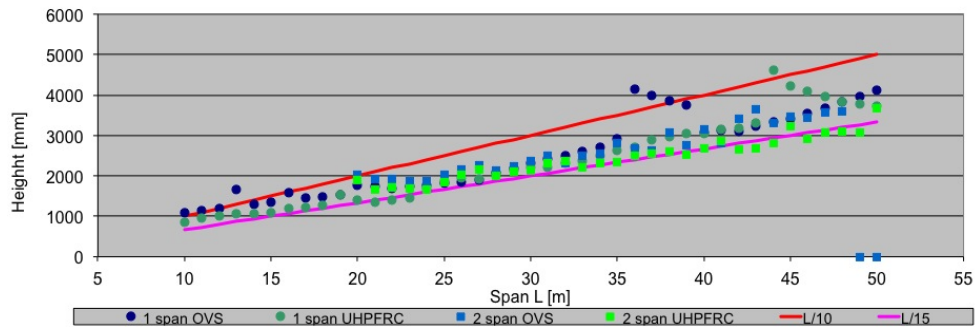


Figure 9.23: Structure height to span length.

**Height**

Figure 9.23 shows the height of the structures over the length. The model which shows the most significant reduction of height is the statically undetermined structure. Here the reduction is between 100 mm and 800 mm. In the statically determined structure the structure height remains almost equal to the OVS-limit model. The average reduction is height is 140 mm. It must be said that the deviation of this average is rather larger for both models. Therefore it is not quite possible to give an unambiguous statement about the height reduction. What can be noted is that for the single span structure the height reduction is more located in the shorter spans, while in the double span structure the most reduction is present for spans longer than 35 meters.

**Concrete cross sectional area**

In the single span structure the wall width shows a split in two ranges. From span length 10 meters up to 30 meters the wall width rises quick for the reduced stress limit model compared to the OVS-results. This is due to the iterations started by the bending moment design verification. This design aspect causes both the height and the wall width to increase. As soon as the bending moment design

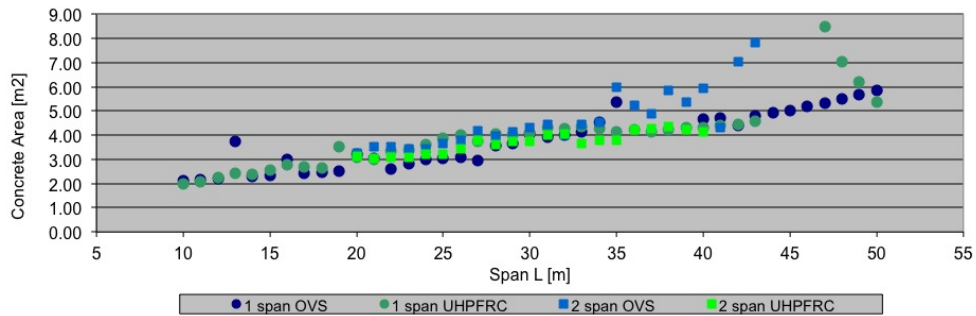


Figure 9.24: Concrete area to span length.

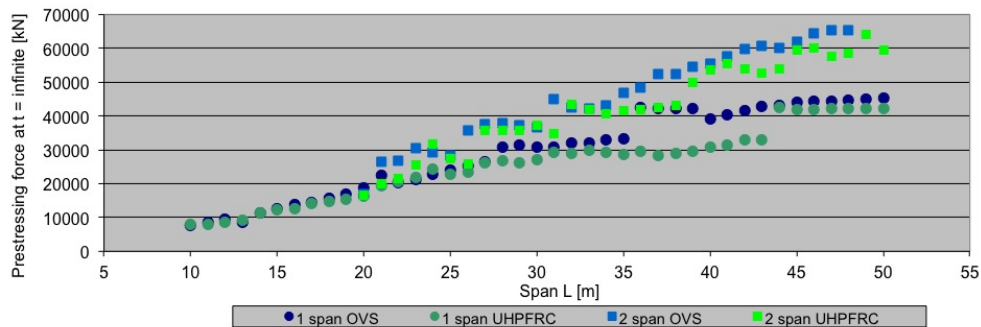


Figure 9.25: Prestressing force to span length.

aspect disappears from figure 9.19 the wall width for both models are almost the same.

The double span structure shows a reduction in wall width for the reduced stress limits for spans longer than 35 meters. This can be explained as for this region the OVS-limit model applies a larger prestressing force with more ducts. To fit these ducts the wall width is increased.

The changes in structural height and wall width taken into account, the total area of the structure shows little reduction compared to the OVS-limit model. The reduced area by the loss of height is compensated for by the increased wall width. Due to the increased wall width the average difference between the single span models is even shows a small increase, but here also large deviations can be found. The double span structure shows a reduction in concrete area in the longer span region, but here a large deviation seems to occur in the OVS-limit model.

In general it can be said that not much concrete area is reduced by increasing the tensile stress limits. However, as the height does decrease and the wall width increases due to the bending moment iterations, which is purely a modeling choice, it would be interesting to see how the design changes when the increased wall width due to bending moment iterations is omitted.

### Prestressing

For the double span structure the prestressing force does not show substantial differences in the applied prestressing force. The average change in prestressing force is a reduction of 4000 kN.

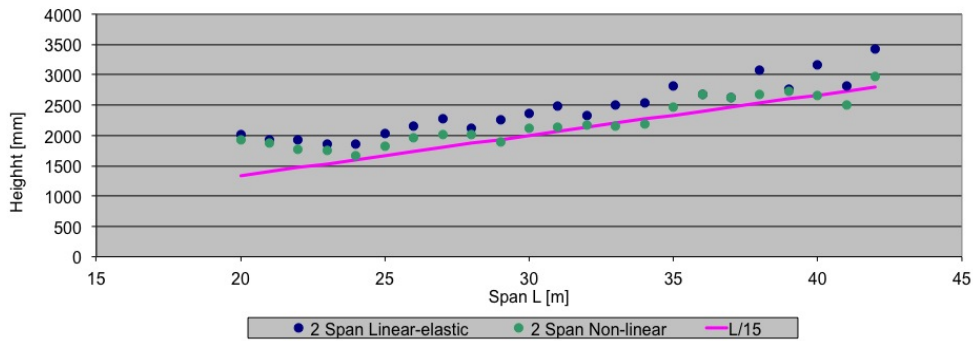


Figure 9.26: Structure height to span length.

Assuming a working prestress of  $\sigma_{pw} = 1000 \text{ N/mm}^2$  this is less than the force in two 19 strands cables ( $2 \cdot 140 \text{ mm}^2 \cdot 19 \cdot \sigma_{pw} \cdot 10^{-3} = 5320 \text{ kN}$ ).

Except of the span range between 36 and 43 meters the prestressing force in the single span structures are almost the same. This area shows resemblance to figure 9.19. In this area the models require many iterations and produce unrealistic results.

### 9.3 Non-linear results

Due to the limitations of the non-linear model (section 8.9.3) large deviations are expected. Therefore the results of the non-linear model can not be regarded as absolute results. Consequently the results will not be presented as in previous sections, but rather a qualitative description will be given.

#### 9.3.1 Geometry

The only cross sectional dimension which is variable in the non-linear model is the height of the walls. Figure 9.26 shows the difference in the wall height between the linear-elastic and non-linear results. This figure shows that a reduction of the wall height is possible after redistribution of the bending moments. The reduction in height varies between 100 mm and 400 mm. The reduction in height is possible because on the capacity side there is a certain measure of overcapacity in the verifications. This is due to the fact that the cross sections are not fully optimized. In the subsequent iterations the capacity of the cross sections is reduced faster than the load effect due to moment redistribution. This causes that at a certain iteration one or more verifications can no longer be satisfied.

#### 9.3.2 Moment redistribution

The gain which can be achieved by applying a non-linear calculation can be expressed in the redistribution of the bending moment. Therefore it is interesting to evaluate how much moment redistribution UHPFRC allows. The measure of moment redistribution is expressed with the symbol  $\delta$ . This stands for the ratio between the linear-elastic and non-linear bending moment. For the statically undetermined structure with two simply supported spans  $\delta$  is calculated based on the support bending moment (equation 9.6). A value of  $\delta = 1.0$  indicates the linear-elastic bending moment.

$$\delta = \frac{M_{\text{support,NL}}}{M_{\text{support,LE}}} \quad (9.6)$$

The maximum bending moment redistribution by the Eurocode for linear-elastic calculations with restricted redistribution is given for concretes with  $f_{ck} > 50 \text{ MPa}$  as:

$$\delta \geq k_3 + k_4 x_u / d \quad (9.7)$$

in which:

$$k_3 = \frac{7f}{\varepsilon_{cu3} \cdot 10^6 + 7f}$$

$$k_4 = 1.0$$

$$f = \frac{(f_{pd} - \sigma_{pm,\infty})A_p + f_{yd}A_s}{A_p + A_s}$$

$x_u$  height of concrete compressive zone after redistribution

$d$  effective height of the cross section

Figure 9.27 shows how this maximum moment redistribution relates to the found redistributions in the non-linear model results. For each span length the maximum redistribution according to the Eurocode is depicted as a square. The circles are the found moment redistributions in the non-linear model results. The color of the circles indicate which design aspect is gives the highest unity check. The maximum moment redistribution according to the Eurocode remains fairly constant between 0.65 and 0.70. The achieved moment redistribution in the results show a large scatter for the various span lengths. The non-linear structures where fatigue and deflection were leading show per design aspect a  $\delta$  of the same order of size. For the stresses however even within this design aspect there is a large scatter. To explain this the span lengths of twenty-two and thirty-seven meters, with respectively a large and small redistribution are investigated.

### Span L=22 m

The cross-sectional height resulting from the linear-elastic calculation is  $h = 1920 \text{ mm}$ . Each iteration the height is reduced with 50 mm until after the fourth iteration at  $h = 1720 \text{ mm}$  the verification with regard to the stresses at the top side of the structure due to the frequent load combination can no longer be met. The unity check for this verification rises in four iterations from  $-0.34$  to  $1.34$ . Figure 9.28 shows the stress distribution in the top of the structure due to the governing frequent load combination for the different iterations. In the linear-elastic calculations the stress is  $\sigma = 0.16 \text{ N/mm}^2$ . With a maximum allowed tensile stress of  $\sigma_{max} = 1.50 \text{ N/mm}^2$  this leads to the negative unity check of:

$$u.c. = \sigma - \sigma_{max} + 1 = 0.16 - 1.50 + 1.00 = -0.34 \text{ N/mm}^2 \quad (9.8)$$

Because of the definition of the unity check on stresses (equation 9.9) the values of the unity checks may be misleading. They do not represent a percentage of the used capacity, but they represent an actual amount of  $\text{N/mm}^2$  that the effective stress is removed from the maximum stress. This residual capacity can be expressed as equation 9.10. When this residual capacity is larger than one  $\text{N/mm}^2$  the unity check give a negative value.

$$u.c. = \sigma_{Ed} - \sigma_{max} + 1 \quad (9.9)$$

$$\sigma_{residual} = 1 - u.c. \quad (9.10)$$

The verification for the stress has been defined according to function 9.9 as maximum tensile stresses of  $0 \text{ N/mm}^2$  occur, which would, with the regular verification, lead to a division through zero.

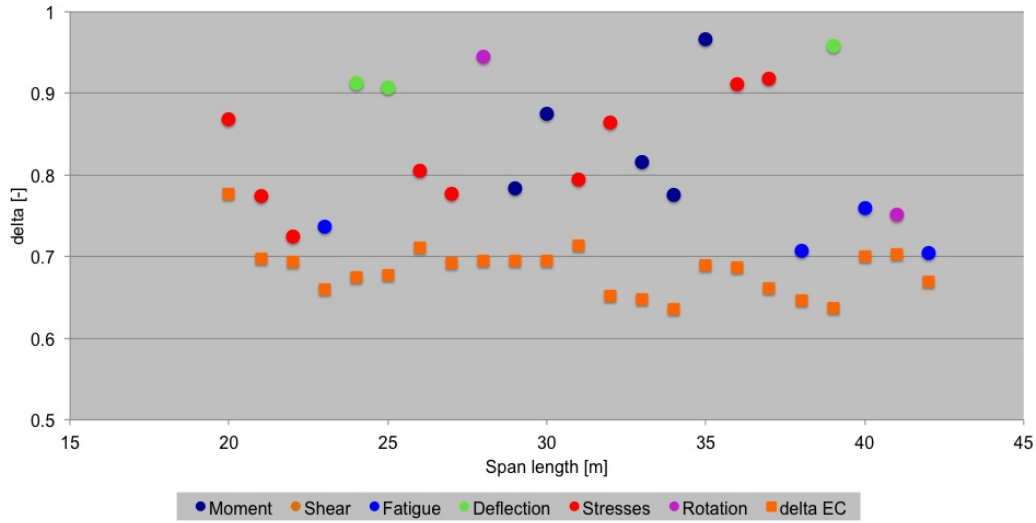


Figure 9.27: Ratio of moment redistribution  $\delta$  to span length.

Design aspect	linear elastic h=1920 mm	iteration 1 1870 mm	iteration 2 1820 mm	iteration 3 1770 mm	iteration 4 1720 mm
u.c. fatigue field bottom	0.34	0.34	0.35	0.36	0.37
u.c. fatigue field top	0.11	0.11	0.11	0.11	0.12
u.c. fatigue support bottom	0.16	0.16	0.17	0.17	0.18
u.c. fatigue support top	0.49	0.51	0.53	0.55	0.57
u.c. lateral torsional buckling	0.32	0.33	0.33	0.33	0.34
u.c. moment field	0.21	0.21	0.21	0.22	0.22
u.c. moment support	0.07	0.07	0.24	0.29	0.35
u.c. shear compressive strut	0.19	0.19	0.20	0.20	0.21
u.c. shear	0.21	0.21	0.21	0.22	0.22
u.c. characteristic bottom	-3.84	-3.56	-3.45	-3.32	-3.17
u.c. characteristic top	-0.58	-0.82	-0.45	-0.04	0.41
u.c. frequent bottom	-2.48	-2.37	-1.98	-1.58	-1.36
u.c. frequent top	-0.34	0.07	0.45	0.87	1.34
u.c. quasi-perm. Bottom	-1.17	-1.06	-0.46	-0.27	-0.05
u.c. quasi-perm. Top	-1.07	-0.94	-0.71	-0.44	-0.14
u.c. deflection	0.33	0.33	0.35	0.38	0.40
u.c. rotation field	-	0.53	0.56	0.54	0.56
u.c. rotation support	-	0.02	0.20	0.20	0.21

Table 9.4: Value of the verifications for the non-linear iterations. L=22 m.

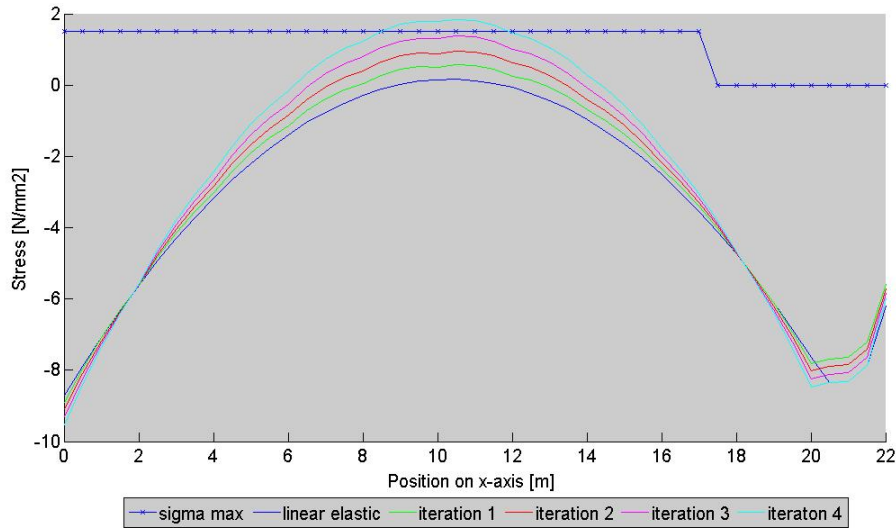


Figure 9.28: Stresses in top fibres due to governing frequent load combination.

### Span L=37 m

In the structure with span length 37 meters the stresses in the frequent combination are also governing. Here, however, no redistribution is possible. Table 9.5 presents the unity checks for the linear-elastic results and after the first (and only) non-linear iteration. This table shows that after the linear-elastic calculation the stresses at the top side in the characteristic combination are governing. In the non-linear calculation this has changed to the frequent combination. This change can be explained by figure 9.29 which displays the maximum stresses at the top in the characteristic and frequent load combination and the corresponding stress distributions in the linear-elastic and non-linear calculation. This shows that the critical position for the stresses is the top fibre above the mid-support. The graph shows that after moment redistribution the stress in the characteristic load combination decreases, while in the frequent combination the stress increases. This increase is that much that after redistribution the stress goes from  $-1.67 \text{ N/mm}^2$  to  $0.22 \text{ N/mm}^2$ .

The reason why the stress increases in the frequent combination and decreases in the characteristic is due to the redistributed bending moment as the cross sectional properties and prestressing are the same. Investigating the bending moments shows that the redistributed bending moment in the characteristic load combination results in a smaller bending moment at the support. Redistribution in the frequent combination leads to a larger bending moment at the support. This can also be recognized in figure 9.29. In fact, the redistributed bending moments are very close together, giving a similar stress in the top fibre. For the frequent combination the maximum stress is lower however and thus leads to a unsatisfied design verification.

### General remark

This investigation of the two separate span lengths shows two situations where the stresses in the serviceability state were governing. In these two situations it was shown that the number of possible iterations (and thus the magnitude of redistribution  $\delta$ ) was dependent on the remaining capacity of the verifications in the linear-elastic calculation.

Design aspect	linear elastic	iteration 1
	h=2620 mm	h=2570 mm
u.c. fatigue field bottom	0.25	0.26
u.c. fatigue field top	0.55	0.56
u.c. fatigue support bottom	0.51	0.52
u.c. fatigue support top	0.13	0.14
u.c. lateral torsional buckling	0.42	0.43
u.c. moment field	0.29	0.30
u.c. moment support	0.16	0.16
u.c. shear compressive strut	0.20	0.19
u.c. shear	0.25	0.24
u.c. characteristic bottom	-6.31	-5.86
u.c. characteristic top	0.84	-0.06
u.c. frequent bottom	-6.13	-4.94
u.c. frequent top	-0.67	1.23
u.c. quasi-perm. Bottom	-6.83	-6.47
u.c. quasi-perm. Top	-7.49	-7.50
u.c. deflection	0.62	0.72
u.c. rotation field	0.00	0.53
u.c. rotation support	0.00	0.01

Table 9.5: Value of the verifications for the non-linear iterations. L=37 m.

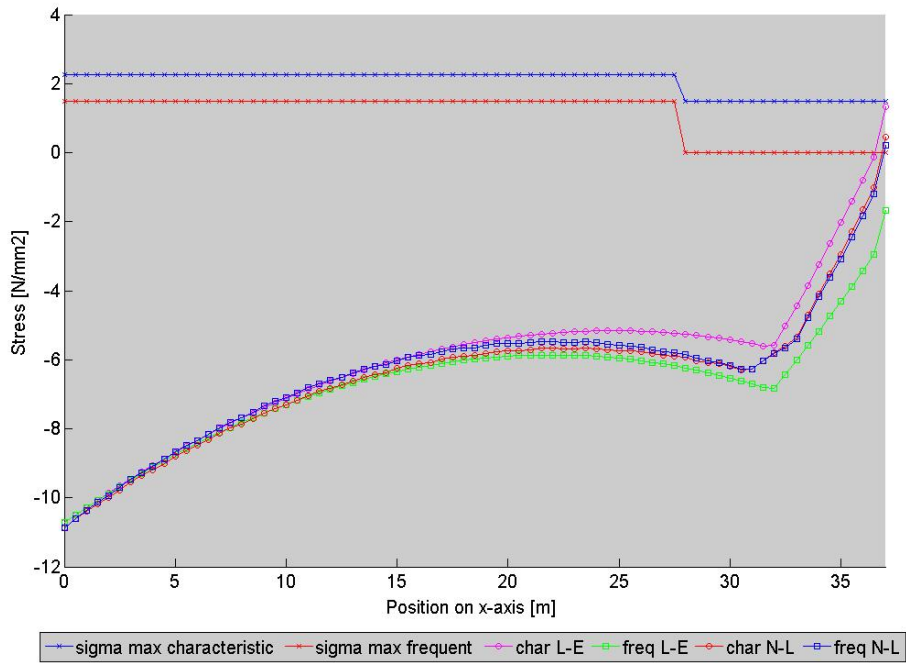


Figure 9.29: Stresses in top fibres due to governing characteristic and frequent load combination.

The investigation has also shown that the moment redistribution does not always redistribute the bending moment in the same direction. This is inherent to the way the model enforces the displacement to meet the boundary conditions. In certain situations the bending moment is redistributed upward and in other times downward, dependent on whether the initial displacement is situated above or below zero displacement at the mid support.

### 9.3.3 Rotation capacity

UHPFRC is a tough material with (for concrete) a high ductility. This material property makes that it can allow large rotations. Although the rotation capacity was only twice the governing design aspect in the twenty-three evaluated structures it is an important aspect of non-linear calculation. The model results show that the allowed maximum rotation is much dependent on the applied verification method (see also section 7.3). The applied method in the non-linear model is originating from the CUR 108 publication. This method defines the ultimate rotation by equation 9.11. As in UHPFRC structures the height of the compressive zone in the ultimate state ( $x_u$ ) generally becomes smaller, the maximum rotation becomes larger compared to conventional concrete.

$$\Phi_u = \frac{\epsilon_{cu3}}{x_u} \cdot d \quad (9.11)$$

The ultimate rotation calculated by the method of the Eurocode is dependent on the relative depth of the compressive zone  $\xi = \frac{x_u}{d}$ . As the compressive zone becomes smaller in UHPFRC, the relative depth also decreases (even though the structural height in general decreases as well). However, the relation between the relative depth and the ultimate rotation is bi-linear. The relation is given in figure 9.30. It can thus not simply be said that, as the relative depth in- or decreases, the ultimate rotation behaves in a certain direction.

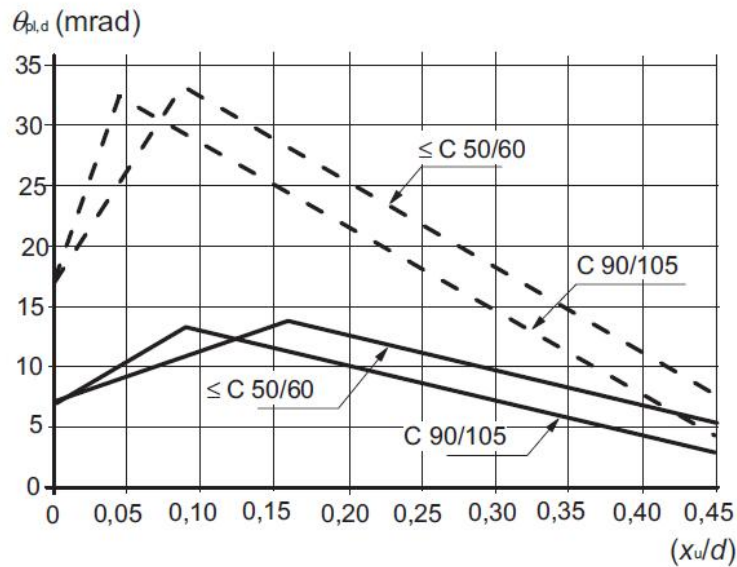


Figure 9.30: Maximum allowed rotation according to NEN-EN 1992-1-1.

Figure 9.31 shows the maximum allowed rotation above the mid support for both verification methods and for the results in conventional concrete and UHPFRC. The values have been calculated

based on the linear-elastic results. This graph clearly shows how the CUR108 recommendations allow a larger rotation. This especially influences the UHPFRC structures which have a relative small relative compressive depth.

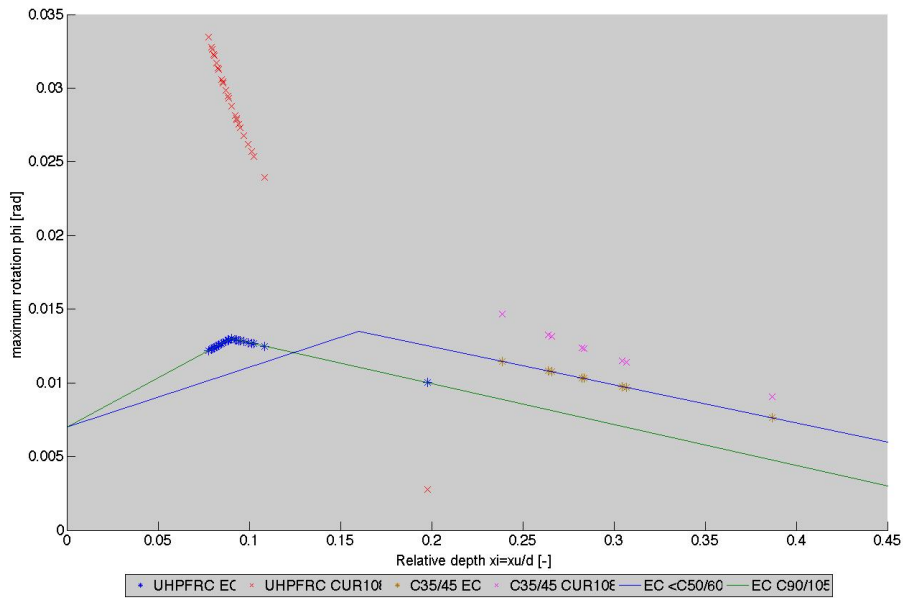


Figure 9.31: Maximum allowed rotation for C35/45 and UHPFRC according to CUR108 and Eurocode.

The two different verification methods compared here give very divergent results. In this it must be noted that both verification methods are not tailored to the material properties. Although the rotation capacity has not shown to be normative in the non-linear calculations more research to the rotation capacity of UHPFRC structures should be performed to be able to apply boundaries which suit the material behavior of UHPFRC.

## Chapter 10

---

# Conclusions

### 10.1 Applying UHPFRC

Ultra High Performance Fibre Reinforced Concrete is not a concrete type which can be applied like a conventional concrete with a different stress-strain diagram. Due to its characteristic properties it requires a different approach in design with different verifications. As there is currently no legislative basis for design available (expected end 2014 by *fib* task group) it is important to clarify which design method is being used.

In terms of durability UHPFRC performs very well. Next to a very low impermeability, which makes the material suitable to protect reinforcement- and prestressing steel in aggressive environments, it also contains good abrasion and freeze-thaw resistance properties. These properties make it that the design life-time of UHPFRC could be stretched beyond those of conventional structures. Although UHPFRC is per cubic meter more expensive, the design life time makes that the life cycle costs could well be lower than for a conventional structure.

When designing a trough bridge in conventional concrete the OVS-requirements with regard to the stresses in the serviceability limit state are governing. Meaning that the tendon profile, the geometry and the minimum and maximum prestressing force may not be in conflict with each other. For designing in UHPFRC this aspect remains the same. When this is satisfied, most other verifications will also be satisfied. However, due to the application UHPFRC the concrete cross sectional area can be reduced. This results in a smaller moment of inertia and therefore in less resistance against deflection. Where the deflection hardly plays a role in conventional concrete trough bridges, it does become an important design aspect in UHPFRC. Especially for double span structures, where the height of the structure can significantly be reduced, this plays an important role.

UHPFRC contains high fatigue strengths. Especially in case of compression the fatigue strength is sufficient to withstand the stresses due to fatigue loading. In case of tension the fatigue verifications demand more attention. Here the capacity is approached. It must however be noted that it was possible to satisfy all the fatigue tensile verifications in the longitudinal direction without the application of reinforcement steel.

In calculating the shear capacity UHPFRC knows a third component next to the concrete and reinforcement capacities; the fibres. In the calculation of the shear capacity the fibres are given a relatively low tensile strength over 90% of the effective concrete area. The fibre capacity increases the shear capacity of the cross section to such an extent that shear force is the least important design aspect. Due to the high compressive strength the compressive strut gains a high capacity as well.

In general UHPFRC does not lead to an increased bending moment capacity. The horizontal compressive force can be achieved in a smaller compression zone, which increases the internal lever arm, but this is of little influence. The steel fibres also cause only a small contribution compared to the forces by the activated reinforcement- and prestressing steel. In trough bridges this is no

problem as the bending moment capacity rarely turns out to be normative. However, UHPFRC can be used to create a large bending moment capacity. Due to its high compressive strength the maximum percentage of reinforcement steel can be rather high. In combination with the maximum reinforcement percentage UHPFRC can accommodate large bending moments. This property might be applied in structures where the bending moment is more important as a design aspect, like, for instance, plate bridges.

For both the single and the double span structure the concrete cross sectional area shows a significant reduction of circa  $4 m^2$  and  $2 m^2$  respectively. This reduction is that large that even though UHPFRC is more dense the structures are generally lighter than conventional concrete structures. In railway bridges this may provide possibilities as the structures are often prefabricated and later in a short period of time, put in place. A lighter structure makes this easier, but also possible for longer spans.

Much of the reduced area is due to the decreased structure height. Although the reduced concrete area is favorable for the costs, in trough bridges the height of the wall is usually not important. More useful is the possibility to reduce the thickness of the trough floor as this reduces the effective construction depth. In combination with heavy reinforcement, like described above, the thickness of the trough floor can at least be halved.

The application of  $\varnothing 25 - 125 mm$  reinforcement in the 300 mm thick floor is quite dense. This can influence the fibre directions and concrete quality. Even more dense reinforcement is applied in compact reinforcement layers which can be applied as reinforcement of steel orthotropic plate bridges. The execution methods applied for these overlays could be a source of inspiration for the execution of the UHPFRC trough floor.

## 10.2 Reducing the stress limitations

The limitations the OVS sets to the allowable stresses in the serviceability limit state are unfavorable for UHPFRC. Due to its high tensile strength the upper limits allow at most 30% of its capacity. At the same time these stress limits are the governing design aspect in designing trough bridges (both in UHPFRC as in conventional concrete). Loosening the stress limitations by allowing a certain percentage of the tensile strength does more right to the material properties.

After loosening the stress limitations the design aspect with regard to these stresses is still the one which results with the highest unity checks. Though the structure geometry is no longer determined by the required moment of inertia to reduce the stresses, but by the moment of inertia required to satisfy the deflection demands. The deflection becomes especially important for spans with lengths from 30 meters and longer for single spans and 35 meters and longer.

The effective gain in reduced cross section area is very little for both single and double span structures. In single span structures the most, with on average  $0.10 m^2$ . On the area of prestressing there is no unambiguous trend to be noted. In general it can be said that the amount of required prestressing is in the same order as when the OVS stress limits apply. Recapitulating there seem to be little advantages for trough bridges to loosening the stress limitations.

The problem with the stress verification is that after application of a certain prestressing, stresses arise which exceed the limit. This is because it is the actual limit which is applied in determining the prestressing force. The higher allowed stresses for UHPFRC do not lead to solving the design issue with regard to the stress limits. The higher allowed stress only give different boundary conditions. The only way that the verification on stresses is easier satisfied, is when the applied boundary conditions for determining the prestressing force are taken lower than the allowed limit. On this way the minimum and maximum prestressing force can be determined at one or two cross sections. Incidental higher stresses which occur at different cross sections will then more likely be within the

limits. However, this method does no right to the material and is only more conservative. It may as well be applied in conventional concrete as is UHPFRC.

### 10.3 Non-linear calculations

The non-linear results show that a moment redistribution with  $\delta$  as low as 0.7 is possible. Consequently this makes a reduction in the cross sectional area possible. The results, however, show a large scatter. The amount of moment redistribution, and reduction in cross sectional area, is very much dependent on how much residual capacity is present in the linear-elastic verifications.

The non-linear calculation gives rise to the verification of the rotational capacity. Here the allowable rotation is very much dependent on the applied verification method. The CUR 108 method seems to do more right to the material properties as it allows larger rotations.

### 10.4 General conclusion

UHPFRC shows as a material many favorable properties compared to conventional concrete. A higher compressive and tensile strength, increased fatigue resistance and excellent durability performance. A drawback of the material is however the execution method. Due to the composition the mixture is very thick and more difficult to pour. Besides this it may (depending on the mixture) require heat treatment. When executing a structure in UHPFRC specific attention needs to be payed to the quality control.

Trough bridges are structures which generally are applied when the structural height is of little importance. Applying UHPFRC makes it possible to reduce the construction height. The approached slenderness in UHPFRC is however not of an order which a well designed and optimized conventional concrete structure can't approach. The actual effective construction depth is determined by the trough floor. In UHPFRC the thickness of the trough floor can be reduced significantly. For this reason there might be possibilities in applying an UHPFRC trough floor in combination with conventional concrete walls.

Due to the possible application of a high reinforcement percentage the moment capacity can be significantly increased. UHPFRC is therefore better used in structures where the bending moment capacity tends to become normative, like plate bridges.

The stress limitations in the OVS do no right to the material properties of UHPFRC. However, configuring these stress limits to the properties of UHPFRC does not necessarily lead to much gain in terms of concrete area. Other design aspects become governing in dictating the cross section dimensions.



## Chapter 11

---

### Recommendations

Based on the results and conclusions from this research some recommendations can be given as to how further investigate the possibilities of UHPFRC in large infrastructural works.

- UHPFRC is a material which is very suitable to make a fully optimized design. Due to its high compressive and tensile strength, the possibility of omitting additional steel reinforcement and the high cost per volume compared to conventional concrete. The way how the UHPFRC was applied in this research is therefore rather unsophisticated. The shape of the structure was never regarded as a variable. In designing a fully optimized structure the actual shape of the structure and the specific material properties should be taken into account as an integral part of design. There are multiple examples available in the literature which show designs in UHPFRC which make optimized use of the material and the shape of the structure.
- The possibilities of fully optimizing a design with UHPFRC in combination with the shape of the structure make that the used model in this research is no longer applicable. It is recommended that as the shapes of UHPFRC structures become more complicated finite element models are applied. Contrary to the applied model in this research a three dimensional model can give a more accurate representation of the stresses and strains in the material. Especially for fully optimized designs it is important to be able to verify the internal loads and forces at all sections.
- The results have shown that, for a constant material, a smaller cross section is more sensitive to lateral torsional buckling. In this research the walls were not fully optimized and the limitations of lateral torsional buckling are not approached. As UHPFRC is a material which is very suitable for fully optimized designs it is very likely that in the future UHPFRC designs will be made where lateral torsional buckling will become a design issue. The applied verification method on lateral torsional buckling in this research is only an indication of the sensitivity of the structure on this kind of instability. It is not an absolute verdict. As UHPFRC structures are likely to obtain more slender webs it is recommended that research is performed on defining a verification method for lateral torsional buckling in concrete structural elements.
- It was shown in section 8.8 that the way the Matlab model alters the cross section in the various iterations has a large influence on the results of the model. Different choices in the way the model optimizes the construction may lead to more optimized structures. Due to the parametric design further optimization compared to the model results is also possible when one individual structure with its specific situation is considered.
- In tension the fatigue stresses have to be accounted for by either the concrete, or, when this capacity is insufficient, by the reinforcement. When the reinforcement is applied to withstand

the fatigue all stresses are applied to the reinforcement steel. As in reality part of these stresses are taken by the steel fibres it can be expected that the application of steel fibres has a positive effect on the fatigue resistance of the reinforcement steel. The extent of this effect is subject to further research.

- Loosening the stress requirement by omitting the upper limits certainly influences the geometry and design of the structure. The OVS-limits are based on concrete mixtures which are no longer the top of the segment. New technologies have made concrete mixtures possible with new material properties. The OVS stress-limits could therefore be considered as outdated limits which no longer comply to the modern concrete mixtures. It should be investigated if the stress-limits in the OVS can be adjusted to suit the material properties of higher concrete strengths and fibre reinforced concretes.
- The research on non-linear calculated structures show that certainly some gain is possible for UHPFRC structures. More research on the non-linear behavior of UHPFRC structures is recommended to provide better insight in the possibilities. Specific attention must be paid to the rotation capacity of UHPFRC as both verification methods compared in this research give a large deviation and are not tailored to the specific UHPFRC material properties.
- Due to the very specific material properties and mixture it is advisable that, as long as UHPFRC is not widely commercially available, the engineering company works closely together with a concrete supplier in order to make a concrete mixture which satisfies the needs of the specific project and of which all material properties are exactly known.
- The workability of the UHPFRC mixture is significantly lower than for conventional concretes due to the addition of steel fibres and the low water-binder ratio. This has a large effect on the quality of the poured concrete and quality control of the cast concrete should therefore be given raised attention. As the quality of the cast concrete can be better controlled in controlled environments it is recommended to design in precast elements where possible.
- The terms 'optimization', 'most governing design aspect' and 'normativeness' have frequently been used. This research has interpreted the unity checks as a measure for how important a certain design aspect is. Although it is an abstract concept and the daily use of it may for the practical engineer not be exactly clear, it would be interesting to perform further research on this term 'normativeness'. Better understanding of which aspects influence a design could lead to new, goal-oriented, technical solutions, or might make it possible to make designs which make better use of the material.

## References

- de Jong, P., & Schaafsma, D. (1997). Kantelkip. *Cement*(9).
- Dilsiz, G. (2013, July). *Levensduurverlenging van vermoeiingsgevoelige orthotrope stalen brugdekken met engineered cementitious composite(ecc)*.
- Eurocode. (2011a, December). *Nen-en 1990+a1+a1/c2* (Tech. Rep.). NEN-EN.
- Eurocode. (2011b, December). *Nen-en 1991-1-5+c1/nb* (Tech. Rep.). NEN-EN.
- Graybeal, B. (2006). *Material property characterization of uhpc* (No. FHWA-HRT-06-103).
- Kenter, R. (2010, October). *The elevated metro structure in concrete, uhpc and composite*.
- Ketel, H., Willemse, R., van Rijen, P., & Koolen, E. (2011). Rekenmodel vvuhsb. *Cement*(3).
- Kremer, A. (2010, October). *Ontwerpvoorschrift profiel van vrije ruimte* (5th ed.; Tech. Rep.). ProRail.
- Kremer, A. (2012, April). *Ontwerpvoorschrift voor kunstwerken aanvullingen en wijzigingen op nen-en normen* (4th ed.; Tech. Rep.). ProRail.
- Raven, W. (2006, May). *Nieuwe blik op kip en knik - stabiliteit en sterkte van staven*.
- Sagel R., D. v. A. (2003). *Ontwerpen in gewapend beton*. Stichting ENCI Media.
- Tirimanna, D., & Buitelaar, P. (2012). Modulaire uhsb brug beproefd. *Cement*(6).
- Valkenburg, C. (2012, May). *Ontwerpvoorschrift baan en bovenbouw spoor in ballast* (6th ed.; Tech. Rep.). ProRail.



## **Appendix A**

---

# **Productsheet Ductal CS1000**



**CS1000**

structural solutions for bridges, decks, marine docks/walls, troughs, piles and leave-in place forms

An exceptional material choice for innovative structural elements that are extremely durable, cost effective and require very little maintenance.

Ductal® is a revolutionary, ultra-high performance composite material that provides strength, ductility, durability and aesthetics. This unique combination of superior properties facilitates the ability to create innovative designs with new shapes that are thinner, lighter and more graceful.

Reinforced with steel fibers, Ductal® CS1000 is significantly stronger than conventional concrete (with strengths similar to some metals) and performs better in terms of abrasion and chemical resistance, freeze-thaw, carbonation and chloride ion penetration.

Because of its optimized gradation of the raw material components, Ductal® is denser than conventional concrete. This “denseness”, along with nano-meter sized non-connected pores throughout its cementitious matrix, also attributes to its remarkable imperviousness and durability against adverse conditions or aggressive agents.



**PHYSICAL PROPERTIES**

Characteristic Values for Design							
	Test Data				Design Values		
	Mean		Standard Deviation				
	MPa	psi	MPa	psi	MPa	psi	
Compression	180	26,000	12	1,800	160	23,000	
Flexural	35	5,000	4.5	650	--	--	
Direct Tension	$f_{ij}$	10	1,450	1	145	8	1,160
	$\bar{\sigma}$ 1%	12	1,800	2	300	8	1,160
Youngs Modulus	GPa	ksi	GPa	ksi	GPa	ksi	
	60	8,700	2	300	55	8,000	

# CS1000

## DURABILITY

• Chloride Ion diffusion	0.02x10 <sup>-12</sup> m <sup>2</sup> /s
• Carbonation penetration depth	<0.5 mm
• Freeze/thaw (after 300 cycles)	100%
• Salt-scaling	<0.10 g/m <sup>2</sup>
• Abrasion (relative volume loss index)	1.2

## OTHER PROPERTIES

• Density	2.4 – 2.6 S.G.
• Capillary porosity (>10mm)	<1%
• Total porosity	2 – 6%
• Post cure shrinkage	<10 <sup>-5</sup>
• Creep coefficient	0.2-0.5

## COMPONENTS

A) Premix	- silica fume, ground quartz, sand, cement
B) High tensile steel fibers	- 0.2 mm (0.008 in) diameter x 14 mm (0.5 in) long (>2000 MPa/ 290 psi)
C) Admixture	- high range water reducer/ 3rd generation
+ Water and/or ice	

## BATCHING

High shear mixers and temperature controlled environments are recommended to successfully produce Ductal® CS1000.

## THERMAL TREATMENT

Thermal treatment of 90°C (195°F), at 90% relative humidity for 48 hours, is applied after final set produces the required design strength and durability characteristics. For fire rated structures, the Ductal® AF formula is available and provides fire performance similar to normal concrete.

## MOLDING

The fineness of Ductal® raw materials and fluidity of the mix facilitates the ability to replicate the micro-texture of the form surface or special mold textures.

## PLACING

Ductal® should be placed in a controlled precast environment. Placing techniques include: gravitational flow, injection or auguring.

## PRE-STRESSING

The strength of Ductal® allows for solutions to be designed with smaller elements, without the use of passive reinforcement (reinforcing steel), prestressing will further enhance and optimize the designed solution.

**Disclaimer:** The values indicated above depend on the product characteristics, experimentation method, raw materials, formulae, manufacturing procedures and equipment used; all of which may vary. This data sheet provides no guarantee or commitment that the values set forth above will be achieved in any particular application of Ductal®. Ductal® is a registered trademark and may not be used without permission. The ultra-high performance material that is Ductal® and its various components are protected by various patents and may not be used except pursuant to the terms of a license agreement with the patent holder.

### Lafarge Canada Inc.

1200, 10655 Southport Road S.W.  
Calgary, Alberta, Canada T2W 4Y1

Email: ductal@lafarge-na.com • Tel: 403-271-9110

Toll free: 1-866-238-2825 • www.imagineductal.com



Post Consumer



### Add value with Ductal® CS1000

- superior strength
- ductility
- freeze/thaw resistance
- design flexibility
- longer spans
- shallow, thin, lightweight structures
- reductions in foundations
- faster construction
- reduce or eliminate passive reinforcing
- increased usage life
- improved seismic performance
- impact resistance
- abrasion resistance
- dimensional stability
- lower permeability
- low chloride ion diffusion
- reduced maintenance



## Appendix B

### Derrivation of uneven settlement

#### B.1 Double span

##### B.1.1 Case 1

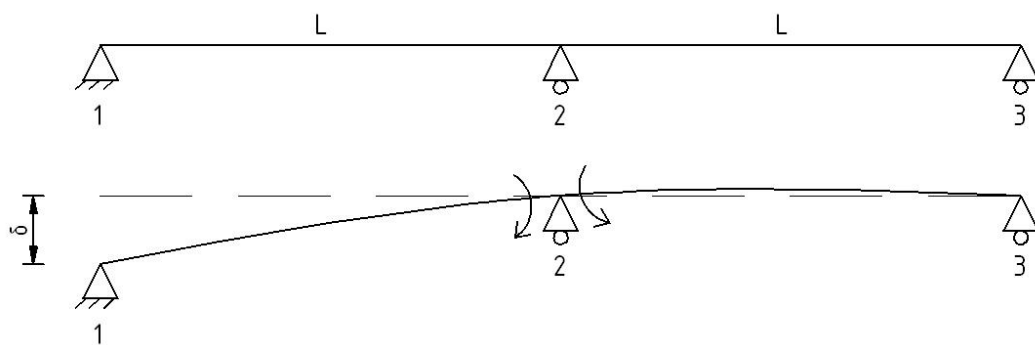


Figure B.1: Uneven settlement at end support

$$\phi_{21} = \frac{\delta}{L} - \frac{M2 \cdot L}{3 \cdot EI} \quad (\text{B.1})$$

$$\phi_{23} = \frac{M2 \cdot L}{3 \cdot EI} \quad (\text{B.2})$$

$$\phi_{21} = \phi_{23} \quad (\text{B.3})$$

$$M2 = \frac{3 \cdot \delta \cdot EI}{2 \cdot L^2} \quad (\text{B.4})$$

$$V_1 = -\frac{M2}{\alpha L} \quad (\text{B.5})$$

$$V_{2L} = -\frac{M2}{\alpha L} \quad (\text{B.6})$$

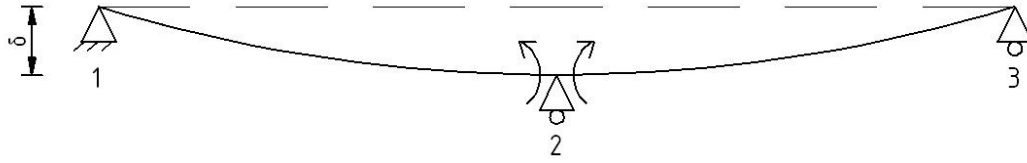


Figure B.2: Uneven settlement at end support

**B.1.2 Case 2**

$$\phi_{21} = -\frac{\delta}{L} + \frac{M2 \cdot L}{3 \cdot EI} \tag{B.7}$$

$$\phi_{23} = \frac{\delta}{L} - \frac{M2 \cdot L}{3 \cdot EI} \tag{B.8}$$

$$\phi_{21} = \phi_{23} \tag{B.9}$$

$$M2 = \frac{3 \cdot \delta \cdot EI}{L^2} \tag{B.10}$$

$$V_1 = \frac{M2}{\alpha L} \tag{B.11}$$

$$V_{2L} = \frac{M2}{\alpha L} \tag{B.12}$$

**B.2 Three spans**

**B.2.1 Case 1**

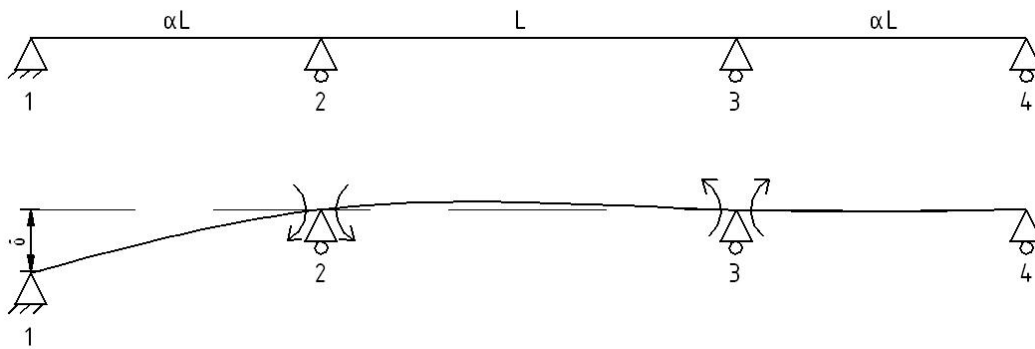


Figure B.3: Uneven settlement at end support

$$\phi_{21} = \frac{\delta}{\alpha L} - \frac{M2 \cdot \alpha L}{3 \cdot EI} \tag{B.13}$$

$$\phi_{23} = \frac{M2 \cdot L}{3 \cdot EI} - \frac{M3 \cdot L}{6 \cdot EI} \tag{B.14}$$

$$\phi_{32} = -\frac{M2 \cdot L}{6 \cdot EI} + \frac{M3 \cdot L}{3 \cdot EI} \quad (B.15)$$

$$\phi_{34} = \frac{M3 \cdot \alpha L}{3 \cdot EI} \quad (B.16)$$

$$\phi_{21} = \phi_{23} \quad (B.17)$$

$$\phi_{32} = \phi_{34} \quad (B.18)$$

$$M_2 = \frac{12(1 + \alpha)\delta EI}{L^2 \alpha(8\alpha + 4\alpha^2 + 3)} \quad (B.19)$$

$$M_3 = \frac{6\delta EI}{L^2 \alpha(8\alpha + 4\alpha^2 + 3)} \quad (B.20)$$

$$V_1 = -\frac{M2}{\alpha L} \quad (B.21)$$

$$V_{2L} = -\frac{M2}{\alpha L} \quad (B.22)$$

$$V_{2R} = \frac{M2}{L} + \frac{M3}{L} \quad (B.23)$$

### B.2.2 Case 2

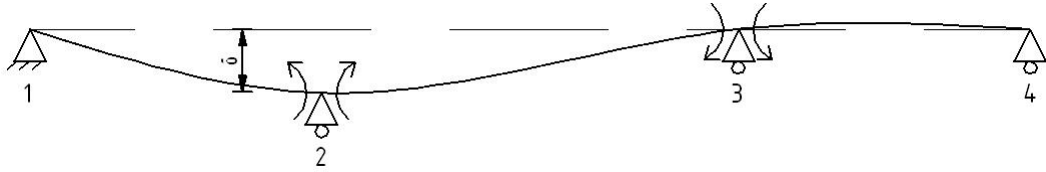


Figure B.4: Uneven settlement at intermediate support

$$\phi_{21} = -\frac{\delta}{\alpha L} + \frac{M2 \cdot \alpha L}{3 \cdot EI} \quad (B.24)$$

$$\phi_{23} = -\frac{M2 \cdot L}{3 \cdot EI} + \frac{M3 \cdot L}{6 \cdot EI} \quad (B.25)$$

$$\phi_{32} = +\frac{M2 \cdot L}{6 \cdot EI} - \frac{M3 \cdot L}{3 \cdot EI} \quad (B.26)$$

$$\phi_{34} = \frac{M3 \cdot \alpha L}{3 \cdot EI} \quad (B.27)$$

$$\phi_{21} = \phi_{23} \quad (B.28)$$

$$\phi_{32} = \phi_{34} \quad (B.29)$$

$$M_2 = \frac{12(1 + \alpha)\delta EI}{L^2 \alpha(8\alpha + 4\alpha^2 + 3)} \quad (B.30)$$

$$M_3 = \frac{6\delta EI}{L^2 \alpha(8\alpha + 4\alpha^2 + 3)} \quad (B.31)$$

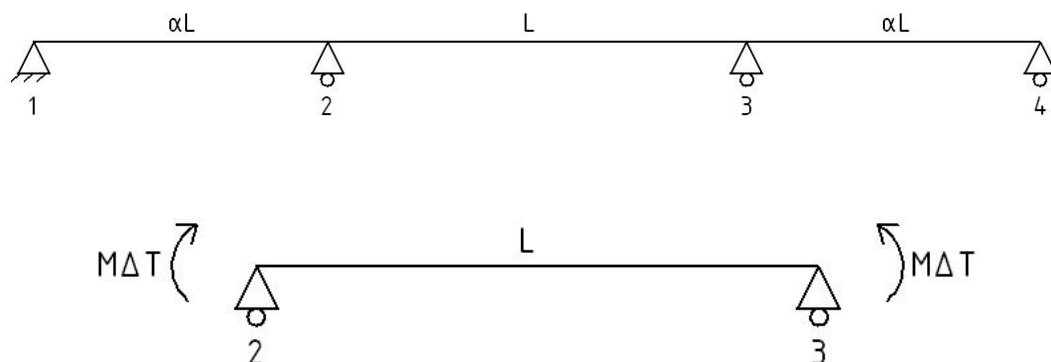
$$V_1 = \frac{M_2}{\alpha L} \tag{B.32}$$

$$V_{2L} = \frac{M_2}{\alpha L} \tag{B.33}$$

$$V_{2R} = -\frac{M_2}{L} - \frac{M_3}{L} \tag{B.34}$$

## Appendix C

### Derivation of temperature load effect



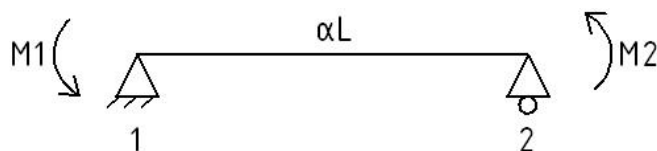
Assuming a constant bending moment over the length of the structure due to heating. This gives:

$$\phi_{23} = -\frac{M(\Delta T) \cdot L}{3 \cdot EI} - \frac{M(\Delta T) \cdot L}{6 \cdot EI} \quad (C.1)$$

$$\frac{\kappa \cdot L}{2} = \left| -\frac{M(\Delta T) \cdot L}{3 \cdot EI} - \frac{M(\Delta T) \cdot L}{6 \cdot EI} \right| \quad (C.2)$$

$$M(\Delta T) = \kappa \cdot EI \quad (C.3)$$

Since the moment at the end support is zero a moment is applied to counterbalance the constant moment. The effect of this moment on the intermediate support moment is:



$$\phi_{21} = -\frac{M_1 \cdot \alpha \cdot L}{6 \cdot EI} + \frac{M_2 \cdot \alpha \cdot L}{3 \cdot EI} \quad (C.4)$$

$$\phi_{21} = \phi_{23} \quad (C.5)$$

$$-\frac{M_1 \cdot \alpha \cdot L}{6 \cdot EI} + \frac{M_2 \cdot \alpha \cdot L}{3 \cdot EI} = -\frac{M_2 \cdot L}{3 \cdot EI} - \frac{M_2 \cdot L}{6 \cdot EI} \quad (\text{C.6})$$

$$M_2 = M_1 \cdot \frac{\frac{\alpha}{6}}{\frac{1}{2} + \frac{\alpha}{3}} \quad (\text{C.7})$$

In which:

$$M_1 = M(\Delta T) \quad (\text{C.8})$$

The resulting bending moment above the intermediate supports due to thermal loading is:

$$M_{support}(\Delta T) = M(\Delta T) + M_2 \quad (\text{C.9})$$

$$M_{support}(\Delta T) = M(\Delta T) \left( 1 + \frac{\frac{\alpha}{6}}{\frac{1}{2} + \frac{\alpha}{3}} \right) \quad (\text{C.10})$$

## Appendix D

### Tendon profile

#### D.1 Single span

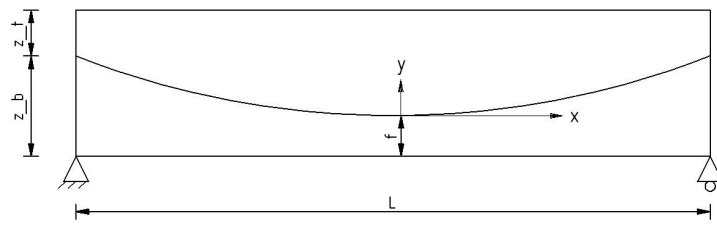


Figure D.1: Tendon profile single span structure

Parabolic function:

$$g(x) = C_1 \cdot x^2 + C_2 \cdot x + C_3 \quad (\text{D.1})$$

Boundary conditions:

$$g\left(\frac{1}{2}L\right) = z_b - f \quad (\text{D.2})$$

$$g(0) = 0 \quad (\text{D.3})$$

$$g'(0) = 0 \quad (\text{D.4})$$

Solving boundary conditions gives.

$$\begin{aligned} C_3 &= 0 \\ C_2 &= 0 \\ C_1 &= \frac{4 \cdot (z_b - f)}{L^2} \end{aligned}$$

Substitution in the original function gives:

$$g(x) = \frac{4(z_b - f)}{L^2} \cdot x^2 \quad (\text{D.5})$$

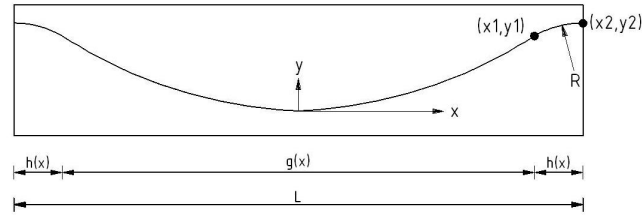


Figure D.2: Tendon profile in midspan

## D.2 Three spans

### D.2.1 Midspan

Parabolic functions:

$$g(x) = C_1 \cdot x^2 \quad (\text{D.6})$$

$$h(x) = C_2 \cdot x^2 + C_3 \cdot x + C_4 \quad (\text{D.7})$$

Boundary conditions:

$$h(x_2) = y_2 \quad (\text{D.8})$$

$$h'(x_2) = 0 \quad (\text{D.9})$$

$$h''(x_2) = \frac{1}{R} \quad (\text{D.10})$$

$$g(x_1) = h(x_1) \quad (\text{D.11})$$

$$g'(x_1) = h'(x_1) \quad (\text{D.12})$$

Solving the boundary conditions D.8, D.9 and D.10 gives:

$$h''(x_2) = 2 \cdot C_2 = \frac{1}{R} \Rightarrow C_2 = \frac{1}{2 \cdot R} \quad (\text{D.13})$$

$$h'(x_2) = 0 \Rightarrow 2 \cdot C_2 \cdot x_2 + C_3 = 0 \Rightarrow C_3 = -\frac{x_2}{R} \quad (\text{D.14})$$

$$h(x_2) = \frac{1}{R} \cdot \left( \frac{x_2^2}{2} - x_2^2 \right) + C_4 = y_2 \Rightarrow C_4 = y_2 + \frac{x_2^2}{2 \cdot R} \quad (\text{D.15})$$

$$h(x) = \frac{1}{2 \cdot R} (x - x_2)^2 + y_2 \quad (\text{D.16})$$

Solving boundary conditions D.11 and D.12 gives:

$$g'(x_1) = h'(x_1) \Rightarrow 2 \cdot C_1 \cdot x_1 = \frac{x_1 - x_2}{R} \Rightarrow C_1 = \frac{x_1 - x_2}{2 \cdot x_1 \cdot R} \quad (\text{D.17})$$

$$g(x_1) = h(x_1) \Rightarrow \frac{x_1 - x_2}{2 \cdot x_1 \cdot R} \cdot x_1^2 = \frac{1}{2R} \cdot (x_1 - x_2)^2 + y_2 \quad (\text{D.18})$$

$$x_1 = 2 \cdot \frac{y_2}{x_2} \cdot R + x_2 \quad (\text{D.19})$$

$$g(x) = \frac{1}{2R + \frac{x_2^2}{y_2}} \cdot x^2 \quad (\text{D.20})$$

## D.2.2 Endspan

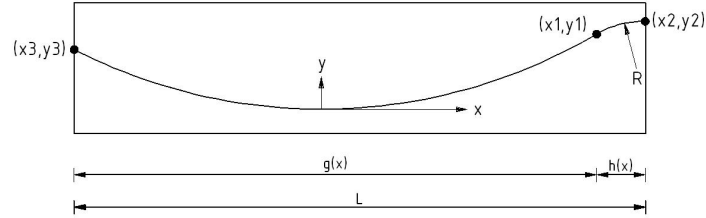


Figure D.3: Tendon profile in endspan

Parabolic functions:

$$g(x) = C_1 \cdot x^2 \quad (\text{D.21})$$

$$h(x) = C_2 \cdot x^2 + C_3 \cdot x + C_4 \quad (\text{D.22})$$

Boundary conditions:

$$h(x_2) = y_2 \quad (\text{D.23})$$

$$h'(x_2) = 0 \quad (\text{D.24})$$

$$h''(x) = \frac{1}{R} \quad (\text{D.25})$$

$$g(x) = h(x) \quad (\text{D.26})$$

$$g'(x) = h'(x) \quad (\text{D.27})$$

$$g(x_3) = y_3 \quad (\text{D.28})$$

$$x_3 = x_2 - L \quad (\text{D.29})$$

Solving the boundary conditions gives:

$$h''(x_2) = 2 \cdot C_2 = \frac{1}{R} \Rightarrow C_2 = \frac{1}{2 \cdot R} \quad (\text{D.30})$$

$$h'(x_2) = 0 \Rightarrow 2 \cdot C_2 \cdot x_2 + C_3 = 0 \Rightarrow C_3 = -\frac{x_2}{R} \quad (\text{D.31})$$

$$h(x_2) = \frac{1}{R} \cdot \left( \frac{x_2^2}{2} - x_2^2 \right) + C_4 = y_2 \Rightarrow C_4 = y_2 + \frac{x_2^2}{2 \cdot R} \quad (\text{D.32})$$

$$h(x) = \frac{1}{2 \cdot R} (x - x_2)^2 + y_2 \quad (\text{D.33})$$

$$g'(x_1) = h'(x_1) \Rightarrow 2 \cdot C_1 \cdot x_1 = \frac{x_1 - x_2}{R} \Rightarrow C_1 = \frac{x_1 - x_2}{2 \cdot x_1 \cdot R} \quad (\text{D.34})$$

$$g(x_3) = y_3 \Rightarrow \frac{(x_2 - L)^2}{2R + \frac{x_2^2}{y_2}} = y_3 \quad (\text{D.35})$$

$$x_2 = \frac{L \pm \sqrt{\frac{y_3}{y_2} \cdot (L^2 - 2R \cdot y_3) + 2R \cdot y_3}}{1 - \frac{y_3}{y_2}} \quad (\text{D.36})$$

$$g(x) = \frac{1}{2R + \frac{x_2^2}{y_2}} \cdot x^2 \quad (\text{D.37})$$



## Appendix E

# Manual Calculation - One span

### E.1 Geometry

The manual calculation as a verification of the computer model has been performed for the span of forty meters. The geometry in this manual calculation is the result of the model. The cross-section has been defined with the dimensions described below and has a total concrete area of  $A_c = 4661920 \text{ mm}^2$ .

wall height	$h$	3080	mm
wall thickness	$b_w$	562	mm
floor thickness	$t_b$	300	mm
internal width	$b_i$	4000	mm
outer width	$b_d$	5124	mm

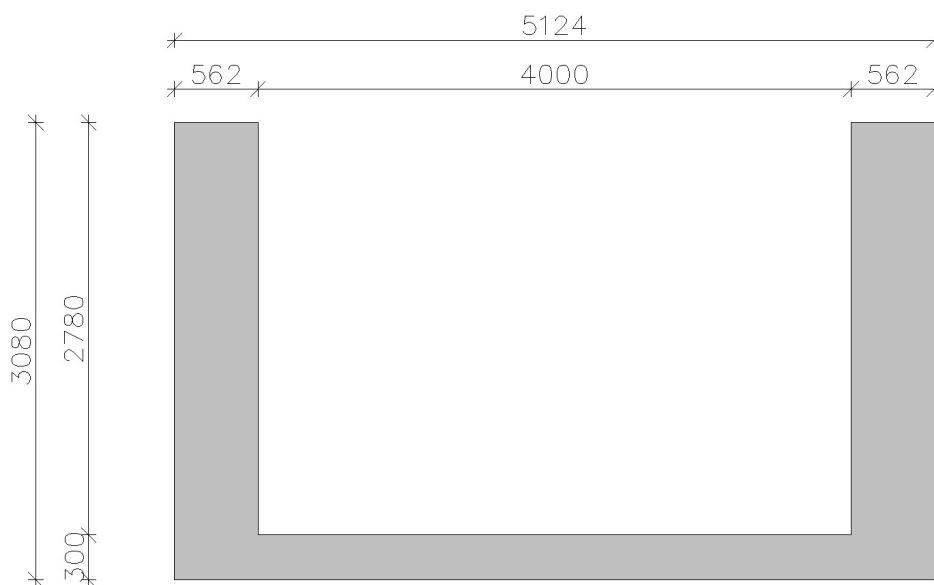


Figure E.1: Cross section

Further cross section properties:

Neutral line.

$$y_{bottom} = \frac{1}{A_c} \left( \frac{1}{2} \cdot b_i \cdot t_b^2 + 2 \cdot \frac{1}{2} b_w \cdot h^2 \right) \quad (E.1)$$

$$y_{bottom} = \frac{1}{4661920} \left( \frac{1}{2} \cdot 4000 \cdot 300^2 + 2 \cdot \frac{1}{2} \cdot 562 \cdot 3080^2 \right) = 1898 \text{ mm} \quad (E.2)$$

$$y_{top} = h - y_{bottom} = 1182 \text{ mm} \quad (E.3)$$

Moment of inertia:

section	equation	value	unit
floor	$\frac{1}{12} \cdot b_d \cdot t_b^3 + b_d \cdot t_b \cdot (y_b - \frac{1}{2} t_b)^2$	$1.29 \cdot 10^{12}$	$mm^4$
walls	$\frac{2}{12} \cdot b_w \cdot h^3 + 2 \cdot b_w \cdot h \cdot (y_t - \frac{1}{2} \cdot h)^2$	$3.18 \cdot 10^{12}$	$mm^4$
total		$4.47 \cdot 10^{12}$	$mm^4$

Table E.1: Calculation of moment of inertia

This gives the following section moduli:

$$W_{bot} = \frac{I_{yy}}{y_{bottom}} = 3.78 \cdot 10^9 \text{ mm}^3 \quad (E.4)$$

$$W_{top} = \frac{I_{yy}}{y_{top}} = 2.36 \cdot 10^9 \text{ mm}^3 \quad (E.5)$$

## E.2 Loads

### E.2.1 Self weight

Self weight of the structure:

$$q_{g,k} = \gamma_c \cdot A_c = 29 \cdot 4.66 = 135 \text{ kN/m} \quad (E.6)$$

$$M_{g,k} = -\frac{1}{2} \cdot q_{g,k} \cdot x^2 + \frac{1}{2} \cdot q_{g,k} \cdot L \cdot x \quad (E.7)$$

With a maximum moment at  $x = 20 \text{ m}$  of  $M_{g,k} = 27028 \text{ kNm}$  and a maximum shear force at the supports of  $V_{g,k} = \frac{1}{2} \cdot q_{g,k} \cdot L = 2703 \text{ kN}$ .

### E.2.2 Railroad track

Self weight of the railroad track:

$$q_{track,k} = \gamma_t \cdot t_{track} \cdot b_i = 22 \cdot 0.58 \cdot 4.0 = 51 \text{ kN/m} \quad (E.8)$$

$$M_{track,k} = -\frac{1}{2} \cdot q_{track,k} \cdot x^2 + \frac{1}{2} \cdot q_{track,k} \cdot L \cdot x \quad (E.9)$$

With a maximum at  $x = 20 \text{ m}$  of  $M_{track,k} = 10200 \text{ kNm}$  and a maximum shear force at the supports of  $V_{track,k} = \frac{1}{2} \cdot q_{track,k} \cdot L = 1020 \text{ kN}$ .

### E.2.3 Load model 71

The load model consists of two infinite length block loads and four axle loads. For simplicity of the manual calculation the block loads have been combined to a continuous load and the axle loads have been combined to one point load. The magnitude of the loads are calculated by multiplying the characteristic load with the factor  $\alpha = 1.21$  and the dynamic factor  $\Phi_3$ .

$$\Phi_3 = \frac{2.16}{\sqrt{L_\Phi} - 0.2} + 0.73 \quad (\text{E.10})$$

$$L_\Phi = 40 \text{ m} \quad (\text{E.11})$$

$$\Phi_3 = \frac{2.16}{\sqrt{40} - 0.2} + 0.73 = 1.08 \quad (\text{E.12})$$

$$q_{v,k} = 80 \cdot \alpha \cdot \Phi_3 = 80 \cdot 1.21 \cdot 1.08 = 105 \text{ kN/m} \quad (\text{E.13})$$

$$M_{q,k} = \frac{1}{8} \cdot 105 \cdot 40^2 = 21000 \text{ kNm} \quad (\text{E.14})$$

$$Q_{v,k} = 250 \cdot \alpha \cdot \Phi_3 = 250 \cdot 1.21 \cdot 1.08 = 327 \text{ kN} \quad (\text{E.15})$$

$$M_{Q,k} = \frac{1}{4} \cdot 4 \cdot Q_{v,k} \cdot L = \frac{1}{4} \cdot 327 \cdot 40 = 13080 \text{ kNm} \quad (\text{E.16})$$

Together the bending moment due to load model 71 is:

$$M_{LM71,k} = 21000 + 13080 = 34080 \text{ kNm} \quad (\text{E.17})$$

The maximum shear force is:

$$V_{LM71,k} = \frac{1}{2}(q_{v,k} \cdot L + 4 \cdot Q_{v,k}) = \frac{1}{2}(105 \cdot 40 + 4 \cdot 327) = 2754 \text{ kN} \quad (\text{E.18})$$

### E.2.4 SW0

As the total length of the load model SW0 is 35.3 meters the position for the load model to achieve the maximum bending moment will be in the middle of the span as the length of the span is larger than the length of the load model.

$$q_{vk} = 133 \cdot 1.21 \cdot 1.08 = 174 \text{ kN/m} \quad (\text{E.19})$$

$$V_{SW0,k} = \frac{1}{2} \cdot 2a \cdot q_{vk} = 2610 \text{ kN} \quad (\text{E.20})$$

$$M_{sw0,k} = -\left(\frac{1}{2} \cdot 5.3 + \frac{1}{2} \cdot 15\right) \cdot 174 \cdot 15 + \frac{1}{2} \cdot 40 \cdot 2610 = 25709 \text{ kNm} \quad (\text{E.21})$$

### E.2.5 SW2

As the total length of the load model SW2 is 53 meters the position for the load model is placed at the beginning of the span. Due to the statically determined structure the bending moment at  $x=20$  can easily be calculated.

$$q_{vk} = 150 \cdot 1.21 \cdot 1.08 = 196 \text{ kN/m} \quad (\text{E.22})$$

$$\sum M = 0 = -\frac{1}{2} \cdot 25^2 \cdot 196 - 8 \cdot 196 \cdot 36 + R_b \cdot 40 = -117698 + R_b \cdot 40 \text{ kNm} \quad (\text{E.23})$$

$$R_b = 117698/40 = 2942 \text{ kN} \quad (\text{E.24})$$

$$R_a = (25 + 8) \cdot 196 = 3526 \text{ kN} \quad (\text{E.25})$$

The bending moment at the middle cross section is:

$$M_{sw2,k} = 3526 \cdot 20 - \frac{1}{2} \cdot 196 \cdot 20^2 = 31320 \text{ kNm} \quad (\text{E.26})$$

The maximum shear force occurs at support a with a magnitude of  $V_{sw2,k} = 3526 \text{ kN}$ .

## E.2.6 Fatigue loading

The composition of heavy traffic consists of four real train load models. The load effects are required to be multiplied with a dynamic load factor for fatigue. This dynamic load factor  $\phi_{fat}$  is found to be:

$$K = \frac{v}{47.16L^{0.408}} = \frac{200}{47.16 \cdot 40^{0.408}} = 0.94 \quad (E.27)$$

$$\phi' = \frac{K}{1 - K + K^4} = \frac{0.94}{1 - 0.94 + 0.94^4} = 1.12 \quad (E.28)$$

$$\phi'' = 0.56 \cdot e^{-\frac{L_{\phi}^2}{100}} = 0.56 \cdot e^{-\frac{40^2}{100}} = 6.3 \cdot 10^{-8} \quad (E.29)$$

$$\phi_{fat} = 1 + \frac{1}{2}(\phi' + \frac{1}{2}\phi'') = 1.56 \quad (E.30)$$

The fatigue load models exist of concentrated loads representing the train axles. The equivalent for these load models exist of a continuous spread load. The corresponding bending moment can be calculated by equation E.31.

$$M_{fat,k} = \frac{1}{8} \cdot (\phi_{fat} \cdot q_k) \cdot L^2 \quad (E.31)$$

Table E.2.6 gives the value of the spread load for each model and the corresponding largest bending moment at  $x = 20 \text{ m}$ .

Load model	$q_k$ [kN/m]	$M_{fat,k}$ [kNm]
5	80	24960
6	43	13416
11	57.2	17846
12	53.4	16661

Table E.2: fatigue loading

## E.3 Load combinations

### E.3.1 Ultimate limit state

The largest bending moment due to life loads is that of load model LM71. The load combination for the ultimate limit state is defined as the largest of the following two equations:

$$M_{Ed} = \gamma_{G,i,sup} G_{k,j,sup} + \gamma_P P + \gamma_{Q,1} \Psi_{0,1} Q_{k,1} \quad (E.32)$$

$$M_{Ed} = \gamma_{G,i,sup} G_{k,j,sup} + \gamma_P P + \gamma_{Q,1} Q_{k,1} \quad (E.33)$$

Evaluating these equations gives:

$$M_{Ed} = 1.5 \cdot (27028 + 10200) + 1.35 \cdot 34080 = 101850 \text{ kNm} \quad (E.34)$$

$$M_{Ed} = 1.3 \cdot (27028 + 10200) + 1.65 \cdot 34080 = 104628 \text{ kNm} \quad (E.35)$$

The effective ultimate bending moment is  $M_{Ed} = 104628 \text{ kNm}$ .

The same combinations apply to the shear force.

$$V_{Ed} = 1.5 \cdot (2703 + 1020) + 1.35 \cdot 3526 = 10345 \text{ kN} \quad (E.36)$$

$$V_{Ed} = 1.3 \cdot (2703 + 1020) + 1.65 \cdot 3526 = 10658 \text{ kN} \quad (E.37)$$

The effective ultimate shear force is  $V_{Ed} = 10658 \text{ kN}$ .

### E.3.2 Serviceability limit state

The SLS defines three different combinations for the loadings. These are as follows:

$$\text{Characteristic combination } \sum_{j \geq 1} = G_{k,j} + P + Q_{k,1} + \sum_{i > 1} \Psi_{0,i} Q_{k,i} \quad (\text{E.38})$$

$$\text{Frequent combination } \sum_{j \geq 1} = G_{k,j} + P + \Psi_{1,1} Q_{k,1} + \sum_{i > 1} \Psi_{2,i} Q_{k,i} \quad (\text{E.39})$$

$$\text{Quasi-permanent combination } \sum_{j \geq 1} = G_{k,j} + P + \sum_{i \geq 1} \Psi_{2,i} Q_{k,i} \quad (\text{E.40})$$

This gives the following effective forces acting on the structure.

Quasi-permanent

$$M_{Ed,qp} = 1.0 \cdot 27028 + 1.0 \cdot 10200 + 0.0 \cdot 34080 = 37228 \text{ kNm} \quad (\text{E.41})$$

Frequent

$$M_{Ed,fr} = 1.0 \cdot 27028 + 1.0 \cdot 10200 + 0.8 \cdot 34080 = 64492 \text{ kNm} \quad (\text{E.42})$$

Characteristic

$$M_{Ed,ch} = 1.0 \cdot 27028 + 1.0 \cdot 10200 + 1.0 \cdot 34080 = 71308 \text{ kNm} \quad (\text{E.43})$$

The load combination in which the structure is the least loaded is during construction when only the concrete structure is present yet. This situation belongs to the characteristic loading combination.

$$M_{Ed,construction} = 1.0 \cdot M_{G,k} = 27028 \text{ kNm} \quad (\text{E.44})$$

A quasi-permanent load combination which will be used is the situation where the track is situated on the bridge, but no life load is present.

$$M_{Ed,qp2} = 1.0 \cdot (M_{G,k} + M_{track,k}) = 37228 \text{ kNm} \quad (\text{E.45})$$

## E.4 Prestressing

### E.4.1 Tendon profile

The tendon profile is defined as a parabola by:

$$g(x) = \frac{4 \cdot f}{L^2} \cdot x^2 \quad (\text{E.46})$$

The origin of the local coordinate system is halfway the length of the beam and at a point 306 mm from the bottom of the beam. At the ends of the structure the eccentricity of the tendon profile is 218 mm above the neutral axis. This makes the drap in the structure  $f = 1094 \text{ mm}$  and the radius of the cable  $R = \frac{40^2}{8 \cdot 1.094} = 183 \text{ m}$ .

### E.4.2 Friction losses

The prestressing force after frictions losses has been calculated according to:

$$P(x) = P_0 \cdot e^{-\mu(\Delta\theta + k \cdot x)} \quad (\text{E.47})$$

in which:

$$\begin{array}{ll} \mu = 0.17 & [-] \quad \text{friction coefficient} \\ k = 0.008 & [rad/m] \quad \text{wobble effect} \end{array}$$

The absolute angular rotation can be calculated according to the derivative of the tendon profile to  $x$ .

$$g'(x) = \frac{8 \cdot f}{L^2} \cdot x \quad (\text{E.48})$$

The curvature in the structure is constant. This gives that there are three points in the local coordinate system which need to be evaluated in order to define the angular rotation. Table E.4.2 shows the angular rotations and the corresponding friction losses at these locations.

$x - \text{global [m]}$	$x - \text{local [m]}$	$g'(x) [-]$	$\Delta\theta [\text{rad}]$	$P(x)/P_0 [-]$
0	-20	-0.11	0	1.00
20	0	0	0.11	0.96
40	20	0.22	0.22	0.91

Table E.3: Friction losses

The influence of the wedge settlement works over the length  $l_{set}$ . The assumed wedge settlement is  $w_{set} = 10 \text{ mm}$ .

$$l_{set} = \left( \frac{w_{set} \cdot E_p}{\frac{\Delta\sigma_p}{\Delta x}} \right)^{0.5} = \left( \frac{10 \cdot 1.95 \cdot 10^5}{2.0 \cdot 10^{-3}} \right)^{0.5} = 31.2 \text{ m} \quad (\text{E.49})$$

$$P(31.2)/P_0 = 1 - 2.0 \cdot 10^{-3} \cdot 31.2 = 0.94 \quad (\text{E.50})$$

$$P(0) = 1.00 - 2 \cdot (1 - 0.94) = 0.88 \quad (\text{E.51})$$

This makes the average prestressing after friction losses and wedge settlement  $P_{mean} = 0.91 \cdot P_0$ .

### E.4.3 Initial prestressing force

The initial prestressing force has been found by applying the OVS-stress criteria as boundary conditions to the cross section analysis on the middle cross section. The time dependent losses are estimated to be 15%. This allows to compare the prestressing force boundary conditions on different moments in time. The results are presented in table E.4.3.

Load combination	Location	$\sigma_{max} [N/mm^2]$	$P_{m\infty} [kN]$	$P_{m0} [kN]$
construction	bottom	3	--	$\geq 9300$
construction	top	3	--	$\leq 92241$
frequent	bottom	0	$\geq 38233$	$\geq 44980$
frequent	top	1.5	$\leq 183984$	$\leq 216451$
quasi-permanent	bottom	0	$\geq 22070$	$\geq 25945$
quasi-permanent	top	0	$\leq 100678$	$\leq 118444$
characteristic	bottom	1.5	$\geq 37231$	$\geq 43802$
characteristic	top	2.25	$\leq 202417$	$\leq 238137$

Table E.4: Boundary conditions to prestressing force

These results give that the maximum and minimum allowable prestressing force respectively are:

$$P_{m0,max} = 92241 \text{ kN} \quad (\text{E.52})$$

$$P_{m0,min} = 44980 \text{ kN} \quad (\text{E.53})$$

The applied prestressing force is taken to be  $P_{m0} = 44980 \text{ kN}$ . This means that the prestressing force at tensioning is required to be  $P_0 = P_{m0}/0.91 = 49429 \text{ kN}$ .

#### E.4.4 Applied prestressing

The required prestressing area is:

$$A_p = \frac{P_0}{\sigma_{pi}} = \frac{P_0}{0.8 \cdot f_{pu}} = \frac{49429 \cdot 10^3}{0.8 \cdot 1690} = 36560 \text{ mm}^2 \quad (\text{E.54})$$

Apply 16 cables consisting of 19 strands with each an area of  $140 \text{ mm}^2$ . This gives an applied prestressing area of  $A_p = 16 \cdot 19 \cdot 140 = 42560 \text{ mm}^2$ . The stress in the prestressing steel is now at prestressing:

$$\sigma_{p0} = \frac{49429 \cdot 10^3}{42560} = 1162 \text{ N/mm}^2 \quad (\text{E.55})$$

The prestressing cables are applied in a cable configuration of eight cables in each trough wall in which they are ordered in four pairs. At the ends of the structure the height of the wall should be sufficient to place all the anchors. The required anchor height is 300 mm. When an intermediate spacing of 50 mm is applied the required height for the anchors is 1450 mm. Half of this height is required to be available below and above the center of the prestressing.

Top:  $h - y_b - 100 = 3080 - 1182 - 100 = 1798 \text{ mm} > 725 \text{ mm}$

Bottom:  $h - y_t - 100 = 3080 - 1898 - 100 = 1082 \text{ mm} > 725 \text{ mm}$

#### E.4.5 Time dependent losses

Creep

The stress at the location of the prestressing cable due to  $P_{m0}$  and the quasi-permanent load combination is:

$$\sigma_c = -\frac{P_{m0}}{A_c} - \frac{P_{m0} \cdot e_p^2}{I_{yy}} + \frac{M_{Ed,qp} \cdot e_p}{I_{yy}} = -10 \text{ N/mm}^2 \quad (\text{E.56})$$

The creep strain is calculated in which the material properties  $E_c = 1.05 \cdot E_{cm} = 57750 \text{ N/mm}^2$  and  $\phi(\infty, t_0) = 0.5$ .

$$\epsilon_{cc}(\infty, t_0) = 0.5 \cdot \frac{-10}{57750} = -0.087 \text{ }^\circ/\text{ }_\infty \quad (\text{E.57})$$

Shrinkage

Autogeneous shrinkage:

$$\epsilon_{ca} = 2.5(f_{ck} - 10) \cdot 10^{-6} = 2.5(172 - 10) \cdot 10^{-6} = 4.05 \cdot 10^{-4} \quad (\text{E.58})$$

Drying shrinkage is given to be less than or equal to  $\epsilon_{cd} = 10^{-5}$ . Total shrinkage is:

$$\epsilon_{cs} = 10^{-5} + 4.05 \cdot 10^{-4} = 0.415 \text{ }^\circ/\text{ }_\infty \quad (\text{E.59})$$

Relaxation

$$\frac{\Delta\sigma_{pr}}{\sigma_{pi}} = 0.66 \cdot \rho_{1000} \cdot e^{9.1\mu} \left( \frac{t}{1000} \right)^{0.75(1-\mu)} \cdot 10^{-5} \quad (\text{E.60})$$

In which  $\rho_{1000} = 2.5\%$  and  $t = 876000$  hours and:

$$\sigma_{pi} = \frac{0.95 \cdot P_0}{A_p} = \frac{0.95 \cdot 49429 \cdot 10^3}{42560} = 1103 \text{ N/mm}^2 \quad (\text{E.61})$$

$$\mu = \frac{\sigma_{pi}}{f_{pk}} = \frac{1103}{1860} = 0.59 \quad (\text{E.62})$$

$$\Delta\sigma_{pr} = 1103 \cdot 0.59 \cdot 2.5 \cdot e^{9.1 \cdot 0.59} \left( \frac{876000}{1000} \right)^{0.75(1-0.59)} \cdot 10^{-5} = 28 \text{ N/mm}^2 \quad (\text{E.63})$$

The total time dependent losses are:

$$\Delta\sigma_p = (\epsilon_{cc} + \epsilon_{cs}) \cdot E_p + \Delta\sigma_{pr} \quad (\text{E.64})$$

$$\Delta\sigma_p = (0.087 + 0.415) \cdot 10^{-3} \cdot 1.95 \cdot 10^5 + 28 = 125 \text{ N/mm}^2 \quad (\text{E.65})$$

$$\sigma_{pm0} = \frac{P_{m0}}{A_p} = \frac{44980 \cdot 10^3}{42560} = 1057 \text{ N/mm}^2 \quad (\text{E.66})$$

$$t_{dl} = \frac{\Delta\sigma_p}{\sigma_{pm0}} = \frac{125}{1057} \cdot 100\% = 11.9\% \quad (\text{E.67})$$

The prestressing force at  $t = \infty$  is  $P_{m\infty} = 39638 \text{ kN}$ . This is greater than the minimum required force  $P_{m\infty, \min} = 38233 \text{ kN}$ .

The upward load due to the prestressing load is:

$$q_{p,k} = \frac{8 \cdot P_{m\infty} \cdot f}{l^2} = 217 \text{ kN/m} \quad (\text{E.68})$$

## E.5 Verifications - main structure

### E.5.1 ULS - Bending moment capacity

The effective width of the concrete is a function of the the span. As the effective width might become less than the actual width of the structure, the bending moment capacity has been regarded per trough wall. The effective width of the floor in this case has been calculated as:

$$b_{eff,1} = 0.2 \cdot b_i + 0.1 \cdot l_0 \leq 0.5 \cdot b_i \leq 0.2 \cdot l_0 \quad (\text{E.69})$$

$$b_{eff,1} = 0.2 \cdot 4000 + 0.1 \cdot 40000 \leq 0.5 \cdot 4000 \leq 0.2 \cdot 40000 \quad (\text{E.70})$$

$$b_{eff,1} = 4400 \leq 2000 \leq 8000 \quad (\text{E.71})$$

The effective width of the floor is half of the width  $b_{eff} = 2000 + 562 = 2562 \text{ mm}$ .

The applied reinforcement is practical reinforcement of  $\varnothing 16 - 150\text{mm}$  in one layer at the bottom of the floor. The reinforcement area in the effective width is:

$$A_s = \frac{b_{eff}}{s} \cdot \frac{1}{4} \cdot \pi \cdot d_r^2 = \frac{2562}{150} \cdot \frac{1}{4} \cdot \pi \cdot 16^2 = 3434 \text{ mm}^2 \quad (\text{E.72})$$

In order to find the height of the compression zone  $x$  the horizontal equilibrium is evaluated.

$$N_c = N_s + N_t + \Delta P + P_{m\infty} \quad (\text{E.73})$$

in which  $N_t$  is the tensile force in the concrete. This  $N_t$  is the sum of three different parts in the stress diagram.

$$\begin{aligned} T_1 &= \frac{1}{2} f_{ctd} \cdot x_1 \cdot b_w \\ T_2 &= f_{ctd} \cdot x_2 \cdot b_w \\ T_3 &= \frac{1}{2} f_{ctd} \cdot x_3 \cdot b_w \end{aligned} \quad (E.74)$$

The distances  $x_1$ ,  $x_2$  and  $x_3$  can be calculated by:

$$\begin{aligned} \kappa_x &= \frac{\varepsilon_{sy}}{z - x} \\ x_1 &= \frac{\varepsilon_{ct}}{\kappa_x} = \frac{\varepsilon_{ct}}{\varepsilon_{sy}} (z - x) \\ x_2 &= \frac{\varepsilon_{ctd} - \varepsilon_{ct}}{\kappa_x} = \frac{\varepsilon_{ctd} - \varepsilon_{ct}}{\varepsilon_{sy}} (z - x) \\ x_3 &= \frac{\varepsilon_{ctu} - \varepsilon_{ctd}}{\kappa_x} = \frac{\varepsilon_{ctu} - \varepsilon_{ctd}}{\varepsilon_{sy}} (z - x) \end{aligned} \quad (E.75)$$

The horizontal equilibrium can now be expressed in a function with only one unknown  $x$ .

$$N_c = N_s + N_t + \Delta P + P_{m\infty} \quad (E.76)$$

$$\alpha \cdot f_{cd} \cdot b_w \cdot x = f_{ctd} \cdot b_w \cdot \left( \frac{1}{2} x_1 + x_2 + \frac{1}{2} x_3 \right) + A_s \cdot f_{yd} + (f_{pd} - \sigma_{p\infty}) \cdot A_p + P_{m\infty} \quad (E.77)$$

This is now an equation with only the unknown  $x$ . Solving this equation gives  $x = 1386 \text{ mm}$ . The length of the concrete tension zone is calculated to be  $x_T = 11197 \text{ mm}$ . This is larger than the cross section height. Therefore the cross section is reevaluated in a situation where  $x_3$  is limited by the height of the cross section.

A variable  $x_3^*$  is introduced. This is the length of  $x_3$  in case there would be no limit to it. The actual length of  $x_3$  equals  $x_3 = h - x - x_1 - x_2$ . The concrete tensile force is now calculated according to the second scheme in figure E.2. The equations from E.74 now become:

$$\begin{aligned} T_1 &= \frac{1}{2} f_{ctd} \cdot x_1 \cdot b_w \\ T_2 &= f_{ctd} \cdot x_2 \cdot b_w \\ T_3 &= (f_{ctd} - \theta_t \cdot x_3) \cdot x_3 \cdot b_w \\ T_4 &= \frac{1}{2} \cdot \theta_t \cdot x_3 \cdot b_w \end{aligned} \quad (E.78)$$

In this  $\theta_t = \frac{f_{ctd}}{x_3^*}$ .

Solving equation E.77 now gives  $x = 1000 \text{ mm}$ . The horizontal equilibrium now consists of the following horizontal forces:

$$\begin{aligned} N_c &= 46762 \text{ kN} \\ N_t &= 9252 \text{ kN} \\ N_s &= 1518 \text{ kN} \\ \Delta P &= 16173 \text{ kN} \\ P_{m\infty} &= \frac{1}{2} \cdot 39638 \text{ kN} \end{aligned} \quad (E.79)$$

As control the strain in the steel is calculated. Due to the high compressive strength it might occur that only a small compressive height is required for horizontal equilibrium. This can lead to a large curvature which may cause the steel to break.

$$\kappa_x = \frac{\varepsilon_{cu3}}{x} = \frac{2.6 \cdot 10^{-3}}{1000} = 2.60 \cdot 10^{-6} \quad (E.80)$$

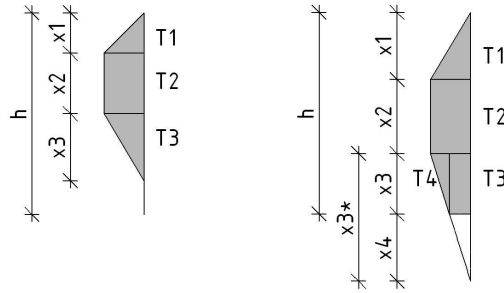


Figure E.2: Tension zone in the concrete. Left: cracked. Right: uncracked.

$$\varepsilon_s = \kappa_x \cdot (d - x) = 2.60 \cdot 10^{-6} \cdot (3052 - 1000) \cdot 10^3 = 5.34^\circ / \infty \quad (\text{E.81})$$

The steel strain is greater than the yield strain  $\varepsilon_{sy} = 2.2^\circ / \infty$  and smaller than the ultimate strain  $\varepsilon_{su} = 32.5^\circ / \infty$ .

The maximum compressive height  $x_u$  is calculated and should be greater than  $x$  in order to prevent compressive failure.

$$f = \frac{(f_{pd} - \sigma_{p\infty})A_p^* + f_{yd}A_s}{A_p^* + A_s} = 569 \text{ N/mm}^2 \quad (\text{E.82})$$

$$k_3 = \frac{7 \cdot f}{\varepsilon_{cu3} \cdot 10^6 + 7 \cdot f} = 0.61 \quad (\text{E.83})$$

$$x_u = (1 - k_3) \cdot d = 1205 \text{ mm} \quad (\text{E.84})$$

The maximum compressive height  $x_u = 1205 \text{ mm}$  is greater than the occurring compressive height  $x = 1000 \text{ mm}$ .

The bending moment capacity can now be calculated according to equation E.85.

$$M_{ud} = N_c \cdot (1 - \beta) \cdot x + \frac{2}{3} \cdot T_1 \cdot x_1 + T_2 \cdot (x_1 + 0.5 \cdot x_2) + T_3 \cdot (x_1 + x_2 + \frac{1}{2} \cdot x_3) + T_4 \cdot (x_1 + x_2 + \frac{1}{3} \cdot x_3) + N_s \cdot (z - x) + \Delta P \cdot (y_t + e_p - x) \quad (\text{E.85})$$

For the concrete which reaches the ultimate strain  $\beta = 0.36$ . The values of  $T_1$  trough  $T_4$  according to equations from F.166 are:

$$\begin{aligned} T_1 &= 99 \text{ kN} \\ T_2 &= 3085 \text{ kN} \\ T_3 &= 4954 \text{ kN} \\ T_4 &= 1116 \text{ kN} \end{aligned} \quad (\text{E.86})$$

Evaluating equation E.85 gives for the ultimate bending moment capacity  $M_{ud} = 71135 \text{ kNm}$ . The effective bending moment capacity on one trough beam is  $M_{Ed} = 0.5 \cdot 104628 - 0.5 \cdot 39638 \cdot 0.88 = 34873 \text{ kNm}$ . Performing a unity check for the bending moment capacity in the ultimate limit state gives:

$$u.c. = \frac{M_{Ed}}{M_{ud}} = \frac{34873}{71135} = 0.49 < 1.0 \quad (\text{E.87})$$

### E.5.2 ULS - Shear capacity

The shear force capacity of the individual components of the concrete, reinforcement and steel fibres have been calculated below.

Concrete.

$$V_{Rd,c} = \left( C_{Rdc} \cdot k \cdot (100 \cdot \rho_1 \cdot f_{ck})^{1/3} + k_1 \cdot \sigma_{cp} \right) \cdot b_w \cdot d \cdot 10^{-3} \quad (E.88)$$

In which:

$$\begin{aligned} C_{Rdc} &= \frac{0.18}{\gamma_c} = 0.12 & [-] \\ k &= \sqrt{1 + \frac{200}{d}} \leq 2.0 = 1.03 & [-] \\ \rho_1 &= \frac{A_s}{b_w \cdot d} = 4.08 \cdot 10^{-4} & [-] \\ f_{ck} &= 172 & N/mm^2 \\ k_1 &= 0.15 & [-] \\ \sigma_{cp} &= \frac{P_{m\infty}}{A_c} \leq 0.2 \cdot f_{cd} = 8.50 & N/mm^2 \end{aligned} \quad (E.89)$$

Evaluation equation F.190 with the values from E.89 gives  $V_{Rdc} = 2592 \text{ kN}$ .

Shear reinforcement.

$$V_{Rd,s} = 0.9 d \frac{A_{sw}}{s} f_{y;d} (\sin \alpha + \cos \alpha) \quad (E.90)$$

In which:

$$\begin{aligned} A_{sw} &= 2 \cdot \frac{1}{4} \cdot \pi \cdot \varnothing_l^2 = 628 \text{ mm}^2 \\ s &= 100 \text{ mm} \\ \alpha &= 90^\circ \end{aligned} \quad (E.91)$$

This gives a capacity of the shear reinforcement of  $V_{Rds} = 7282 \text{ kN}$ .

Fibres

$$V_{Rd,f} = \frac{S \cdot \sigma_p}{\gamma_f \cdot \tan \theta} \quad (E.92)$$

In which:

$$\begin{aligned} S &= 0.9 \cdot b_w \cdot (h - t_b) = 1.41 \cdot 10^6 \text{ mm}^2 \\ \sigma_p &= 8 \text{ N/mm}^2 \\ \gamma_f &= 1.2 & [-] \\ \theta &= 30^\circ \end{aligned} \quad (E.93)$$

The fibres give a contribution to the shear capacity of  $V_{Rdf} = 16295 \text{ kN}$ .

The influence of the prestressing force on the shear force is:

$$V_{pd} = -\frac{1}{2} \cdot q_{p,d} \cdot L \quad (E.94)$$

$$V_{pd} = -\frac{1}{2} \cdot 217 \cdot 40 = -4340 \text{ kN} \quad (E.95)$$

The maximum shear force occurs due to load model SW2. The corresponding load combination in the ULS gives a shear force of  $V_{Ed} = 10658 \text{ kN}$ . The shear resistance is dependent on whether the cross section is cracked or uncracked. The positive cracking moment is  $M_{cr} = W_{bot} \cdot (f_{ctd} + \frac{P_{m\infty}}{A_c}) = 62370 \text{ kNm}$ . This is less than the ultimate occurring bending moment. Therefore the shear capacity is calculated for a cracked cross section. There will probably be a larger capacity at the position of the ultimate shear force since the maximum shear force is located near the support and the maximum moment in the midspan.

$$u.c. = \frac{V_{Ed}}{V_{Rd}} = \frac{\frac{1}{2} \cdot (10658 - 4340)}{16295 + 7282} = 0.13 < 1.0 \quad (E.96)$$

Due to the slender webs of the trough bridge the capacity of the shear compressive strut should be verified. The resistance is calculated by:

$$V_{Rd,max} = \left( 1.14 \cdot \frac{0.85}{\gamma_E \gamma_c} f_{ck}^{\frac{2}{3}} \sin(2\theta) \right) \cdot b_w \cdot d \quad (\text{E.97})$$

Solving this equation gives that the shear compressive strut resistance is  $V_{Rd,max} = 29678 \text{ kN}$ .

$$u.c. = \frac{V_{Ed}}{V_{Rd,max}} = \frac{\frac{1}{2}(10658 - 4340)}{29678} = 0.11 < 1.0 \quad (\text{E.98})$$

### E.5.3 ULS - Lateral torsional buckling

The general verification for lateral torsional buckling is:

$$\frac{F_{Ed}}{F_{Rd}} + \frac{\bar{M}_{y,Ed}}{M_{y,Rd}} + \frac{\bar{M}_{z,Ed}}{M_{z,Rd}} \leq 1 \quad (\text{E.99})$$

The bending moment and bending moment resistance around the z-axis are calculated below.

$$M_{z,Rd} = \frac{I_{zz,wall}}{\frac{1}{2}b_w} \cdot f_{mu} = \frac{\frac{1}{12} \cdot 3080 \cdot 562^3}{\frac{1}{2} \cdot 562} \cdot 35 = 5675 \text{ kNm} \quad (\text{E.100})$$

$$M_{z,Ed} = \frac{F_E \cdot v_0}{k_1 n_z^* - 1} \quad (\text{E.101})$$

In this  $F_E$  is the euler buckling load,  $v_0$  is the initial horizontal excentricity and  $n_z^*$  is the second order factor.

$$F_E = \frac{\pi^2 \cdot EI_{zz,wall}}{l^2} = \frac{\pi^2 \cdot 55000 \cdot \frac{1}{12} \cdot 3080 \cdot 562^3}{40000^2} \cdot 10^{-3} = 15456 \text{ kN} \quad (\text{E.102})$$

$$v_0 = L/300 = 133 \text{ mm} \quad (\text{E.103})$$

The second order factor for a beam with a lateral support (in this case the trough floor) in the tension zone can be found with equation E.104.

$$\frac{1}{n_z^*} = \frac{k_1 M_{y1} + F_c \frac{h}{2}}{GI_t \frac{2}{h} + F_E \frac{h}{2}} \quad (\text{E.104})$$

$$G = \frac{E_{cm}}{2(1+\nu)} = 22917 \text{ N/mm}^2 \quad (\text{E.105})$$

$$I_t = \frac{1}{3} \cdot h \cdot b_w^3 = 1.82 \cdot 10^{11} \text{ mm}^4 \quad (\text{E.106})$$

$$k_1 = 0.80 \quad (\text{E.107})$$

With  $F_c = P_{m0}$  solving the second order factor gives  $n_z^* = 44$ .

$$M_{z,Ed} = \frac{15456 \cdot 10^3}{0.8} \cdot \frac{133}{44 - 1} = 60 \text{ kNm} \quad (\text{E.108})$$

$$u.c. = \frac{\frac{1}{2}P_{m0}}{f_{cd} \cdot b_w \cdot h} + \frac{\frac{1}{2}M_{y,Ed}}{M_{y,ud}} + \frac{M_{z,Ed}}{M_{z,Rd}} \quad (\text{E.109})$$

$$u.c. = \frac{\frac{1}{2} \cdot 49429}{276953} + \frac{34873}{71135} + \frac{60}{5675} = 0.59 < 1.0 \quad (\text{E.110})$$

### E.5.4 ULS - Fatigue

The ultimate bending moment for fatigue loading is:

$$M_{fat,max,d} = 1.0 \cdot (27028 + 10200) + 1.0 \cdot 24960 - 1.0 \cdot 34881 = 27307 \text{ kNm} \quad (\text{E.111})$$

The minimum bending moment for fatigue loading is:

$$M_{fat,min,d} = 1.0 \cdot (27028 + 10200) - 1.0 \cdot 34881 = -2347 \text{ kNm} \quad (\text{E.112})$$

The maximum and minimum occurring stresses in the top and bottom fiber are calculated with equations E.113 and E.114.

$$\sigma_{top} = -\frac{P_{m,inf}}{A_c} - \frac{M_{fat}}{W_{top}} \quad (\text{E.113})$$

$$\sigma_{bottom} = -\frac{P_{m,inf}}{A_c} + \frac{M_{fat}}{W_{bottom}} \quad (\text{E.114})$$

This results in the following maximum and minimum stresses.

$$\begin{aligned} \sigma_{t,max} &= -20 \text{ N/mm}^2 \\ \sigma_{t,min} &= -8 \text{ N/mm}^2 \\ \sigma_{b,max} &= -9 \text{ N/mm}^2 \\ \sigma_{b,min} &= -1 \text{ N/mm}^2 \end{aligned} \quad (\text{E.115})$$

The material properties for fatigue behavior are as follows.

$$f_{ctd,fat} = \frac{f_{ctk,0.05}}{\gamma_{c,fat}} = \frac{10}{1.5} = 6.7 \text{ N/mm}^2 \quad (\text{E.116})$$

$$f_{cd,fat} = \frac{f_{ck}}{\gamma_{c,fat}} \cdot \left(1 - \frac{f_{ck}}{400}\right) = \frac{180}{1.5} \cdot \left(1 - \frac{180}{400}\right) = 66 \text{ N/mm}^2 \quad (\text{E.117})$$

The top side of the structure is always in compression. The verification for compressive fatigue is done according to equation E.118.

$$\gamma_{sd} \cdot \sigma_{c,max} \cdot \eta_c \leq 0.45 \cdot f_{cd,fat} \quad (\text{E.118})$$

$$\eta_c = \frac{1}{1.5 - 0.5 \frac{|\sigma_1|}{|\sigma_{c,max}|}} \quad (\text{E.119})$$

$$\sigma_1 = -\frac{P_{m,inf}}{A_c} - \frac{M_{fat,max} \cdot (y_t - 300)}{I_{yy}} \quad (\text{E.120})$$

$$\sigma_1 = -\frac{39638 \cdot 10^3}{4661920} - \frac{27307 \cdot 10^6 \cdot (1898 - 300)}{4.47 \cdot 10^{12}} = -18 \text{ N/mm}^2 \quad (\text{E.121})$$

$$u.c. = \frac{1.0 \cdot 20 \cdot 0.96}{0.45 \cdot 66} = \frac{19}{29} = 0.66 \quad (\text{E.122})$$

The maximum compressive stress in the bottom of the structure is  $\sigma_b = -9 \text{ N/mm}^2$ .

$$\sigma_1 = -\frac{P_{m,inf}}{A_c} + \frac{M_{fat,min} \cdot (y_t - 300)}{I_{yy}} \quad (\text{E.123})$$

$$\sigma_1 = -\frac{39638 \cdot 10^3}{4661920} + \frac{-2347 \cdot 10^6 \cdot (1182 - 300)}{4.47 \cdot 10^{12}} = -9 \text{ N/mm}^2 \quad (\text{E.124})$$

$$u.c. = \frac{1.0 \cdot 9 \cdot 1.00}{0.45 \cdot 66} = \frac{9}{29} = 0.31 \quad (\text{E.125})$$

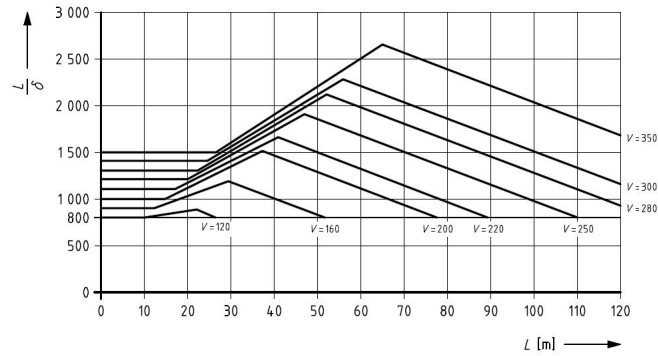


Figure E.3: Maximum allowable deflection

### E.5.5 SLS - Deflection

The load combination causing the largest deformation is the characteristic combination. Superposition is applied to find the resulting deflections of this combination. For the calculation of the bending stiffness  $EI$  the young's modulus at the time  $t = \infty$  has to be applied.

$$E_{cm,eff} = \frac{E_{cm}}{1 + \phi_{creep}} = 3.66 \cdot 10^4 \text{ N/mm}^2 \quad (\text{E.126})$$

$$w_{g,d} = \frac{5}{384} \cdot \frac{q_{g,d} \cdot l^4}{EI} = 27.5 \text{ mm} \quad (\text{E.127})$$

$$w_{track,d} = \frac{5}{384} \cdot \frac{q_{track,d} \cdot l^4}{EI} = 10.4 \text{ mm} \quad (\text{E.128})$$

$$w_{pq,d} = -\frac{5}{384} \cdot \frac{q_{p,d} \cdot l^4}{EI} = -44.2 \text{ mm} \quad (\text{E.129})$$

$$w_{pm,d} = -2 \cdot \frac{P_{m\infty ep}}{6 \cdot EI} \cdot \left( \frac{3}{4}l^2 - \frac{1}{8}l^2 - l^2 \right) = 10.6 \text{ mm} \quad (\text{E.130})$$

The deflection line due to SW2 can be found by making use of the displacement method. The load model divides the beam in three intervals. By applying the corresponding boundary conditions the equations for the deflection on each interval can be found. The resultant deflection at midspan was on this way found to be  $w_{SW2,d} = 31.5 \text{ mm}$ . The total deflection is  $w_d = 35.8 \text{ mm}$ .

The maximum allowable deflection is derived from figure E.3. For structures of one span the factor  $L/\delta$  may be reduced with a factor 0.7.

$$\frac{L}{\delta} = 1450 \quad (\text{E.131})$$

$$\delta = \frac{40000}{0.7 \cdot 1450} = 39.4 \text{ mm} \quad (\text{E.132})$$

The unity check for deflection become:

$$u.c. = \frac{35.8}{39.4} = 0.91 \quad (\text{E.133})$$

### E.5.6 SLS - Stresses

The OVS sets strict limits to the allowable tensile stresses in the concrete. These limits were used to define the prestressing boundary conditions. The actual occurring stresses are verified here. The maximum tensile stresses will occur at the top of the cross section at midspan during construction and at the bottom of the cross section at midspan at  $t = \infty$ ,  $t = 0$

$$\sigma_{top} = -\frac{P_0}{A_c} + \frac{M_p}{W_t} - \frac{M(G)}{W_t} \quad (\text{E.134})$$

$t = \infty$

$$\sigma_{bottom} = -\frac{P_\infty}{A_c} - \frac{M_p}{W_b} + \frac{M(G+Q)}{W_b} \quad (\text{E.135})$$

Load combination	Location	Effective stress	Allowable stress
Construction	top	-4.40 N/mm <sup>2</sup>	3.0 N/mm <sup>2</sup>
Construction	bottom	-12.92 N/mm <sup>2</sup>	3.0 N/mm <sup>2</sup>
Frequent	top	-21.11 N/mm <sup>2</sup>	1.5 N/mm <sup>2</sup>
Frequent	bottom	-0.63 N/mm <sup>2</sup>	0.0 N/mm <sup>2</sup>
Characteristic	top	-24.00 N/mm <sup>2</sup>	2.25 N/mm <sup>2</sup>
Characteristic	bottom	1.18 N/mm <sup>2</sup>	1.5 N/mm <sup>2</sup>
Quasi-permanent	top	-9.56 N/mm <sup>2</sup>	0 N/mm <sup>2</sup>
Quasi-permanent	bottom	-7.84 N/mm <sup>2</sup>	0 N/mm <sup>2</sup>

## E.6 Verifications - floor

The verifications for the floor have been performed on a strip of one meter wide. A conservative approach was used with fixed supports ( $r = 1.0$ ) and rotational spring supports with  $r = 0.5$ .

### E.6.1 Loads

For the manual calculation the trough floor has been modeled as a beam in two rotational springs on both sides. The spring stiffness is taken as  $r = 1.0$  for the maximum support moment and as  $r = 0.5$  for the maximum field moment.

The self weight of the structure is:

$$q_{g,k} = t_b \cdot \gamma_c = 0.30 \cdot 29 = 9 \text{ kN/m} \quad (\text{E.136})$$

The self weight of the track is:

$$q_{tr,k} = t_{track} \cdot \gamma_t = 0.58 \cdot 22 = 13 \text{ kN/m} \quad (\text{E.137})$$

The train axle loads have a magnitude of  $Q_k = 250 \text{ kN}$ , but they may be spread over three sleepers according to figure E.4. The concentrated load is spread by the sleeper with a length of 2520 mm. The load is spread to the neutral line of the floor with a ratio of 4:1 trough the ballast layer and 1:1 trough the concrete. The total area over which the concentrated loads are spread is:

$$b_Q = l_{sleeper} + \frac{2}{4} \cdot (t_{ballast} - h_{sleeper}) + 2 \cdot \frac{t_b}{2} = 2995 \text{ mm} \quad (\text{E.138})$$

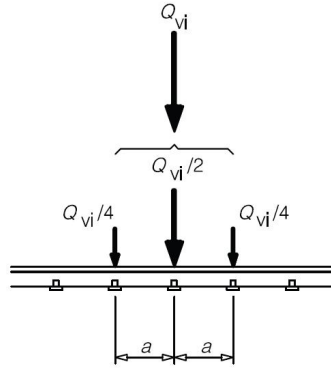


Figure E.4: Distribution in longitudinal direction of concentrated train loads.

$$l_Q = 2 \cdot a + \frac{2}{4} \cdot (t_{ballast} - h_{sleeper}) + t_b = 1675 \text{ mm} \quad (\text{E.139})$$

This makes the spread load due to the concentrated loads:

$$q_{Q,k} = \frac{Q_k}{l_Q \cdot b_Q} = 50 \text{ kN/m}^2 \quad (\text{E.140})$$

As the areas over which the load is spread overlap each other this spread load is doubled.

$$q_{Q,k} = 2 \cdot 50 = 100 \text{ kN/m}^2 \quad (\text{E.141})$$

For the fixed support the load effects are calculated with:

$$\begin{aligned} M_{s,k} &= -\frac{1}{12} \cdot q_k \cdot b_i^2 \\ V_{s,k} &= \frac{1}{2} \cdot q_k \cdot b_i \end{aligned} \quad (\text{E.142})$$

$$\begin{aligned} M_{s,g,k} &= -12 \text{ kNm} \\ M_{s,tr,k} &= -17 \text{ kNm} \\ M_{s,Q,k} &= -133 \text{ kNm} \end{aligned} \quad (\text{E.143})$$

$$\begin{aligned} V_{s,g,k} &= 18 \text{ kNm} \\ V_{s,tr,k} &= 26 \text{ kNm} \\ V_{s,Q,k} &= 200 \text{ kNm} \end{aligned} \quad (\text{E.144})$$

For the spring supported structure the load effects are calculated with:

$$M_{f,k} = \left(-\frac{1}{2} \cdot \frac{1}{12} + \frac{1}{8}\right) \cdot q_k \cdot (b_i + b_w)^2 \quad (\text{E.145})$$

$$\begin{aligned} M_{f,g,k} &= 12 \text{ kNm} \\ M_{f,tr,k} &= 17 \text{ kNm} \\ M_{f,Q,k} &= 133 \text{ kNm} \end{aligned} \quad (\text{E.146})$$

The load combinations in the ultimate limit state are:  
equation 6.10a

$$M_{s,d} = 1.5 \cdot (-12 - 17) + 1.35 \cdot -133 = -223 \text{ kNm} \quad (\text{E.147})$$

$$M_{f,d} = 1.5 \cdot (12 + 17) + 1.35 \cdot 133 = 223 \text{ kNm} \quad (\text{E.148})$$

$$V_{s,d} = 1.5 \cdot (18 + 26) + 1.35 \cdot 200 = 336 \text{ kN} \quad (\text{E.149})$$

equation 6.10b

$$M_{s,d} = 1.3 \cdot (-12 - 17) + 1.65 \cdot -133 = -257 \text{ kNm} \quad (\text{E.150})$$

$$M_{f,d} = 1.3 \cdot (12 + 17) + 1.65 \cdot 133 = 257 \text{ kNm} \quad (\text{E.151})$$

$$V_{s,d} = 1.3 \cdot (18 + 26) + 1.65 \cdot 200 = 387 \text{ kN} \quad (\text{E.152})$$

This gives that  $M_{s,d} = -336 \text{ kNm}$ ,  $M_{f,d} = 257 \text{ kNm}$  and  $V_{s,d} = 387 \text{ kN}$ .

The fatigue loads are:

Support

$$M_{s,fat,max} = M_{s,g,k} + M_{s,tr,k} + M_{s,Q,k} = -162 \text{ kNm} \quad (\text{E.153})$$

$$M_{s,fat,min} = M_{s,g,k} + M_{s,tr,k} = -29 \text{ kNm} \quad (\text{E.154})$$

Field

$$M_{f,fat,max} = M_{f,s,g,k} + M_{f,tr,k} + M_{f,Q,k} = 162 \text{ kNm} \quad (\text{E.155})$$

$$M_{f,fat,min} = M_{f,g,k} + M_{f,tr,k} = 29 \text{ kNm} \quad (\text{E.156})$$

## E.6.2 ULS - Bending moment capacity

The applied reinforcement in the floor in the cross direction is  $\varnothing 25 - 125$  at both the top and the bottom. This gives per side of the floor a reinforcement area of  $A_s = 3927 \text{ mm}^2$  per meter. Horizontal equilibrium is given by:

$$N_c = N_s + N_t \quad (\text{E.157})$$

Fully written this is:

$$\alpha \cdot f_{cd} \cdot 1000 \cdot x = f_{ctd} \cdot 1000 \cdot \left(\frac{1}{2}x_1 + x_2 + \frac{1}{2}x_3\right) + A_s \cdot f_{yd} \quad (\text{E.158})$$

The applied yield stress is  $300 \text{ N/mm}^2$ .

Solving this equation gives for the height of the compression zone  $x = 19 \text{ mm}$ . The concrete tension zone has a length of  $x_T = 80 \text{ mm}$ .

Horizontal equilibrium consists of the components:

$$\begin{aligned} N_c &= 1562 \text{ N/mm}^2 \\ T_1 &= 3 \text{ N/mm}^2 \\ T_2 &= 63 \text{ N/mm}^2 \\ T_3 &= 318 \text{ N/mm}^2 \\ N_s &= 1178 \text{ N/mm}^2 \end{aligned} \quad (\text{E.159})$$

As control the strain in the steel is calculated. Due to the high compressive strength it might occur that only a small compressive height is required for horizontal equilibrium. This can lead to a large curvature which may cause the steel to break.

$$\kappa_x = \frac{\epsilon_{cu3}}{x} = \frac{2.6 \cdot 10^{-3}}{19} = 1.37 \cdot 10^{-4} \quad (\text{E.160})$$

$$\epsilon_s = \kappa_x \cdot (d - x) = 1.53 \cdot 10^{-4} \cdot (267.5 - 18.8) \cdot 10^3 = 31.8^\circ/\infty \quad (\text{E.161})$$

The steel strain is greater than the yield strain  $\epsilon_{sy} = 2.2^\circ/\infty$  and smaller than the ultimate strain  $\epsilon_{su} = 32.5^\circ/\infty$ .

The ultimate compression zone height is given by:

$$f = \frac{(f_{pd} - \sigma_{p\infty})A_p^* + f_{yd}A_s}{A_p^* + A_s} = 300 \text{ N/mm}^2 \quad (\text{E.162})$$

$$k_3 = \frac{7 \cdot f}{\epsilon_{cu3} \cdot 10^6 + 7 \cdot f} = 0.45 \quad (\text{E.163})$$

$$x_u = (1 - k_3) \cdot d = 138 \text{ mm} \quad (\text{E.164})$$

This makes that the compression zone  $x$  is smaller than the ultimate compression zone  $x_u$ .

The bending moment capacity is  $M_{u,d, \text{floor}} = 308 \text{ kNm}$  for both the supports and the field cross section.

The unity checks as verification for the bending moment capacity now become:

$$\begin{aligned} \text{support} \quad u.c. &= \frac{-257}{-308} = 0.83 \\ \text{field} \quad u.c. &= \frac{257}{308} = 0.83 \end{aligned} \quad (\text{E.165})$$

### E.6.3 ULS - Shear capacity

The cracking moment of the floor is:

$$M_{cr} = f_{ctd} \cdot W_{fl} = 120 \text{ kNm} \quad (\text{E.166})$$

The floor is cracked, the shear resistance therefore exists of only the fibre part.

Fibres

$$V_{Rd,f} = \frac{S \cdot \sigma_p}{\gamma_f \cdot \tan \theta} \quad (\text{E.167})$$

In which:

$$\begin{aligned} S &= 0.9 \cdot 1000 \cdot t_b = 2.70 \cdot 10^5 \text{ mm}^2 \\ \sigma_p &= f_{ctd} = 8 \text{ N/mm}^2 \\ \gamma_f &= 1.2 \quad [-] \\ \theta &= 30^\circ \end{aligned} \quad (\text{E.168})$$

The fibres give a contribution to the shear capacity of  $V_{Rdf} = 3117 \text{ kN}$ . This is well above the occurring shear force. The verification now becomes:

$$u.c. = \frac{V_{s,d}}{V_{Rd}} = \frac{387}{3117} = 0.12 \quad (\text{E.169})$$

Verification of the compressive strut.

$$V_{Rd,max} = \left( 1.14 \cdot \frac{0.85}{\gamma_E \gamma_c} f_{ck}^{\frac{2}{3}} \sin(2\theta) \right) \cdot b \cdot d \quad (\text{E.170})$$

Solving this equation gives that the shear compressive strutt resistance is  $V_{Rd,max} = 4351 \text{ kN}$ .

$$u.c. = \frac{V_{Ed}}{V_{Rd,max}} = \frac{387}{4351} = 0.09 < 1.0 \quad (\text{E.171})$$

### E.6.4 ULS - Fatigue

At the support the stresses at the top and bottom of the cross section are:

$$\begin{aligned}
 \sigma_{s,t,max} &= \frac{M_{s,fat,max}}{W_{floor}} = 10.8 \text{ N/mm}^2 \\
 \sigma_{s,t,min} &= \frac{M_{s,fat,min}}{W_{floor}} = 1.9 \text{ N/mm}^2 \\
 \sigma_{s,b,max} &= \frac{M_{s,fat,max}}{W_{floor}} = -10.8 \text{ N/mm}^2 \\
 \sigma_{s,b,min} &= \frac{M_{s,fat,min}}{W_{floor}} = -1.9 \text{ N/mm}^2
 \end{aligned} \tag{E.172}$$

In the field the stresses at the top and bottom of the cross section are:

$$\begin{aligned}
 \sigma_{f,t,max} &= \frac{M_{f,fat,max}}{W_{floor}} = -10.8 \text{ N/mm}^2 \\
 \sigma_{f,t,min} &= \frac{M_{f,fat,min}}{W_{floor}} = -1.9 \text{ N/mm}^2 \\
 \sigma_{f,b,max} &= \frac{M_{f,fat,max}}{W_{floor}} = 10.8 \text{ N/mm}^2 \\
 \sigma_{f,b,min} &= \frac{M_{f,fat,min}}{W_{floor}} = 1.9 \text{ N/mm}^2
 \end{aligned} \tag{E.173}$$

Since the stresses in the field and the support are the same but in opposite direction they will only be verified once.

Compression

$$\gamma_{Sd} \cdot \sigma_{c,max} \cdot \eta_c \leq 0.45 \cdot f_{cd,fat} \tag{E.174}$$

$$\eta_c = \frac{1}{1.5 - 0.5 \frac{|\sigma_1|}{|\sigma_{c,max}|}} \tag{E.175}$$

$$\sigma_1 = 0 \text{ N/mm}^2 \tag{E.176}$$

$$u.c. = \frac{1.0 \cdot 10.8 \cdot 0.67}{0.45 \cdot 66} = \frac{7.2}{29} = 0.25 \tag{E.177}$$

Tension

$$\sigma_{fat,max} = 10.8 \text{ N/mm}^2 > \sigma_{ctd,fat} = 6.7 \text{ N/mm}^2 \tag{E.178}$$

The tensile stress is larger than the concrete fatigue tensile strength. Therefore the fatigue stresses will in total have to be taken by the reinforcement steel.

$$\sigma_{s,max} = \frac{M_{fat,max} \cdot (\frac{1}{2}t_b - c_r - \varnothing_l - \frac{1}{2}\varnothing_s)}{I_{floor}} \tag{E.179}$$

$$\sigma_{s,max} = \frac{162 \cdot 10^6 \cdot (150 - 20 - 16 - 12.5)}{\frac{1}{12} \cdot 1000 \cdot 300^3} = 7.3 \text{ N/mm}^2 \tag{E.180}$$

$$\sigma_{s,min} = \frac{M_{fat,min} \cdot (\frac{1}{2}t_b - c_r - \frac{1}{2}\varnothing_s)}{I_{floor}} \tag{E.181}$$

$$\sigma_{s,min} = \frac{29 \cdot 10^6 \cdot (150 - 20 - 16 - 12.5)}{\frac{1}{12} \cdot 1000 \cdot 300^3} = 1.3 \text{ N/mm}^2 \tag{E.182}$$

The stress range due to fatigue loading is  $\Delta\sigma_s = 6.0 \text{ N/mm}^2$ .

The number of train passages per day by the traffic group of 'heavy traffic with axel loads of 25t' is 51. The design lifetime of the structure is 100 years. This gives  $n = 51 \cdot 365 \cdot 100$  load cycles and  $\log n = 6.3$ . From this the fatigue strength of the steel can be calculated.

$$\Delta\sigma_{Rsk} = 160 - 0.3 \cdot \frac{160 - 95}{2} = 150 \text{ N/mm}^2 \quad (\text{E.183})$$

The unity check for the fatigue resistance of the reinforcement steel is:

$$u.c. = \frac{\gamma_{sd} \cdot \Delta\sigma_s}{\frac{\Delta\sigma_{Rsk}}{\gamma_{s, fat}}} = \frac{1.15 \cdot 6}{\frac{150}{1.15}} = 0.05 \quad (\text{E.184})$$

## E.7 Verification

This manual calculation has been done to verify the results from the matlab model. Below, in table E.5 some key values of the design for both the manual calculation and the matlab model are presented. In this some deviations can be noted.

Two effects explain the deviation in the bending moment. First, the manual calculation takes into account a larger prestressing force and second, the multiple layer model introduces a deviation as a certain force deviation is introduced due to the numerical approach.

The unity check on fatigue at the bottom side shows a deviation of 16%. Here the manual calculation takes into account a compressive stress of  $9 \text{ N/mm}^2$  where the model calculates  $7.6 \text{ N/mm}^2$ . This difference of  $1.4 \text{ N/mm}^2$  may be accepted at this point of the manual calculation.

The verifications on the floor show some rather large deviations. Here it must be noted that in the manual calculation the floor has been differently modeled than in the Matlab model. Besides this, due to the small dimensions of the floor the round of errors cause a larger impact percent wise. Although the application of a simplified static model reduces the possibility of verifying the model, it does show the structural soundness of the trough floor with the reduced thickness.

With these remarks and based on this comparison the results of the Matlab model may be accepted as realistic results.

Aspect	Units	Manual	Matlab	Difference
$L$	$m$	40	40	0.00
$h$	$mm$	3080	3080	0.00
$b_w$	$mm$	562	562	0.00
$t_{floor}$	$mm$	300	300	0.00
$A_c$	$mm^2$	4661920	4661920	0.00%
$y_{top}$	$mm$	1898	1898	0.00%
$y_{bot}$	$mm$	1182	1182	0.00%
$I_{yy}$	$mm^4$	$4.47 \cdot 10^{12}$	$4.47 \cdot 10^{12}$	0.00%
$W_{top}$	$mm^3$	$2.36 \cdot 10^9$	$2.35 \cdot 10^9$	0.25%
$W_{bot}$	$mm^3$	$3.78 \cdot 10^9$	$3.78 \cdot 10^9$	0.03%
$M_{Ed}$	$kNm$	104628	10793	-0.63%
$V_{Ed}$	$kN$	10658	10793	-1.27 %
$M_{q-p,d}$	$kNm$	37228	37247	-0.05%
$M_{freq,d}$	$kNm$	64492	64286	0.32 %
$M_{char,d}$	$kNm$	71308	71709	-0.56 %
$P_0$	$kN$	49429	49305	0.25%
$A_p$	$mm^2$	42560	42560	0.00%
Cables		16	16	0.00%
Strands		19	19	0.00%
time dependent loss	%	11.9	12.4	-3.89 %
$P_{m\infty}$	$kN$	39638	39157	1.21 %
u.c. bending moment	-	0.49	0.55	-12.24 %
u.c. shear	-	0.13	0.26	-99.23 %
u.c. compressive strut	-	0.11	0.23	-113.91 %
u.c. lateral torsional buckling	-	0.59	0.65	-9.61 %
u.c. fatigue top	-	0.66	0.66	0.36 %
u.c. fatigue bottom	-	0.31	0.26	16.13 %
u.c. deflection	-	0.91	0.86	5.58 %

Table E.5: Design values for manual calculation and model results in longitudinal direction.

Aspect	Units	Manual	Matlab	Difference
$M_{support}$	$kNm$	-270	-288	6.18%
$M_{field}$	$kNm$	270	304	11.18 %
u.c. bending moment support	-	0.83	0.84	1.19 %
u.c. bending moment field	-	0.83	0.89	6.74 %
u.c. shear	-	0.12	0.11	-14.08 %
u.c. compressive strut	-	0.09	0.07	-37.83 %
u.c. fatigue top	-	0.05	0.04	-33.25%
u.c. fatigue support	-	0.25	0.25	1.30%

Table E.6: Design values for manual calculation and model results of the floor.



## Appendix F

# Manual Calculation - Two span

### F.1 Geometry

The manual calculation as a verification of the computer model has been performed for the statically undetermined structure with two spans of twenty meters. The geometry in this manual calculation is the result of the model. The cross-section has been defined with the dimensions described below and has a total concrete area of  $A_c = 3256360 \text{ mm}^2$ .

wall height	$h$	2020	mm
wall thickness	$b_w$	509	mm
floor thickness	$t_b$	300	mm
internal width	$b_i$	4000	mm
outer width	$b_d$	5018	mm

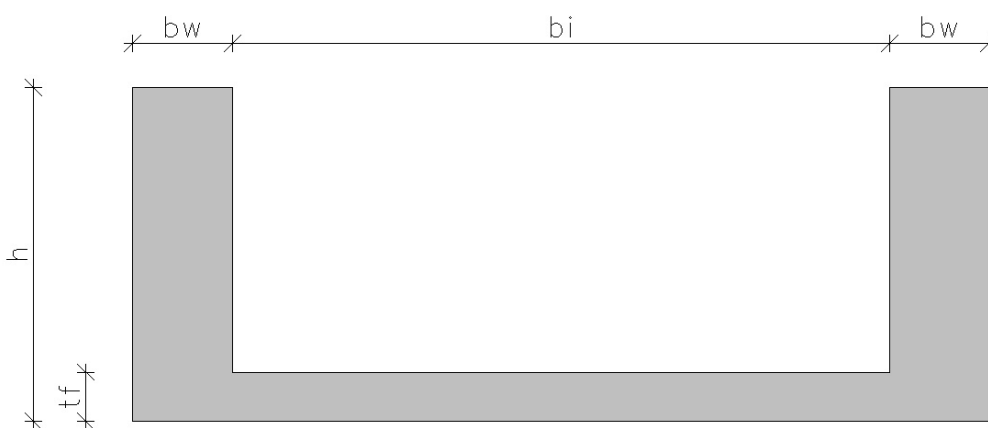


Figure F.1: Cross section

Further cross section properties:

Neutral line.

$$y_{bottom} = \frac{1}{A_c} \left( \frac{1}{2} \cdot b_i \cdot t_b^2 + 2 \cdot \frac{1}{2} b_w \cdot h^2 \right) \quad (\text{F.1})$$

$$y_{bottom} = \frac{1}{A_c} \left( \frac{1}{2} \cdot 4000 \cdot 300^2 + 2 \cdot \frac{1}{2} 300 \cdot 2020^2 \right) = 693 \text{ mm} \quad (\text{F.2})$$

$$y_{top} = h - y_{bottom} = 2020 - 693 = 1367 \text{ mm} \quad (\text{F.3})$$

Moment of inertia:

section	equation	value	unit
floor	$\frac{1}{12} \cdot b_d \cdot t_b^3 + b_d \cdot t_b \cdot (y_b - \frac{1}{2}t_b)^2$	$3.63 \cdot 10^{11}$	$mm^4$
walls	$\frac{2}{12} \cdot b_w \cdot h^3 + 2 \cdot b_w \cdot h \cdot (y_t - \frac{1}{2} \cdot h)^2$	$9.06 \cdot 10^{11}$	$mm^4$
total	$I_{yy} =$	$1.27 \cdot 10^{12}$	$mm^4$

Table F.1: Calculation of moment of inertia

This gives the following section moduli:

$$W_{bot} = \frac{I_{yy}}{y_{bottom}} = 1.83 \cdot 10^9 \text{ mm}^3 \quad (\text{F.4})$$

$$W_{top} = \frac{I_{yy}}{y_{top}} = 9.56 \cdot 10^8 \text{ mm}^3 \quad (\text{F.5})$$

## F.2 Loads - field

As the position of the maximum field bending moment changes in accordance with the load configuration, the maximum field moment has been calculated at the exact position if this was known. As for a single loaded span this position is at  $x = 0.44 \cdot L$  and for a continuous load over both spans this is at  $x = 0.38 \cdot L$ . For the sake of verifying the Matlab model the combination of the loads, or in case this exact position was unknown, the bending moment has been calculated at four tenth of the span ( $0.4 \cdot 20 = 8 \text{ m}$ ).

### F.2.1 Self weight

Self weight of the structure:

$$q_{g,k} = \gamma_c \cdot A_c = 29 \cdot 3.26 = 95 \text{ kN/m} \quad (\text{F.6})$$

The bending moment in the first span can be calculated by:

$$M_{f,g,k} = -\frac{1}{2} \cdot q_{g,k} \cdot x^2 + \frac{3}{8} \cdot q_{g,k} \cdot L \cdot x \quad (\text{F.7})$$

The maximum bending moment occurs at  $x = \frac{3}{8} \cdot L$  and is  $M_{f,g,k} = 2672 \text{ kNm}$ .

### F.2.2 Railtrack

Self weight of the railroad track:

$$q_{track,k} = \gamma_t \cdot t_{track} \cdot b_i = 22 \cdot 0.58 \cdot 4 = 51 \text{ kN/m} \quad (\text{F.8})$$

$$M_{f,track,k} = \frac{9}{128} \cdot q_{track,k} \cdot L^2 = \frac{9}{128} \cdot 51 \cdot 20^2 = 1434 \text{ kNm} \quad (\text{F.9})$$

### F.2.3 Load model 71

The load model consists of two infinite length block loads and four axle loads. For simplicity of the manual calculation the block loads have been combined to a continuous load and two axle loads have been combined to one point load. The maximum field moment is obtained when the second field is unloaded. The magnitude of the loads are calculated by multiplying the characteristic load with the factor  $\alpha = 1.21$  and the dynamic factor  $\Phi_3$ .

$$\Phi_3 = \frac{2.16}{\sqrt{L_\Phi - 0.2}} + 0.73 \quad (\text{F.10})$$

$$L_\Phi = 1.12 \cdot \frac{1}{2}(L1 + L2) = 1.12 \cdot \frac{1}{2}(20 + 20) = 24 \text{ m} \quad (\text{F.11})$$

$$\Phi_3 = \frac{2.16}{\sqrt{24 - 0.2}} + 0.73 = 1.19 \quad (\text{F.12})$$

$$q_{LM71,k} = 80 \cdot \alpha \cdot \Phi_3 = 80 \cdot 1.21 \cdot 1.19 = 115 \text{ kN/m} \quad (\text{F.13})$$

$$M_{f,q,k} = \frac{49}{512} \cdot q_{LM71,k} \cdot L^2 = 4402 \text{ kNm} \quad (\text{F.14})$$

$$Q_{v,k} = 250 \cdot \alpha \cdot \Phi_3 = 250 \cdot 1.21 \cdot 1.19 = 360 \text{ kN} \quad (\text{F.15})$$

$$M_{f,Q,k} = \frac{2 \cdot Q_{v,k} \cdot 0.4 \cdot 0.6 \cdot L^2}{4 \cdot L^3} (4 \cdot L^2 - 0.4 \cdot L(L + 0.4 \cdot L)) \quad (\text{F.16})$$

$$M_{f,Q,k} = \frac{2 \cdot 360 \cdot 0.4 \cdot 0.6 \cdot 20^2}{4 \cdot 20^3} (4 \cdot 20^2 - 0.4 \cdot 20(20 + 0.4 \cdot 20)) = 2972 \text{ kNm} \quad (\text{F.17})$$

Together the bending moment from load model 71 is:

$$M_{f,LM71,k} = 4402 + 2972 = 7374 \text{ kNm} \quad (\text{F.18})$$

### F.2.4 Load model SW/0

The load model SW/0 exists of two block loads of 15 meters long. The bending moment is calculated for one block load present on one span with its center situated at  $x = 0.4 \cdot L$ .

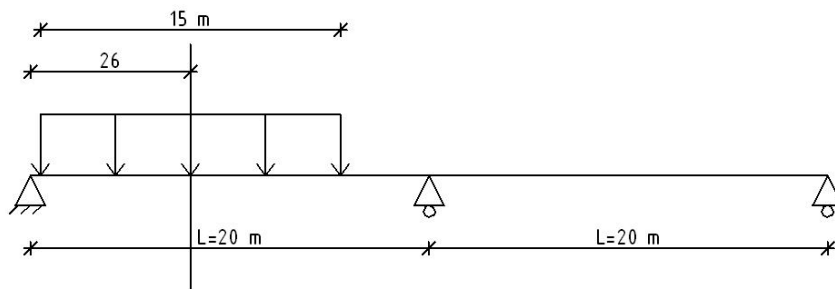


Figure F.2: Position of SW/0 block load for field moment.

$$q_{v,k} = 133 \cdot \alpha \cdot \Phi_3 = 133 \cdot 1.21 \cdot 1.19 = 192 \text{ kN/m} \quad (\text{F.19})$$

$$M_{f,SW0,k} = -\frac{1}{2}q_{v,k} \cdot x^2 + \frac{q(7 \cdot L^3 + 6 \cdot L \cdot a^2 - 4 \cdot a^3)x}{16 \cdot L^2} - \frac{1}{2}q_{v,k} \cdot a^2 \quad (\text{F.20})$$

For  $a = 2.5 \text{ m}$  and  $x = 8 \text{ m}$  this gives:

$$M_{f,SW0,k} = 6861 \text{ kNm} \quad (\text{F.21})$$

### F.2.5 Load model SW/2

The load model SW/2 exists of two block loads of 25 meters long. The maximum field moment occurs when one block completely covers one span, without being present on the second span.

$$q_{v,k} = 150 \cdot \alpha \cdot \Phi_3 = 150 \cdot 1.21 \cdot 1.19 = 216 \text{ kN/m} \quad (\text{F.22})$$

$$M_{f,SW2,k} = \frac{49}{512} \cdot q_{v,k} \cdot L^2 = 8269 \text{ kNm} \quad (\text{F.23})$$

### F.2.6 Fatigue loading

The four real train load models for fatigue have to be multiplied with the dynamic load factor for fatigue. This dynamic load factor  $\phi_{fat}$  is found to be:

$$K = \frac{v}{47.16L^{0.408}} = \frac{200}{47.16 \cdot 20^{0.408}} = 1.25 \quad (\text{F.24})$$

$$\phi' = \frac{K}{1 - K + K^4} = \frac{1.25}{1 - 1.25 + 1.25^4} = 0.57 \quad (\text{F.25})$$

$$\phi'' = 0.56 \cdot e^{-\frac{L_{\Phi}^2}{100}} = 0.56 \cdot e^{-\frac{24^2}{100}} = 0.0018 \quad (\text{F.26})$$

$$\phi_{fat} = 1 + \frac{1}{2}(\phi' + \frac{1}{2}\phi'') = 1.29 \quad (\text{F.27})$$

The equivalent spread load for the train models and the resulting maximum bending moment have been presented in table F.2.6. For the maximum field bending moment the continuous loading was put on one span. The bending moments have been calculated with equation F.28.

$$M_{f,fat,k} = \frac{49}{512} \cdot (q_{fat,k} \cdot \phi_{fat}) \cdot L^2 \quad (\text{F.28})$$

Load model	$q_k$ [kN/m]	$q_k \cdot \phi_{fat}$ [kN/m]	$M_{f,fat,k}$ [kNm]
5	80	103.2	3951
6	43	55.5	2125
11	57.2	73.8	2825
12	53.4	68.9	2638

Table F.2: fatigue loading

### F.2.7 Thermal loading - Heating

$$h_1 = 0.3 \cdot 2020 = 606 \text{ mm} > 150 \text{ mm} \rightarrow h_1 = 150 \text{ mm} \quad (\text{F.29})$$

$$h_2 = 0.3 \cdot 2020 = 606 \text{ mm} > 250 \text{ mm} \rightarrow h_2 = 250 \text{ mm} \quad (\text{F.30})$$

$$\Delta T_{b2} = -\frac{1}{2} \left[ -3 \cdot \frac{h_i}{h} + 2 \cdot \left( \frac{h_i}{h} \right)^2 \right] \cdot \frac{h_1 + h_2}{h_2} \cdot \Delta T_2 \quad (\text{F.31})$$

$$\Delta T_{b2} = -\frac{1}{2} \left[ -3 \cdot \frac{400}{2020} + 2 \cdot \left( \frac{400}{2020} \right)^2 \right] \cdot \frac{400}{250} \cdot 4.5 = 1.9^\circ \quad (\text{F.32})$$

$$\Delta T_1 = 10^\circ \text{C} - \frac{400}{250} \cdot 4.5^\circ \text{C} = 2.8^\circ \text{C} \quad (\text{F.33})$$

$$\Delta T_{b1} = -\frac{1}{2}[-3 \cdot \frac{h_i}{h} + 2 \cdot \left(\frac{h_i}{h}\right)^2] \cdot \Delta T_1 \quad (\text{F.34})$$

$$\Delta T_{b1} = -\frac{1}{2}[-3 \cdot \frac{150}{2020} + 2 \cdot \left(\frac{150}{2020}\right)^2] \cdot 2.8 = 0.3^\circ\text{C} \quad (\text{F.35})$$

$$\kappa = (\Delta T_{b1} + \Delta T_{b2}) \cdot \alpha_T \cdot \frac{1}{h/2} \quad (\text{F.36})$$

$$\kappa = (0.3 + 1.9) \cdot 15 \cdot 10^{-6} \cdot \frac{1}{2020/2} = 3.27 \cdot 10^{-8} \quad (\text{F.37})$$

The bending moment at  $x = 0.4 \cdot L$  is:

$$M_{f,T,h,k} = 0.4 \cdot \kappa \cdot \frac{3}{2} \cdot EI \quad (\text{F.38})$$

$$M_{f,T,h,k} = 0.4 \cdot 3420 = 1368 \text{ kNm} \quad (\text{F.39})$$

### F.2.8 Thermal loading - Cooling

$$h_1 = 0.2 \cdot 2020 = 404 \text{ mm} > 250 \text{ mm} \rightarrow h_1 = 250 \text{ mm} \quad (\text{F.40})$$

$$h_2 = 0.25 \cdot 2020 = 505 \text{ mm} > 200 \text{ mm} \rightarrow h_2 = 200 \text{ mm} \quad (\text{F.41})$$

$$\Delta T_{b2} = -\frac{1}{2}[-3 \cdot \frac{h_i}{h} + 2 \cdot \left(\frac{h_i}{h}\right)^2] \cdot \frac{h_1+h_2}{h_2} \cdot \Delta T_2 \quad (\text{F.42})$$

$$\Delta T_{b2} = -\frac{1}{2}[-3 \cdot \frac{450}{2020} + 2 \cdot \left(\frac{450}{2020}\right)^2] \cdot \frac{450}{200} \cdot -0.5 = -0.3^\circ\text{C} \quad (\text{F.43})$$

$$\Delta T_1 = -5^\circ\text{C} - \frac{450}{200} \cdot -0.5^\circ\text{C} = -3.9^\circ\text{C} \quad (\text{F.44})$$

$$\Delta T_{b1} = -\frac{1}{2}[-3 \cdot \frac{h_i}{h} + 2 \cdot \left(\frac{h_i}{h}\right)^2] \cdot \Delta T_1 \quad (\text{F.45})$$

$$\Delta T_{b1} = -\frac{1}{2}[-3 \cdot \frac{250}{2020} + 2 \cdot \left(\frac{250}{2020}\right)^2] \cdot -3.9 = -0.7^\circ\text{C} \quad (\text{F.46})$$

$$\kappa = (\Delta T_{b1} + \Delta T_{b2}) \cdot \alpha_T \cdot \frac{1}{h/2} \quad (\text{F.47})$$

$$\kappa = (-0.7 - 0.3) \cdot 15 \cdot 10^{-6} \cdot \frac{1}{2020/2} = -1.46 \cdot 10^{-8} \quad (\text{F.48})$$

The bending moment at  $x = 0.4 \cdot L$  is:

$$M_{f,T,c,k} = 0.4 \cdot \kappa \cdot \frac{3}{2} \cdot EI \quad (\text{F.49})$$

$$M_{f,T,c,k} = 0.4 \cdot -1530 = -612 \text{ kNm} \quad (\text{F.50})$$

### F.2.9 Uneven settlement

The largest bending moment due to uneven settlement will occur when the mid support will set (see derivation of uneven settlement loading in appendix B). The forced deformation of the mid support is  $\delta = 5 \text{ mm}$ . The effect of the bending moment in the field is taken at  $x = 0.4 \cdot L$ . As the moment distribution is linear the bending moment in the field is 0.4 times the bending moment at the support. Downward settlement:

$$M_{f,set,k} = 0.4 \cdot \frac{3 \cdot \delta \cdot E \cdot I_{yy}}{L^2} \cdot 10^{-6} = 0.4 \cdot 2617 = 1047 \text{ kNm} \quad (\text{F.51})$$

Upward settlement:

$$M_{f,set,k} = 0.4 \cdot -\frac{3 \cdot \delta \cdot E \cdot I_{yy}}{L^2} \cdot 10^{-6} = 0.4 \cdot -2617 = -1047 \text{ kNm} \quad (\text{F.52})$$

### F.3 Loads - support

#### F.3.1 self weight

The bending moment at the mids upport due to  $q_{g,k} = 95 \text{ kN/m}$  is:

$$M_{s,g,k} = -\frac{1}{8} \cdot q_{g,k} \cdot L^2 = -4750 \text{ kNm} \quad (\text{F.53})$$

The shear force at the support is:

$$V_{s,g,k} = -\frac{5}{8} \cdot q_{g,k} \cdot L = -1188 \text{ kN} \quad (\text{F.54})$$

#### F.3.2 Railtrack

The bending moment at the midsupport due to  $q_{track,k} = 51 \text{ kN/m}$  is:

$$M_{s,track,k} = -\frac{1}{8} \cdot q_{track,k} \cdot L^2 = -2550 \text{ kNm} \quad (\text{F.55})$$

The shear force at the support is:

$$V_{s,track,k} = -\frac{5}{8} \cdot q_{track,k} \cdot L = -638 \text{ kN} \quad (\text{F.56})$$

#### F.3.3 Load model 71

The position of the load is taken the same as for the field moment, but the spread load now continuous on the second field.

$$M_{s,q,k} = -\frac{1}{8} \cdot 115 \cdot 20^2 = -5750 \text{ kNm} \quad (\text{F.57})$$

$$M_{s,Q,k} = \frac{2 \cdot Q_{vk} \cdot a \cdot b \cdot L^2}{4 \cdot L^2} (L + 0.4 \cdot L) = -1210 \text{ kNm} \quad (\text{F.58})$$

$$M_{s,LM71,k} = -5750 - 1210 = -6960 \text{ kNm} \quad (\text{F.59})$$

The shear force at the support due to load model 71.

$$V_{s,q,k} = -\frac{5}{8} \cdot q_{v,k} \cdot L = -1438 \text{ kN} \quad (\text{F.60})$$

$$V_{s,Q,k} = -\frac{2 \cdot a \cdot F(5 \cdot L^2 - a^2)}{4 \cdot L^2} = -293 \text{ kN} \quad (\text{F.61})$$

$$V_{s,LM7,k} = -1438 - 293 = -1731 \text{ kN} \quad (\text{F.62})$$

#### F.3.4 Load model SW/0

The two block loads are each situated on one span symmetrically about the midsupport. This gives the following support moment.

$$M_{s,SW0,k} = \frac{q_{v,k}(3.34 \cdot 10^5 \cdot L - 1.66 \cdot 10^6 + 360 \cdot L^3 - 22854 \cdot L^2)}{16 \cdot L^2} + 147.75 \cdot q_{v,k} \quad (\text{F.63})$$

$$M_{s,SW0,k} = -8749 \text{ kNm} \quad (\text{F.64})$$

The shear force at the support is:

$$V_{s,SW0,k} = \frac{q_{v,k}(3.34 \cdot 10^5 \cdot L - 1.66 \cdot 10^6 + 360 \cdot L^3 - 22854 \cdot L^2)}{16 \cdot L^3} \quad (\text{F.65})$$

$$V_{s,SW0,k} = -1856 \text{ kNm} \quad (\text{F.66})$$

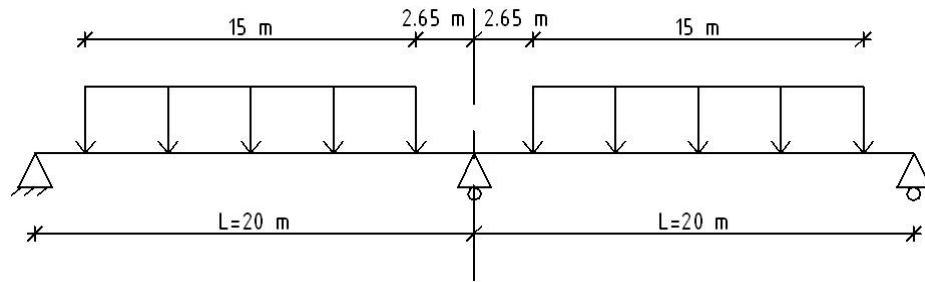


Figure F.3: Position of load model SW/0.

### F.3.5 Load model SW/2

The load model is placed with its outer edge on the outer support. The length of the block model is 25 m and will fill the first span and partly fill the second.

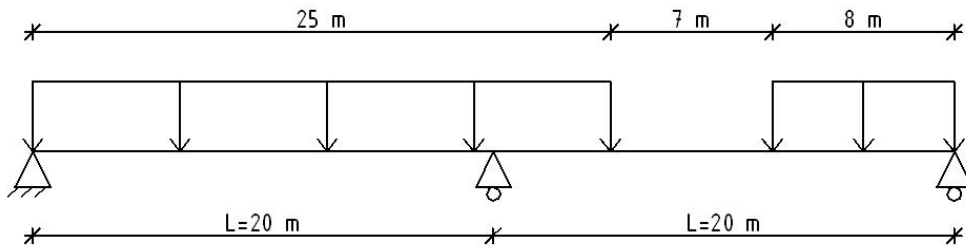


Figure F.4: Position of load model SW/2.

$$M_{s,w2,k} = -\frac{1}{2}q_{v,k} \cdot L^2 + \frac{q_{v,k}(32 \cdot L^3 + 1950 \cdot L^2 - 124800 \cdot L + 950625)}{8 \cdot (32 \cdot L - 1025)} \quad (\text{F.67})$$

$$M_{s,w2,k} = -7385 \text{ kNm} \quad (\text{F.68})$$

$$V_{s,w2,k} = -q_{v,k} \cdot L + \frac{q_{v,k}(32 \cdot L^3 + 1950 \cdot L^2 - 124800 \cdot L + 950625)}{8 \cdot (32 \cdot L - 1025)} \quad (\text{F.69})$$

$$V_{s,w2,k} = -2523 \text{ kN} \quad (\text{F.70})$$

### F.3.6 Fatigue loading

The fatigue load models result in the load effects table F.3.6.

### F.3.7 Thermal loading - Heating

The bending moment above the support has been calculated in section F.2.7.

$$M_{s,T,h,k} = 3420 \text{ kNm} \quad (\text{F.71})$$

The shear force at the support due to the thermal loading is:

$$V_{s,T,h,k} = \frac{3420}{20} = 171 \text{ kN} \quad (\text{F.72})$$

Load model	$q_k$ [kN/m]	$q_k \cdot \phi_{fat}$ [kN/m]	$M_{s,fat,k}$ [kNm]	$V_{s,fat,k}$ [kN]
5	80	103.2	-5160	-1290
6	43	55.5	-2775	-694
11	57.2	73.8	-3690	-923
12	53.4	68.9	-3445	-862

Table F.3: fatigue loading

### F.3.8 Thermal loading - Cooling

The bending moment above the support has been calculated in section F.2.8.

$$M_{s,T,c,k} = -1530 \text{ kNm} \quad (\text{F.73})$$

The shear force at the support due to the thermal loading is:

$$V_{s,T,c,k} = \frac{-1530}{20} = -77 \text{ kN} \quad (\text{F.74})$$

### F.3.9 Uneven settlement

The load effects at the mid support due to uneven settlement have been calculated.

Downward settlement:

$$M_{s,set,k} = \frac{3 \cdot \delta \cdot E \cdot I_{yy}}{L^2} \cdot 10^{-6} = 2617 \text{ kNm} \quad (\text{F.75})$$

$$V_{s,set,k} = \frac{2617}{20} = 131 \text{ kN} \quad (\text{F.76})$$

Upward settlement:

$$M_{s,set,k} = 0.4 \cdot -\frac{3 \cdot \delta \cdot E \cdot I_{yy}}{L^2} \cdot 10^{-6} = -1141 \text{ kNm} \quad (\text{F.77})$$

$$V_{s,set,k} = -\frac{2617}{20} = -131 \text{ kN} \quad (\text{F.78})$$

## F.4 Load Combinations - Field

The maximum bending moment in the field occurs under loading of SW/2

### F.4.1 Ultimate limit state

Equation 6.10a

$$M_{f,Ed} = \gamma_{G,j,sup} G_{k,j,sup} + \gamma_{Q,1} \Psi_{0,1} Q_{k,1} + \gamma_{Q,i} \Psi_{0,i} Q_{k,i} \quad (\text{F.79})$$

$$M_{f,Ed} = \gamma_{G,j,sup} \cdot (M_{f,g,k} + M_{f,track,k}) + \gamma_{Q,1} \Psi_{0,1} M_{f,SW2,k} \quad (\text{F.80})$$

$$M_{f,Ed} = 1.5 \cdot (2672 + 1434) + 1.35 \cdot 1.0 \cdot 8269 = 17322 \text{ kNm} \quad (\text{F.81})$$

Equation 6.10b

$$M_{f,Ed} = \gamma_{G,j,sup} G_{k,j,sup} + \gamma_{Q,1} Q_{k,1} + \gamma_{Q,i} \Psi_{0,i} Q_{k,i} \quad (\text{F.82})$$

$$M_{f,Ed} = \gamma_{G,j,sup} \cdot (M_{f,g,k} + M_{f,track,k}) + \gamma_{Q,1} M_{f,SW2,k} \quad (\text{F.83})$$

$$M_{f,Ed} = 1.3 \cdot (2672 + 1443) + 1.65 \cdot 1.0 \cdot 8269 = 18982 \text{ kNm} \quad (\text{F.84})$$

The largest resulting bending moment is governing.

$$M_{f,Ed} = 18982 \text{ kNm} \quad (\text{F.85})$$

## F.4.2 Serviceability limit state

Characteristic

$$M_{f,ch,d} = M_{f,g,k} + M_{f,track,k} + M_{f,SW2,k} + \Psi_0 \cdot M_{f,T,h,k} \quad (F.86)$$

$$M_{f,ch,d} = 2672 + 1434 + 8269 + 1.0 \cdot 1368 = 13743 \text{ kNm} \quad (F.87)$$

$$M_{f,ch,d} = 2672 + 1434 + 8269 + 1.0 \cdot -612 = 11763 \text{ kNm} \quad (F.88)$$

Frequent

$$M_{f,fr,d} = M_{f,g,k} + M_{f,track,k} + \Psi_1 \cdot M_{f,SW2,k} + \Psi_2 \cdot M_{f,T,h,k} \quad (F.89)$$

$$M_{f,fr,d} = 2672 + 1434 + 0.8 \cdot 8269 + 0.6 \cdot 1368 = 11542 \text{ kNm} \quad (F.90)$$

$$M_{f,fr,d} = 2672 + 1434 + 0.8 \cdot 8269 + 0.6 \cdot -612 = 10354 \text{ kNm} \quad (F.91)$$

Quasi-permanent

$$M_{f,qp,d} = M_{f,g,k} + M_{f,track,k} + \Psi_2 \cdot M_{f,SW2,k} + \Psi_2 \cdot M_{f,T,h,k} \quad (F.92)$$

$$M_{f,qp,d} = 2672 + 1434 + 0.0 \cdot 8269 + 0.5 \cdot 1368 = 4790 \text{ kNm} \quad (F.93)$$

$$M_{f,qp,d} = 2672 + 1434 + 0.0 \cdot 8269 + 0.5 \cdot -612 = 3800 \text{ kNm} \quad (F.94)$$

Construction

$$M_{f,constr,d} = 1.0 \cdot M_{f,g,k} = 2672 \text{ kNm} \quad (F.95)$$

## F.4.3 Fatigue loading

Minimum bending moment:

$$M_{f,fat,min,d} = M_{f,g,k} + M_{f,track,k} \quad (F.96)$$

$$M_{f,fat,min,d} = 2672 + 1434 = 4106 \text{ kNm} \quad (F.97)$$

Maximum bending moment:

$$M_{f,fat,max,d} = M_{f,g,k} + M_{f,track,k} + \gamma_{F,fat} M_{f,fat,k} \quad (F.98)$$

$$M_{f,fat,max,d} = 2672 + 1434 + 1.0 \cdot 3951 = 8057 \text{ kNm} \quad (F.99)$$

## F.5 Load Combinations - Support

### F.5.1 Ultimate limit state

Bending moment Equation 6.10a

$$M_{s,Ed} = \gamma_{G,j,sup} G_{k,j,sup} + \gamma_{Q,1} \Psi_{0,1} Q_{k,1} + \gamma_{Q,i} \Psi_{0,i} Q_{k,i} \quad (F.100)$$

$$M_{s,Ed} = \gamma_{G,j,sup} \cdot (M_{s,g,k} + M_{s,track,k}) + \gamma_{Q,1} \Psi_{0,1} M_{s,SW0,k} \quad (F.101)$$

$$M_{s,Ed} = 1.5 \cdot (-4750 - 2550) + 1.35 \cdot 1.0 \cdot -8749 = -22761 \text{ kNm} \quad (F.102)$$

Equation 6.10b

$$M_{s,Ed} = \gamma_{G,j,sup} G_{k,j,sup} + \gamma_{Q,1} Q_{k,1} + \gamma_{Q,i} \Psi_{0,i} Q_{k,i} \quad (F.103)$$

$$M_{s,Ed} = \gamma_{G,j,sup} \cdot (M_{s,g,k} + M_{s,track,k}) + \gamma_{Q,1} M_{s,SW0,k} \quad (F.104)$$

$$M_{s,Ed} = 1.3 \cdot (-4750 - 2550) + 1.65 \cdot 1.0 \cdot -8749 = -23926 \text{ kNm} \quad (F.105)$$

The largest resulting bending moment is governing.

$$M_{s,Ed} = -23926 \text{ kNm} \quad (\text{F.106})$$

Shear force Equation 6.10a

$$V_{s,Ed} = \gamma_{G,j,sup} \cdot (V_{s,g,k} + V_{s,track,k}) + \gamma_{Q,1} \Psi_{0,1} V_{s,SW2,k} \quad (\text{F.107})$$

$$V_{s,Ed} = 1.5 \cdot (-1188 - 638) + 1.35 \cdot 1.0 \cdot -2523 = -6145 \text{ kN} \quad (\text{F.108})$$

Equation 6.10b

$$V_{s,Ed} = \gamma_{G,j,sup} \cdot (V_{s,g,k} + V_{s,track,k}) + \gamma_{Q,1} V_{s,SW2,k} \quad (\text{F.109})$$

$$V_{s,Ed} = 1.3 \cdot (-1188 - 638) + 1.65 \cdot 1.0 \cdot -2523 = -6537 \text{ kN} \quad (\text{F.110})$$

The largest shear force is governing.

$$V_{s,Ed} = -6537 \text{ kN} \quad (\text{F.111})$$

### F.5.2 Serviceability limit state

Characteristic

$$M_{s,ch,d} = M_{s,g,k} + M_{s,track,k} + M_{s,SW0,k} + \Psi_0 \cdot M_{s,T,k} \quad (\text{F.112})$$

$$M_{s,ch,d} = -4750 - 2550 - 8749 - 1.0 \cdot 1530 = -17579 \text{ kNm} \quad (\text{F.113})$$

$$M_{s,ch,d} = -4750 - 2550 - 8749 + 1.0 \cdot 3420 = -12629 \text{ kNm} \quad (\text{F.114})$$

Frequent

$$F_{s,fr,d} = M_{s,g,k} + M_{s,track,k} + \Psi_1 \cdot M_{s,SW0,k} + \Psi_2 \cdot M_{s,T,k} \quad (\text{F.115})$$

$$M_{s,fr,d} = -4750 - 2550 + 0.8 \cdot -8749 + 0.6 \cdot -1530 = -15217 \text{ kNm} \quad (\text{F.116})$$

$$M_{s,fr,d} = -4750 - 2550 + 0.8 \cdot -8749 + 0.6 \cdot 3420 = -12247 \text{ kNm} \quad (\text{F.117})$$

Quasi-permanent

$$F_{s,qp,d} = M_{s,g,k} + M_{s,track,k} + \Psi_2 \cdot M_{s,SW0,k} + \Psi_2 \cdot M_{s,T,k} \quad (\text{F.118})$$

$$M_{s,qp,d} = -4750 - 2550 + 0.0 \cdot -8749 + 0.5 \cdot -1530 = -8065 \text{ kNm} \quad (\text{F.119})$$

$$M_{s,qp,d} = -4750 - 2550 + 0.0 \cdot -8749 + 0.5 \cdot 3420 = -5590 \text{ kNm} \quad (\text{F.120})$$

Construction

$$M_{s,constr,d} = 1.0 \cdot M_{s,g,k} = -4750 \text{ kNm} \quad (\text{F.121})$$

### F.5.3 Fatigue loading

Minimum bending moment:

$$M_{s,fat,min,d} = M_{s,g,k} + M_{s,track,k} \quad (\text{F.122})$$

$$M_{s,fat,min,d} = -4750 - 2550 = -7300 \text{ kNm} \quad (\text{F.123})$$

Maximum bending moment:

$$M_{s,fat,max,d} = M_{s,g,k} + M_{s,track,k} + \gamma_{F,fat} M_{s,fat,k} \quad (\text{F.124})$$

$$M_{s,fat,max,d} = -4750 - 2550 + 1.0 \cdot -5160 = -12460 \text{ kNm} \quad (\text{F.125})$$

## F.6 Prestressing

### F.6.1 Tendon profile

The tendon profile is symmetrical about the mid support. The tendon profile starts at the neutral line at the end of the structure. The eccentricity in the field is  $e_{pb} = 364 \text{ mm}$  and the eccentricity above the mid support is  $e_{ps} = 1104 \text{ mm}$ . The minimal radius of the tendon profile is  $R_{min} = 5 \text{ m}$ . The tendon profile can be described by two parabolic functions. The derivation of the functions can be found in appendix D. For the upward curvature:

$$g(x) = \frac{x^2}{2 \cdot R_{min} + \frac{x_2^2}{y_2}} \quad (\text{F.126})$$

For the downward curvature around the mid support:

$$h(x) = \frac{1}{2 \cdot R_{min}} \cdot (x - x_2)^2 + y_2 \quad (\text{F.127})$$

The key points of the tendon profile are:

$$x_2 = \frac{20 - \sqrt{\frac{0.364}{1.468} \cdot (20^2 - 2 \cdot -5 \cdot 0.364) + 2 \cdot -5 \cdot 0.364}}{1 - \frac{0.364}{1.468}} = 13.54 \text{ m} \quad (\text{F.128})$$

$$x_3 = 13.54 - 20 = -6.46 \text{ m} \quad (\text{F.129})$$

$$x_1 = 2 \cdot \frac{1.468}{13.54} \cdot -5 + 13.54 = 12.46 \text{ m} \quad (\text{F.130})$$

The radius of the tendon profile at the upward is defined as  $g''(x) = 1/R$ .

$$R = R_{min} + \frac{1}{2} \frac{x_2^2}{y_2} = 57 \text{ m} \quad (\text{F.131})$$

### F.6.2 Friction losses

The statically undetermined structure with two spans is supposed to be tensioned from two sides. This gives a symmetrical friction loss. The friction losses over one span have been calculated and presented in figure F.5.

The prestressing force after friction losses has been calculated according to:

$$P(x) = P_0 \cdot e^{-\mu(\Delta\theta + k \cdot x)} \quad (\text{F.132})$$

in which

$$\begin{array}{ll} \mu = 0.17 & [-] \quad \text{friction coefficient} \\ k = 0.008 & [rad/m] \quad \text{wobble effect} \end{array}$$

The absolute angular rotation can be calculated with the derivative of the tendon profile to  $x$ .

$$g'(x) = \frac{2 \cdot x}{2 \cdot R_{min} + \frac{x_2^2}{y_2}} \quad (\text{F.133})$$

Table F.6.2 shows the angular rotations and the corresponding frictions losses at the key points. The structure is supposed to be tensioned from both sides. Due to resulting symmetry only one span has to be evaluated.

$x - global [m]$	$x - local [m]$	$\theta [-]$	$\Delta\theta [rad]$	$P(x)/P_0 [-]$
0	-6.46	-0.112	0	1.00
6.46	0	0	0.112	0.97
18.92	12.46	0.221	0.333	0.92
20	13.54	0	0.494	0.89

Table F.4: Friction losses

The assumed wedge settlement is  $w_{set} = 10 \text{ mm}$ . The influence length of the wedge settlement is:

$$l_{set} = \left( \frac{w_{set} \cdot E_p}{\frac{\Delta\sigma_p}{\Delta x}} \right)^{0.5} = \left( \frac{10 \cdot 1.95 \cdot 10^5}{\frac{0.08}{18.92}} \right)^{0.5} \cdot 10^{-3} = 21.5 \text{ m} \quad (F.134)$$

$$P(21.5)/P_0 = 1 - \frac{0.08}{18.92} \cdot 21.5 = 0.91 \quad (F.135)$$

$$P(0) = 1 - 2 \cdot (1 - 0.91) = 0.82 \quad (F.136)$$

$$P_{mean} = \frac{\frac{1}{2}(0.80 + 0.92) \cdot 18.92 + \frac{1}{2} \cdot (0.90 + 0.91) \cdot (0.48) + \frac{1}{2}(0.91 + 0.89) \cdot 0.6}{20} \cdot P_0 = 0.86 \cdot P_0 \quad (F.137)$$

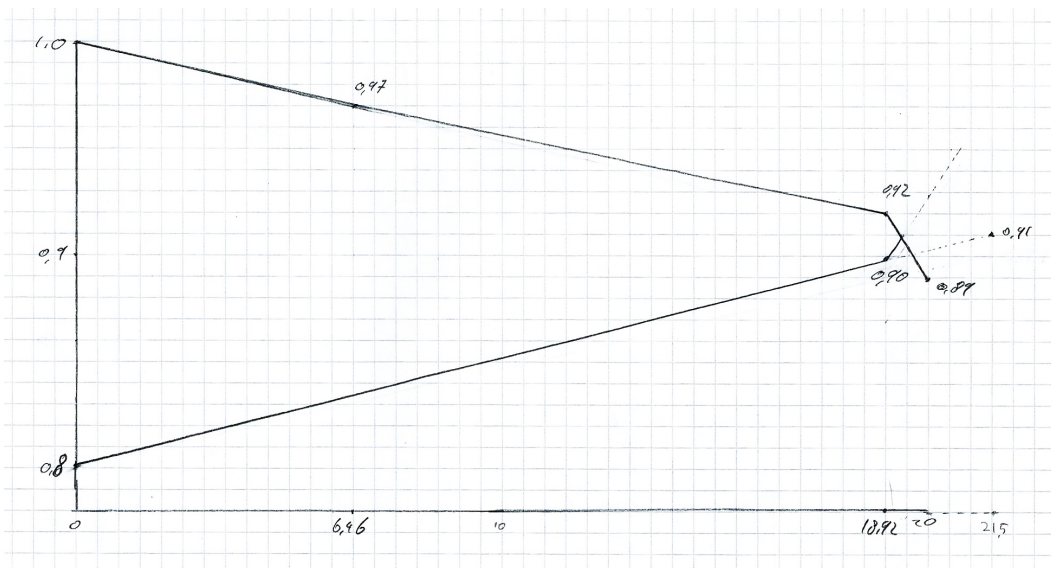


Figure F.5: Friction loss over one span.

### F.6.3 Initial prestressing force

The boundary conditions for the prestressing force with regard to the OVS-stress criteria can be found by a cross-section analysis. Two cross sections have been evaluated for this; in the field at  $x = 0.4 \cdot L = 8 \text{ m}$  and above the mid support. For solving the boundary conditions the bending

moment due to the prestressing force has to be known. This was calculated with the displacement method over four intervals with two upward and two downward continuous loads and a bending moment applied at the head of the structure (0 kNm due to  $e_p = 0$ ). The mean prestressing force over the upward directed curvature load is:

$$P_{m,up} = \frac{1}{2} \cdot (0.80 + 0.90) \cdot P = 0.85 \cdot P \quad (\text{F.138})$$

The mean prestressing over the downward directed curvature load is:

$$P_{m,down} = \frac{\frac{1}{2}(0.90 + 0.91) \cdot 0.48 + \frac{1}{2}(0.91 + 0.89) \cdot 0.6}{1.08} \cdot P = 0.90 \cdot P \quad (\text{F.139})$$

This gives that the absolute bending moment due to prestressing at  $x = 0.4 \cdot L = 8 \text{ m}$  is  $M_{f,p} = 0.38 \cdot P$ . The absolute prestressing bending moment above the support is  $M_{s,p} = 0.58 \cdot P$ .

Solving the boundary equations for the prestressing force, under the assumption of 15% time dependent losses, gives results shown in table F.6.3 and F.6.3.

Load combination	Location	$\sigma_{max}$ [ $N/mm^2$ ]	$M_d$ [ $kNm$ ]	$P_{m\infty}$ [ $kN$ ]	$P_{m0}$ [ $kN$ ]
construction	top	3	2672	--	< 63351
construction	bottom	3	2672	--	> 0
frequent	top	1.5	11542	< 148383	< 174568
frequent	bottom	0	10345	> 10980	> 12918
characteristic	top	2.25	11763	< 159110	< 187188
characteristic	bottom	1.5	13743	> 11663	> 13721
quasi-permanent	top	0	3800	< 43453	< 51121
quasi-permanent	bottom	0	4790	> 5080	> 5976

Table F.5: Boundary conditions to prestressing force in the field.

Load combination	Location	$\sigma_{max}$ [ $N/mm^2$ ]	$M_d$ [ $kNm$ ]	$P_{m\infty}$ [ $kN$ ]	$P_{m0}$ [ $kN$ ]
construction	top	3	4750	--	> 2162
construction	bottom	3	4750	--	< 684493
frequent	top	0	15217	> 17481	> 20566
frequent	bottom	1.5	12247	< 1002141	< 1178989
characteristic	top	1.5	17579	> 18546	> 21819
characteristic	bottom	2.25	12629	< 1119421	< 1316965
quasi-permanent	top	0	8065	> 9265	> 10900
quasi-permanent	bottom	0	5590	< 37366	< 43960

Table F.6: Boundary conditions to prestressing force above the support.

The results give that the minimum required prestressing force is  $P_{m0,min} = 21819 \text{ kN}$  and the maximum allowed prestressing force is  $P_{m0,max} = 43960 \text{ kN}$ . The applied prestressing force is  $P_{m0} = 21819 \text{ kN}$ .

### F.6.4 Applied prestressing

The required prestressing area is:

$$A_p = \frac{P_0}{\sigma_{pi}} = \frac{P_0}{0.8 \cdot f_{pu}} = \frac{23758 \cdot 10^3}{0.8 \cdot 1690} = 17572 \text{ mm}^2 \quad (\text{F.140})$$

The cables are applied in four parallel groups of equal number of cables. Applying twelve cables with 12 strands of 140 mm<sup>2</sup> each gives a prestressing area of:

$$A_p = 12 \cdot 12 \cdot 140 = 20160 \text{ mm}^2 \quad (\text{F.141})$$

The size of the required anchor plates is 200 mm wide by 240 mm high. With three cables situated above each other this means a wall height of  $3 \cdot (240 + 50) + 50 = 920 \text{ mm}$  is required. The height of the trough wall is 2020 mm. The required width is  $(2 \cdot (200 + 50) + 50 = 550 \text{ mm})$ . This is wider than the applied wall width of  $b_w = 509 \text{ mm}$ , therefore a local thickening of the wall is applied to provide enough space for the anchor heads.

### F.6.5 Time dependent losses

Creep

The stress at the location of the prestressing cable is calculated in the field and above the support due to the quasi permanent loading.

$$\begin{aligned} \text{Field : } \quad \sigma_{f,c} &= -\frac{P_{m0}}{A_c} - \frac{M_{f,p} \cdot e_{pb}}{I_{yy}} + \frac{M_{f,qp,d} \cdot e_{pb}}{I_{yy}} = -8 \text{ N/mm}^2 \\ \text{Support : } \quad \sigma_{s,c} &= -\frac{P_{m0}}{A_c} - \frac{M_{s,p} \cdot e_{ps}}{I_{yy}} + \frac{M_{s,qp,d} \cdot e_{ps}}{I_{yy}} = -11 \text{ N/mm}^2 \end{aligned} \quad (\text{F.142})$$

The largest compressive stress is used in the calculation of the creep loss. The used material properties are  $E_c = 1.05 \cdot E_{cm} = 57750 \text{ N/mm}^2$  and  $\phi(\infty, t_0) = 0.5$ .

$$\varepsilon_{cc}(\infty, t_0) = 0.5 \cdot \frac{-11}{57750} = -0.092 \text{ ‰} \quad (\text{F.143})$$

Shrinkage

Autogeneous shrinkage:

$$\varepsilon_{ca} = 2.5 \cdot (f_{ck} - 10) \cdot 10^{-6} = 2.5(172 - 10) \cdot 10^{-6} = 4.05 \cdot 10^{-4} \quad (\text{F.144})$$

Drying shrinkage is given to be less than or equal to  $\varepsilon_{cd} = 10^{-5}$ . Total shrinkage is:

$$\varepsilon_{cs} = 10^{-5} + 4.05 \cdot 10^{-4} = 0.415 \text{ ‰} \quad (\text{F.145})$$

Relaxation

$$\frac{\Delta \sigma_{pr}}{\sigma_{pi}} = 0.66 \cdot \rho_{1000} \cdot e^{9.1\mu} \left( \frac{t}{1000} \right)^{0.75(1-\mu)} \cdot 10^{-5} \quad (\text{F.146})$$

In which  $\rho_{1000} = 2.5\%$  and  $t = 876000$  hours and:

$$\sigma_{pi} = \frac{P_0}{A_p} = \frac{25371 \cdot 10^3}{20160} = 1258 \text{ N/mm}^2 \quad (\text{F.147})$$

$$\mu = \frac{\sigma_{pi}}{f_{pk}} = \frac{1258}{1860} = 0.68 \quad (\text{F.148})$$

$$\Delta\sigma_{pr} = 1258 \cdot 0.68 \cdot 2.5 \cdot e^{9.1 \cdot 0.68} \left( \frac{876000}{1000} \right)^{0.75(1-0.68)} \cdot 10^{-5} = 53 \text{ N/mm}^2 \quad (\text{F.149})$$

The total time dependent losses are:

$$\Delta\sigma_p = (\epsilon_{cc} + \epsilon_{cs}) \cdot E_p + \Delta\sigma_{pr} \quad (\text{F.150})$$

$$\Delta\sigma_p = (0.092 + 0.415) \cdot 10^{-3} \cdot 1.95 \cdot 10^5 + 53 = 152 \text{ N/mm}^2 \quad (\text{F.151})$$

$$\sigma_{pm0} = \frac{P_{m0}}{A_p} = \frac{21819 \cdot 10^3}{20160} = 1082 \text{ N/mm}^2 \quad (\text{F.152})$$

$$t_{dl} = \frac{\Delta\sigma_p}{\sigma_{pm0}} = \frac{152}{1082} \cdot 100\% = 14 \% \quad (\text{F.153})$$

The prestressing force at  $t = \infty$  is  $P_{m\infty} = 18764 \text{ kN}$ .

### F.6.6 Prestressing load effects

With  $P_{m\infty} = 18764 \text{ kN}$  the bending moments are:

$$M_{f,p} = -7149 \text{ kNm} \quad (\text{F.154})$$

$$M_{s,p} = 10883 \text{ kNm} \quad (\text{F.155})$$

The shear force at the support due to the prestressing force is:

$$V_{s,p} = -724 \text{ kN} \quad (\text{F.156})$$

## F.7 Verifications

### F.7.1 ULS - Bending moment capacity - Field

The effective width of the floor has been calculated as:

$$b_{eff,1} = 0.2 \cdot b_i + 0.1 \cdot l_0 \leq 0.5 \cdot b_i \leq 0.2 \cdot l_0 \quad (\text{F.157})$$

$$b_{eff,1} = 0.2 \cdot 4000 + 0.1 \cdot 20000 \leq 0.5 \cdot 4000 \leq 0.2 \cdot 20000 \quad (\text{F.158})$$

$$b_{eff,1} = 2800 \leq 2000 \leq 4000 \quad (\text{F.159})$$

The effective width of the floor is half of the width:  $b_{eff} = 2000 + 509 = 2509 \text{ mm}$ .

The applied reinforcement is practical reinforcement of  $\varnothing 16 - 150\text{mm}$  in one layer at the bottom of the floor. The reinforcement area in the effective width is:

$$A_s = \frac{b_{eff}}{s} \cdot \frac{1}{4} \cdot \pi \cdot d_r^2 = \frac{2509}{150} \cdot \frac{1}{4} \cdot \pi \cdot 16^2 = 3363 \text{ mm}^2 \quad (\text{F.160})$$

In order to find the height of the compression zone  $x$  the horizontal equilibrium is evaluated.

$$N_c = N_s + N_t + \Delta P + P_{m\infty} \quad (\text{F.161})$$

in which  $N_t$  is the tensile force in the concrete. This  $N_t$  is the sum of three different parts in the stress diagram.

$$\begin{aligned} T_1 &= \frac{1}{2} f_{ctd} \cdot x_1 \cdot b_w \\ T_2 &= f_{ctd} \cdot x_2 \cdot b_w \\ T_3 &= \frac{1}{2} f_{ctd} \cdot x_3 \cdot b_w \end{aligned} \quad (\text{F.162})$$

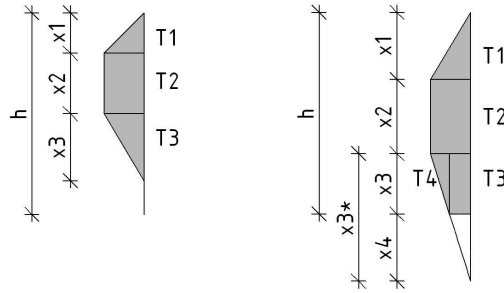


Figure F.6: Tension zone in the concrete. Left: cracked. Right: uncracked.

The distances  $x_1$ ,  $x_2$  and  $x_3$  can be calculated by:

$$\begin{aligned} \kappa_x &= \frac{\epsilon_{sy}}{z-x} \\ x_1 &= \frac{\epsilon_{ct}}{\kappa_x} = \frac{\epsilon_{ct}}{\epsilon_{sy}}(z-x) \\ x_2 &= \frac{\epsilon_{ctd} - \epsilon_{ct}}{\kappa_x} = \frac{\epsilon_{ctd} - \epsilon_{ct}}{\epsilon_{sy}}(z-x) \\ x_3 &= \frac{\epsilon_{ctu} - \epsilon_{ctd}}{\kappa_x} = \frac{\epsilon_{ctu} - \epsilon_{ctd}}{\epsilon_{sy}}(z-x) \end{aligned} \quad (\text{F.163})$$

The horizontal equilibrium can now be expressed in a function with only one unknown  $x$ .

$$N_c = N_s + N_t + \Delta P + P_{m\infty} \quad (\text{F.164})$$

$$\alpha \cdot f_{ct} \cdot b_w \cdot x = f_{ctd} \cdot b_w \cdot \left(\frac{1}{2}x_1 + x_2 + \frac{1}{2}x_3\right) + A_s \cdot f_{yd} + (f_{pd} - \sigma_{p\infty}) \cdot A_p + P_{m\infty} \quad (\text{F.165})$$

Solving this equation gives equilibrium for  $x = 580 \text{ mm}$ . The length of the concrete tension zone is calculated to be  $x_T = 2720 \text{ mm}$ .

This is larger than the cross section height. Therefore the cross section is reevaluated in a situation where  $x_3$  is limited by the height of the cross section.

A variable  $x_3^*$  is introduced. This is the length of  $x_3$  in case there would be no limit to it. The actual length of  $x_3$  equals  $x_3 = h - x - x_1 - x_2$ . The concrete tensile force is now calculated according to the second scheme in figure F.6. The equations from F.180 now become:

$$\begin{aligned} T_1 &= \frac{1}{2} f_{ctd} \cdot x_1 \cdot b_w \\ T_2 &= f_{ctd} \cdot x_2 \cdot b_w \\ T_3 &= (f_{ctd} - \theta_t \cdot x_3) \cdot x_3 \cdot b_w \\ T_4 &= \frac{1}{2} \cdot \theta_t \cdot x_3 \cdot b_w \end{aligned} \quad (\text{F.166})$$

In this  $\theta_t = \frac{f_{ctd}}{x_3^*}$ . Solving equation F.165 now gives  $x = 547 \text{ mm}$ . The calculated compressive and tension zone gives  $x + x_T = 547 + 1473 = 2020 \text{ mm}$ . The assumed stress distribution was right.

As control the strain in the steel is calculated. Due to the high compressive strength it might occur that only a small compressive height is required for horizontal equilibrium. This can lead to a large curvature which may cause the steel to break.

$$\kappa_x = \frac{\epsilon_{cu3}}{x} = \frac{2.6 \cdot 10^{-3}}{547} = 4.7 \cdot 10^{-6} \quad (\text{F.167})$$

$$\epsilon_s = \kappa_x \cdot (d - x) = 4.7 \cdot 10^{-6} \cdot (1992 - 264) \cdot 10^3 = 8.2^\circ / \infty \quad (\text{F.168})$$

The steel strain is greater than the steel yield strain  $\epsilon_{sy} = 2.2^\circ / \infty$  and less than the ultimate steel strain  $\epsilon_{su} = 32.5^\circ / \infty$ .

The maximum compressive height  $x_u$  is calculated and should be greater than  $x$  in order to prevent compressive failure.

$$f = \frac{(f_{pd} - \sigma_{p\infty})A_p + f_{yd}A_s}{A_p + A_s} \quad (\text{F.169})$$

$$f = \frac{(1690 - 930) \cdot 0.5 \cdot 20160 + 435 \cdot 3363}{0.5 \cdot 20160 + 3235} = 679 \quad (\text{F.170})$$

$$k_3 = \frac{7 \cdot f}{\epsilon_{cu3} \cdot 10^6 + 7 \cdot f} = 0.65 \quad (\text{F.171})$$

$$x_u = (1 - k_3) \cdot d = 705 \text{ mm} \quad (\text{F.172})$$

This makes that  $x < x_u$ .

As the requirements with regard to the maximum compressive height are satisfied the force equilibrium can be used to calculate the bending moment capacity of a single trough wall.

$$M_{f,ud} = N_c \cdot (1 - \beta) \cdot x + \frac{2}{3} \cdot x_1 \cdot T_1 + (x_1 + 0.5 \cdot x_2) \cdot T_2 + (x_1 + x_2 + \frac{1}{2} \cdot x_3) \cdot T_3 + (x_1 + x_2 + \frac{1}{3} \cdot x_3) \cdot T_4 + (z - x) \cdot N_s + \Delta P \cdot e_p \quad (\text{F.173})$$

$$\begin{aligned} x_1 &= 23 \text{ mm} \\ x_2 &= 230 \text{ mm} \\ x_3 &= 1221 \text{ mm} \end{aligned} \quad (\text{F.174})$$

$$\begin{aligned} N_c &= 23158 \text{ kN} \\ N_t &= 4642 \text{ kN} \\ N_s &= 1463 \text{ kN} \\ \Delta P &= 7671 \text{ kN} \end{aligned} \quad (\text{F.175})$$

$$M_{f,ud} = 22015 \text{ kNm} \quad (\text{F.176})$$

Performing a unity check for the bending moment capacity in the ultimate limit state gives:

$$u.c. = \frac{0.5 \cdot (M_{f,Ed} + M_{f,p})}{M_{f,ud}} = \frac{0.5 \cdot (18982 - 7149)}{22015} = 0.27 < 1.0 \quad (\text{F.177})$$

## F.7.2 ULS - Bending moment capacity - Support

The applied reinforcement at the top of the wall in longitudinal direction is of  $\varnothing 20 - 100\text{mm}$  in one layer. The reinforcement area is:

$$A_s = \frac{b_w - 2 \cdot c - 2 \cdot \varnothing_{stirrup}}{s} \cdot \frac{1}{4} \cdot \pi \cdot d_r^2 = \frac{509 - 2 \cdot 20 - 2 \cdot 16}{100} \cdot \frac{1}{4} \cdot \pi \cdot 20^2 = 1257 \text{ mm}^2 \quad (\text{F.178})$$

In order to find the height of the compression zone  $x$  the horizontal equilibrium is evaluated.

$$N_c = N_s + N_t + \Delta P + P_{m\infty} \quad (\text{F.179})$$

As the compressive zone is located at the floor the compressive force is calculated with the effective width. For sake of simplicity of the manual calculation the compressive zone has been calculated with the wall width.

$$\begin{aligned} T_1 &= \frac{1}{2} f_{ctd} \cdot x_1 \cdot b_w \\ T_2 &= f_{ctd} \cdot x_2 \cdot b_w \\ T_3 &= \frac{1}{2} f_{ctd} \cdot x_3 \cdot b_w \end{aligned} \quad (\text{F.180})$$

Solving horizontal equilibrium for the only unknown, the compressive zone height  $x$ . The resulting compressive zone height is  $x = 551 \text{ mm}$ . The tension zone length is  $x_T = 2585 \text{ mm}$  which is larger than the construction height.

The alternative calculation method from figure F.6 and equation F.166 is applied. This results in a concrete compressive zone height of  $x = 524 \text{ mm}$ . The resulting tensile zone length is  $x_T = 1496$

The maximum compressive zone height  $x_u$  should be larger than the occurring compressive zone.

$$f = \frac{(f_{pd} - \sigma_{p\infty})0.5 \cdot A_p + f_{yd}A_s}{0.5 \cdot A_p + A_s} \quad (\text{F.181})$$

$$f = \frac{(1690 - 930) \cdot 0.5 \cdot 20160 + 435 \cdot 1257}{0.5 \cdot 20160 + 1257} = 724 \text{ N/mm}^2 \quad (\text{F.182})$$

$$k_3 = \frac{7 \cdot f}{\epsilon_{cu3} \cdot 10^6 + 7 \cdot f} = 0.66 \quad (\text{F.183})$$

$$x_u = (1 - k_3) \cdot d = 675 \text{ mm} \quad (\text{F.184})$$

The maximum compressive zone is satisfied since  $x = 524 \text{ mm} < x_u = 675 \text{ mm}$ .

The bending moment capacity can be calculated with:

$$M_{s,ud} = (1 - \beta) \cdot x \cdot N_c + \frac{2}{3} \cdot x_1 \cdot T_1 + (x_1 + 0.5 \cdot x_2) \cdot T_2 + (x_1 + x_2 + \frac{1}{2} \cdot x_3) \cdot T_3 + (z - x) \cdot N_s + \Delta P \cdot e_p \quad (\text{F.185})$$

With:

$$\begin{aligned} x_1 &= 21 \text{ mm} \\ x_2 &= 221 \text{ mm} \\ x_3 &= 1254 \text{ mm} \end{aligned} \quad (\text{F.186})$$

$$\begin{aligned} N_c &= 22204 \text{ kN} \\ N_t &= 4604 \text{ kN} \\ N_s &= 547 \text{ kN} \\ \Delta P &= 7671 \text{ kN} \end{aligned} \quad (\text{F.187})$$

$$M_{s,ud} = 21015 \text{ kNm} \quad (\text{F.188})$$

The bending moment capacity of each trough wall is  $M_{s,ud} = 21015 \text{ kNm}$ .

Performing a unity check for the bending moment capacity in the ultimate limit state gives:

$$u.c. = \frac{0.5 \cdot (M_{s,Ed} + M_{sp})}{M_{f,ud}} = \frac{0.5 \cdot (23926 - 10883)}{21015} = 0.31 < 1.0 \quad (\text{F.189})$$

### F.7.3 ULS - Shear capacity

The shear force capacity of the individual components of the concrete, reinforcement and steel fibres have been calculated below. The evaluated cross section is located at the mid support.

Concrete.

$$V_{Rd,c} = \left( C_{Rdc} \cdot k \cdot (100 \cdot \rho_1 \cdot f_{ck})^{1/3} + k_1 \cdot \sigma_{cp} \right) \cdot b_w \cdot d \cdot 10^{-3} \quad (\text{F.190})$$

In which:

$$\begin{aligned} C_{Rdc} &= \frac{0.18}{\gamma_c} = 0.12 & [-] \\ k &= \sqrt{1 + \frac{200}{d}} \leq 2.0 = 1.05 & [-] \\ d &= h - c - 0.5 \cdot \varnothing_l = 1992 \text{ mm} \\ \rho_1 &= \frac{A_s}{b_w \cdot d} = 5.9 \cdot 10^{-4} & [-] \\ A_s &= \frac{b_w - 2 \cdot c_r - 2 \cdot \varnothing_{stirrup}}{s} \cdot \frac{1}{4} \pi \cdot \varnothing_l^2 = 603 \text{ mm}^2 \\ f_{ck} &= 172 & \text{N/mm}^2 \\ k_1 &= 0.15 & [-] \\ \sigma_{cp} &= \frac{P_{mso}}{A_c} \leq 0.2 \cdot f_{cd} = 5.8 & \text{N/mm}^2 \end{aligned} \quad (\text{F.191})$$

Evaluation equation F.190 with the values from F.191 gives  $V_{Rdc} = 1159 \text{ kN}$ .

Shear reinforcement.

$$V_{Rd,s} = 0.9 d \frac{A_{sw}}{s} f_{y;d} (\sin \alpha + \cos \alpha) \quad (\text{F.192})$$

In which:

$$\begin{aligned} A_{sw} &= 3 \cdot \frac{1}{4} \cdot \pi \cdot \varnothing_s^2 = 628 & \text{mm}^2 \\ \varnothing_s &= 20 & \text{mm} \\ s &= 100 & \text{mm} \\ \alpha &= 90^\circ \end{aligned} \quad (\text{F.193})$$

This gives a capacity of the shear reinforcement of  $V_{Rds} = 4898 \text{ kN}$ .

Fibres

$$V_{Rd,f} = \frac{S \cdot \sigma_p}{\gamma_f \cdot \tan \theta} \quad (\text{F.194})$$

In which:

$$\begin{aligned} S &= 0.9 \cdot b_w \cdot d = 9.13 \cdot 10^5 & \text{mm}^2 \\ \sigma_p &= 8 & \text{N/mm}^2 \\ \gamma_f &= 1.2 & [-] \\ \theta &= 30^\circ \end{aligned} \quad (\text{F.195})$$

The fibres give a contribution to the shear capacity of  $V_{Rdf} = 10537 \text{ kN}$ .

The maximum occurring shear force at the support is  $V_{s,Ed} + V_{s,p} = -6537 - 724 = -7261 \text{ kN}$ . The corresponding bending moment is  $M_{s,Ed} + M_{s,p} = -23926 + 10883 = -13043 \text{ kNm}$ . The resistance is dependent on whether or not the cross section is cracked. The cracking moment of the cross section is  $M_{s,cr} = W_{top} \cdot f_{ctd} = -7648 \text{ kNm}$ . The cross section is cracked.

The shear resistance is now:

$$V_{s,Rd} = V_{Rd,s} + V_{Rd,f} = 15435 \text{ kN} \quad (\text{F.196})$$

Performing the verification for the shear resistance gives:

$$u.c. = \frac{0.5 \cdot V_{s,Ed}}{V_{s,Rd}} = \frac{0.5 \cdot 7261}{15435} = 0.24 < 1.0 \quad (\text{F.197})$$

Due to the slender webs of the trough bridge the capacity of the shear compressive strut should be verified. The resistance is calculated by:

$$V_{Rd,max} = \left( 1.14 \cdot \frac{0.85}{\gamma_E \gamma_c} f_{ck}^{\frac{2}{3}} \sin(2\theta) \right) \cdot b_w \cdot d \quad (\text{F.198})$$

The maximum shear resistance is  $V_{Rd,max} = 17544 \text{ kN}$ .

$$u.c. = \frac{0.5 \cdot V_{s,Ed}}{V_{Rd,max}} = \frac{0.5 \cdot 7261}{17544} = 0.21 < 1.0 \quad (\text{F.199})$$

#### F.7.4 ULS - Lateral torsional buckling

The general verification for lateral torsional buckling is:

$$\frac{F_{Ed}}{F_{Rd}} + \frac{\bar{M}_{y,Ed}}{M_{y,Rd}} + \frac{\bar{M}_{z,Ed}}{M_{z,Rd}} \leq 1 \quad (\text{F.200})$$

The bending moment and bending moment resistance around the z-axis are calculated below.

$$M_{z,Rd} = \frac{I_{zz,wall}}{\frac{1}{2} b_w} \cdot f_{mu} = \frac{\frac{1}{12} \cdot 2020 \cdot 509^3}{253} \cdot 35 = 3053 \text{ kNm} \quad (\text{F.201})$$

$$M_{z,Ed} = \frac{F_E}{k_1} \frac{\bar{v}_0}{n_z^* - 1} \quad (\text{F.202})$$

In this  $F_E$  is the Euler buckling load for a beam with an infinity stiff mid support,  $v_0$  is the initial horizontal eccentricity and  $n_z^*$  is the second order factor.

$$F_E = \frac{4 \cdot \pi^2 \cdot EI_{zz}}{l^2} = \frac{4 \cdot \pi^2 \cdot 55000 \cdot \frac{1}{12} \cdot 2020 \cdot 509^3}{20000^2} \cdot 10^{-3} = 120500 \text{ kN} \quad (\text{F.203})$$

$$v_0 = L/300 = 67 \text{ mm} \quad (\text{F.204})$$

The second order factor for a beam with a lateral support (in this case the trough floor) in the tension zone can be found with equation F.205.

$$\frac{1}{n_z^*} = \frac{k_1 M_{y1} + F_c \frac{h}{2}}{GI_t \frac{2}{h} + F_E \frac{h}{2}} \quad (\text{F.205})$$

$$G = \frac{E_{cm}}{2(1+\nu)} = 22917 \text{ N/mm}^2 \quad (\text{F.206})$$

$$I_t = \frac{1}{3} \cdot h \cdot b_w^3 = 8.88 \cdot 10^{10} \text{ mm}^4 \quad (\text{F.207})$$

$$k_1 = 0.80 \quad (\text{F.208})$$

$$\frac{1}{n_z^*} = \frac{0.8 \cdot \frac{1}{2} \cdot 11833 \cdot 10^6 + \frac{1}{2} \cdot 21819 \cdot 10^3 \frac{2020}{2}}{22917 \cdot 8.8 \cdot 10^{10} \frac{2}{2020} + 120500 \cdot 10^3 \frac{2020}{2}} \quad (\text{F.209})$$

This gives that  $n_z^* = 134$ .

$$M_{z,Ed} = \frac{120500 \cdot 10^3}{0.8} \cdot \frac{67}{134 - 1} = 76 \text{ kNm} \quad (\text{F.210})$$

$$u.c. = \frac{\frac{1}{2} P_{m0}}{f_{cd} \cdot b_w \cdot h} + \frac{\frac{1}{2} M_{y,Ed}}{M_{y,Rd}} + \frac{M_{z,Ed}}{M_{z,Rd}} \quad (\text{F.211})$$

$$u.c. = \frac{\frac{1}{2} \cdot 21819 \cdot 10^3}{164509 \cdot 10^3} + \frac{\frac{1}{2} \cdot (18982 - 7149) \cdot 10^6}{22015 \cdot 10^6} + \frac{76 \cdot 10^6}{3053 \cdot 10^6} = 0.36 < 1.0 \quad (\text{F.212})$$

### F.7.5 ULS - Fatigue field

The maximum bending moment for fatigue is:

$$M_{f,fat,max} = 8057 - 7149 = 908 \text{ kNm} \quad (\text{F.213})$$

The minimum bending moment for fatigue is:

$$M_{f,fat,min} = 4106 - 7149 = -3043 \text{ kNm} \quad (\text{F.214})$$

The resulting stresses in the top and bottom fiber are:

$$\begin{aligned} \sigma_{t,max} &= -\frac{M_{f,fat,max}}{W_{top}} - \frac{P_{m,\infty}}{A_c} = -7 \text{ N/mm}^2 \\ \sigma_{t,min} &= -\frac{M_{f,fat,min}}{W_{top}} - \frac{P_{m,\infty}}{A_c} = -3 \text{ N/mm}^2 \\ \sigma_{b,max} &= \frac{M_{f,fat,max}}{W_{bot}} - \frac{P_{m,\infty}}{A_c} = -5 \text{ N/mm}^2 \\ \sigma_{b,min} &= \frac{M_{f,fat,min}}{W_{bot}} - \frac{P_{m,\infty}}{A_c} = -7 \text{ N/mm}^2 \end{aligned} \quad (\text{F.215})$$

As all stresses remain in compression only the largest compressive stress is verified on fatigue strength.

$$\gamma_{sd}\sigma_{t,max}\eta_c \leq 0.45 \cdot f_{cd,fat} \quad (\text{F.216})$$

$$\eta_c = \frac{1}{1.5 - 0.5 \cdot |\sigma_{c1}|/|\sigma_{c2}|} \quad (\text{F.217})$$

In which  $\gamma_{sd} = 1$  and  $\sigma_{c1}$  is the smallest compressive stress within 300 mm from the considered fibre. The stress in the considered fibre is  $\sigma_{c2}$ .

$$\sigma_{c1} = \frac{M_{f,fat,min} \cdot 10^6 \cdot (y_{bot} - 300)}{I_{yy}} - \frac{P_{m,\infty}}{A_c} = -7 \text{ N/mm}^2 \quad (\text{F.218})$$

$$\eta_c = \frac{1}{1.5 - 0.5 \cdot |7|/|7|} = 1.00 \quad (\text{F.219})$$

$$1.0 \cdot 7 \cdot 1.00 = 7 \text{ N/mm}^2 \leq 0.45 \cdot 65 = 29 \text{ N/mm}^2 \quad (\text{F.220})$$

In the field the requirements with regard to fatigue are met.

### F.7.6 ULS - Fatigue support

The maximum bending moment for fatigue is:

$$M_{s,fat,max} = -12460 + 10883 = -1577 \text{ kNm} \quad (\text{F.221})$$

The minimum bending moment for fatigue is:

$$M_{s,fat,min} = -7300 + 10883 = 3583 \text{ kNm} \quad (\text{F.222})$$

The resulting stresses in the top and bottom fiber are:

$$\begin{aligned} \sigma_{t,max} &= -\frac{M_{s,fat,max}}{W_{top}} - \frac{P_{m,\infty}}{A_c} = -4 \text{ N/mm}^2 \\ \sigma_{t,min} &= -\frac{M_{s,fat,min}}{W_{top}} - \frac{P_{m,\infty}}{A_c} = -10 \text{ N/mm}^2 \\ \sigma_{b,max} &= \frac{M_{s,fat,max}}{W_{bot}} - \frac{P_{m,\infty}}{A_c} = -7 \text{ N/mm}^2 \\ \sigma_{b,min} &= \frac{M_{s,fat,min}}{W_{bot}} - \frac{P_{m,\infty}}{A_c} = -4 \text{ N/mm}^2 \end{aligned} \quad (\text{F.223})$$

As all stresses remain in compression only the largest compressive stress is verified on fatigue strength.

$$\gamma_{Sd} \sigma_{t,max} \eta_c \leq 0.45 \cdot f_{cd,fat} \quad (F.224)$$

$$\eta_c = \frac{1}{1.5 - 0.5 \cdot |\sigma_{c1}| / |\sigma_{c2}|} \quad (F.225)$$

In which  $\gamma_{Sd} = 1$  and  $\sigma_{c1}$  is the smallest compressive stress within 300 mm from the considered fibre. The stress in the considered fibre is  $\sigma_{c2}$ .

$$\sigma_{c1} = -\frac{M_{s,fat,min} \cdot 10^6 \cdot (y_{top} - 300)}{I_{yy}} - \frac{P_{m,\infty}}{A_c} = -9 \text{ N/mm}^2 \quad (F.226)$$

$$\eta_c = \frac{1}{1.5 - 0.5 \cdot |9| / |10|} = 0.95 \quad (F.227)$$

$$1.0 \cdot 10 \cdot 0.95 = 9.5 \text{ N/mm}^2 \leq 0.45 \cdot 65 = 29 \text{ N/mm}^2 \quad (F.228)$$

At the support the requirements with regard to fatigue are met.

### F.7.7 SLS - Deflection

The load combination which causes the largest deformation is the characteristic combination for the field with cooling as thermal loading. The total deformation at  $x = 8 \text{ m}$  is determined by evaluating the separate load effects and use superposition for the total deformation. The individual load effects have been determined with the displacement method.

The bending stiffness  $EI$  for deformation is taken at  $t = \infty$  with  $E = E_{cm,eff}$ .

$$E_{cm,eff} = \frac{E_{cm}}{1 + \phi_{creep}} = 3.7 \cdot 10^4 \text{ N/mm}^2 \quad (F.229)$$

Self weight

$$w_{g,d} = \frac{27}{5} \frac{q_{g,d} \cdot L^4}{EI} \cdot 10^{-3} = 1.7 \text{ mm} \quad (F.230)$$

$$w_{track,d} = \frac{27}{5} \frac{q_{track,d} \cdot L^4}{EI} \cdot 10^{-3} = 0.9 \text{ mm} \quad (F.231)$$

$$w_{T,c,d} = \frac{3}{25} \kappa \cdot L^2 = 0.8 \text{ mm} \quad (F.232)$$

$$w_{p,d} = -\frac{1.17 \cdot 10^{10} \cdot P_{m,\infty}}{EI} = -4.7 \text{ mm} \quad (F.233)$$

For the verification of the deflection the factor  $\alpha$  for the weight of load model SW2 may be taken as  $\alpha = 1.0$ . This gives that the loading due to SW2 for deflection is:

$$q_{v,k} = 0.5 \cdot 150 \cdot \alpha \cdot \Phi_3 = 150 \cdot 1.00 \cdot 1.19 = 179 \text{ kN/m} \quad (F.234)$$

Evaluation using the displacement method gives  $w_{SW2} = 5.4 \text{ mm}$ .

The total deflection is  $w_{Ed} = 4.1 \text{ mm}$ .

The maximum allowable deflection is derived from figure F.7 and is:

$$\frac{L}{\delta} = 1100 \quad (F.235)$$

$$\delta = \frac{20000}{1100} = 18 \text{ mm} \quad (F.236)$$

The verification with regard to deflection is satisfied as  $w_d = 4.1 \text{ mm} < \delta = 18 \text{ mm}$ .

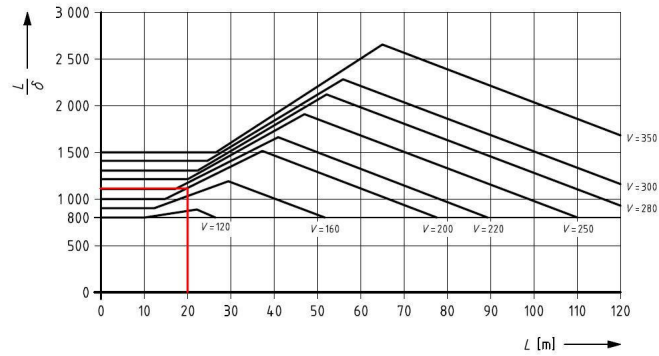


Figure F.7: Maximum allowable deflection

### F.7.8 SLS - Stresses

The OVS sets strict limits to the allowable tensile stresses in the concrete. These limits were used to define the prestressing boundary conditions. The actual occurring stresses are verified here. The maximum tensile stresses will occur at the top of the cross section at midspan during construction and the quasi-permanent load combination and at the bottom of the cross section at midspan at  $t = \infty$  for the frequent and characteristic loading.

Load combination	Effective stress	Allowable stress
Construction	$-9.5 \text{ N/mm}^2$	$3.0 \text{ N/mm}^2$
Quasi-permanent	$-7.1 \text{ N/mm}^2$	$0 \text{ N/mm}^2$
Frequent	$-3.4 \text{ N/mm}^2$	$0.0 \text{ N/mm}^2$
Characteristic	$-2.2 \text{ N/mm}^2$	$1.5 \text{ N/mm}^2$

Table F.7: Stress verification at the field.

Load combination	Effective stress	Allowable stress
Construction	$-1.7 \text{ N/mm}^2$	$3.0 \text{ N/mm}^2$
Quasi-permanent	$-8.7 \text{ N/mm}^2$	$0 \text{ N/mm}^2$
Frequent	$-1.2 \text{ N/mm}^2$	$0.0 \text{ N/mm}^2$
Characteristic	$1.2 \text{ N/mm}^2$	$1.5 \text{ N/mm}^2$

Table F.8: Stress verification at the support.

All effective stresses are smaller than the allowable stresses. Therefore the verification is satisfied.

## F.8 Floor

The dimensions of the floor are the same as for the single span trough bridge. For the manual calculation see appendix E.

## F.9 Verification

Below in table F.9 some key values of the design for both the manual calculation and the matlab model are presented. In this some deviations from the matlab results can be noted.

First the minimum required prestressing is almost 15 % higher than in the matlab results. Consequently this leads to the application of a higher prestressing force. The requirement for the minimum prestressing force is given in by the characteristic load combination a the support cross section. Here the deviation of the working bending moment is 3%. Acceptable, but it does lead to a higher prestressing requirement.

The difference in the applied prestressing force causes a deviation in the resulting time dependent losses.

The large difference in the unity check for the support bending moment can be explained as the manual calculation only calculates the bending moment capacity of the trough wall, while the matlab-model takes the effective width into account, providing a larger capacity.

The deviation in the shear force verification can be explained as the manual calculation only verifies the shear capacity in one cross section. The model evaluates the shear verification at all discretized cross section and takes the shear force and resistance at that point into account.

Based on this comparison the results of the matlab model may be accepted as realistic results.

Aspect	Units	Manual	Matlab	Difference
$L$	$m$	20	20	0.00%
$h$	$mm$	2020	2020	0.00%
$b_w$	$mm$	509	509	0.00%
$t_{floor}$	$mm$	300	300	0.00%
$A_c$	$mm^2$	3256360	3256360	0.00%
$y_t$	$mm$	1327	1327	0.00%
$y_b$	$mm$	693	693	0.00%
$I_{yy}$	$mm^4$	$1.27 \cdot 10^{12}$	$1.27 \cdot 10^{12}$	0.02%
$W_{bot}$	$mm^3$	$1.82 \cdot 10^9$	$1.83 \cdot 10^9$	-0.58%
$W_{top}$	$mm^3$	$9.56 \cdot 10^8$	$9.56 \cdot 10^8$	-0.01%
Field				
$M_{Ed}$	$kNm$	18982	119104	-0.64%
$M_{qp,d}$	$kNm$	4790	4743	0.99%
$M_{freq,d}$	$kNm$	11542	11337	1.78%
$M_{char,d}$	$kNm$	13743	13284	3.34%
Support				
$M_{Ed}$	$kNm$	-23926	-22941	-4.12%
$M_{qp,d}$	$kNm$	-8065	-8136	-0.87%
$M_{freq,d}$	$kNm$	-15217	-15104	0.74%
$M_{char,d}$	$kNm$	-17579	-17099	2.73%
Prestressing				
$P_{m,0}$	$kN$	23758	20252	14.76%
$A_p$	$mm^2$	20160	20160	0.00%
Cables		12	12	0.00%
Strands		12	12	0.00%
time dependent loss	%	14	16	-14.29%
Verifications				
u.c. bending moment field	-	0.27	0.26	-6.81%
u.c. bending moment support	-	0.31	0.16	48.39%
u.c. shear	-	0.24	0.21	12.50%
u.c. compressive strut	-	0.21	0.20	4.76%
u.c. lateral torsional buckling	-	0.36	0.34	5.56%
u.c. fatigue field	-	0.24	0.22	8.33%
u.c. fatigue support	-	0.32	0.29	9.38%
u.c. deflection	-	0.23	0.28	-21.74%

Table F.9: Design values for manual calculation and model results in longitudinal direction.



## Appendix G

### Verification non-linear beam model

For the verification of the non-linear beam model a test environment has been programmed. In this environment the bending moment, curvature, rotation and deflection for a statically undetermined beam with two spans of 5000 mm have been evaluated both analytically and numerically.

The analytical equation for the bending moment, curvature, rotation and deflection have been determined with the displacement method. The equations have been transposed to Matlab. This allows a comparison of both results later on.

The considered beam is a small concrete beam of 500 mm high and 400 mm wide. The applied reinforcement is  $5\varnothing 16 = 1005 \text{ mm}^2$ . The dimensions, reinforcement and its corresponding moment-curvature diagram have been taken from chapter 4 the book 'Ontwerpen in gewapend beton' (Sagel R., 2003). As the considered structure is statically undetermined negative bending moments and curvatures must be accommodated. For simplicity it was assumed that the same amount of reinforcement was present at the top side of the beam and the moment-curvature diagram could therefore also be applied in the opposite direction.

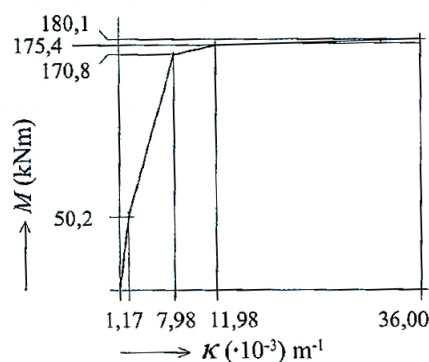


Figure G.1: Positive side of moment-curvature diagram (Sagel R., 2003).

The moment-curvature diagram shows that the linear elastic branch goes up to a bending moment of 50.2 kNm. This means that as long as the absolute maximum bending moment is below 50.2 kNm the analytical and numerical results should give the same result. The maximum continuous load in the linear elastic calculation is has been applied on one span.

$$q = \frac{M \cdot 8}{L^2} = \frac{50.2 \cdot 8}{5^2} = 16.0 \text{ kNm}. \quad (\text{G.1})$$

Figure G.2 to G.4 show the deviations in the results between the analytical and the numerical approach within the linear-elastic branch. The deviations in the curvature are of the order  $10^{-22}$  while the order for the actual curvature is  $10^{-6}$ . The deviations are therefore  $1 \cdot 10^{16}$  times as small. Due to the two times numerical integration the deviation in the deflection is only  $1/10^{-3}$  times as small. The deviation in the deflection is therefore in the order of thousandth of millimeters. This is excepted as deviation for the model.

Figure G.5 shows the iterations for the deflection under a constant load on both spans of 25 kN/m. The crossed line are the analytical results. The deflection at the support is initially too high. After redistribution of the bending moment and recalculation the deflection four times the deflection at the support is within the allowed limit.

After redistribution of the bending moment the total area of the moment distribution line ( $A_M$ ) should still be the same. The redistributed moment is determined by deducting the support moment with a certain step size  $M_{step}$ . This step size is then used to calculate by how much the bending moment at the other cross sections should be reduced. This is a linear function between zero and  $M_{step}$ . The value  $M_{step}$  is an integer, the values on the linear function are not all integers. The round of by Matlab causes a deviation from the actual value. Each iteration therefore increases the total area of the bending moment. With a step size of  $M_{step} = M_{support}/1000$  this deviation is 0.158% of the area  $A_M$  (in this specific test environment).

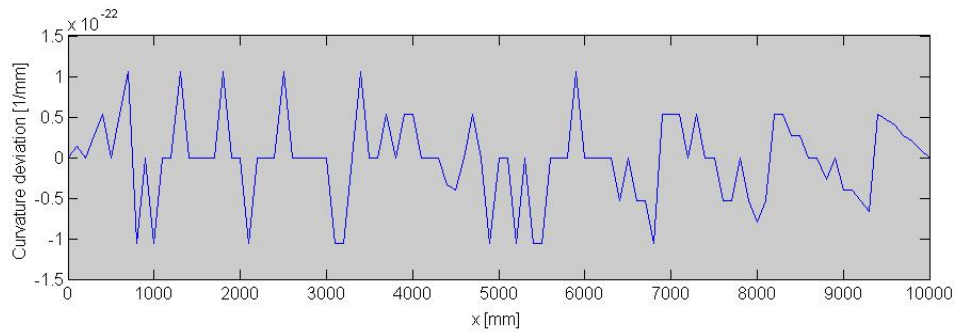


Figure G.2: Deviation in curvature between numerical and analytical results.

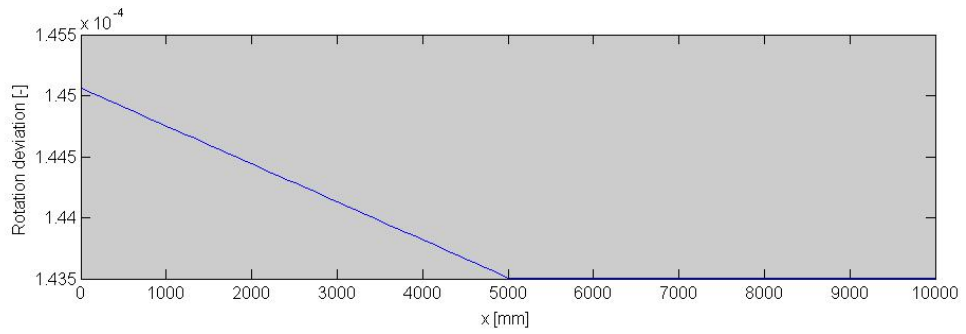


Figure G.3: Deviation in rotation between numerical and analytical results.

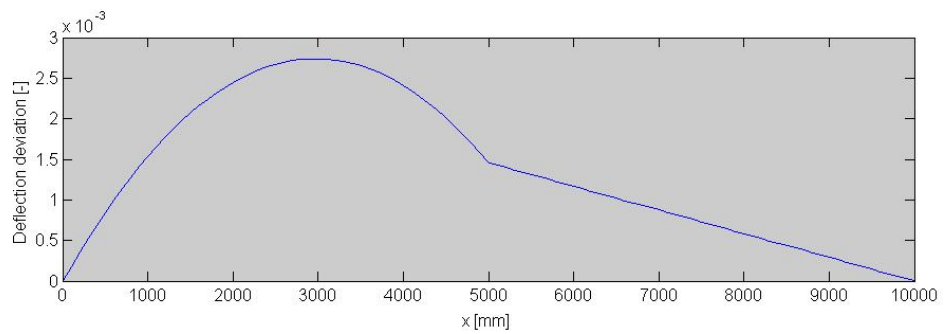


Figure G.4: Deviation in deflection between numerical and analytical results.

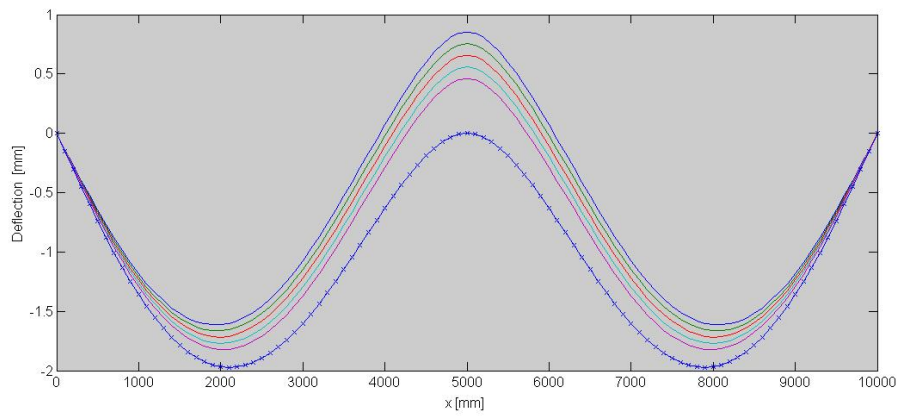


Figure G.5: Iterations of the deflection.